ABSTRACT

Title of dissertation: ANALYSIS AND IMPEDANCE-BASED DETECTION OF ELECTROMAGNETIC COIL INSULATION DEGRADATION

N. Jordan Jameson, 2019

Dissertation directed by: Professor Michael Pecht and Dr. Michael Azarian
Center for Advanced Life Cycle Engineering
Department of Mechanical Engineering

Electromagnetic induction coils are widely used in a variety of applications, such as motors, solenoid valves, and relays. Many of these applications are safety-critical. Failure of the insulation that protects the windings in electromagnetic coils is a significant cause of coil failure and can have severe implications for system reliability. An effective insulation health monitoring program can reduce maintenance and replacement costs, predict the useful lifetime of the coil, and improve the operational availability of the system in which the coil is used. Impedance monitoring of coils has emerged as a promising approach for non-invasive, in-situ insulation health assessments of electromagnetic coils. Yet, little was understood about the relationship between coil impedance and traditional insulation health metrics, such as insulation capacitance and insulation resistance. Furthermore, relating the impedance measurements to chemical and mechanical characteristics of the insulation material is important to understanding the relationship between impedance measurements and the state of the insulation at failure. This study describes the development an

improved method of electromagnetic coil insulation health monitoring and shows the uncovered relationships between coil impedance and the insulation electrical, chemical, and mechanical properties.

ANALYSIS AND IMPEDANCE-BASED DETECTION OF ELECTROMAGNETIC COIL INSULATION DEGRADATION

by

N. Jordan Jameson

Dissertation submitted to the Faculty of the Graduate School of the
University of Maryland, College Park in partial fulfillment
of the requirements for the degree of
Doctor of Philosophy
2019

Advisory Committee:
Prof. Michael Pecht, Chair/Advisor
Dr. Michael Azarian, Co-Chair/Co-Advisor
Prof. Thomas Antonsen, Dean's Representative
Prof. Abijit Dasgupta
Prof. Bongtae Han
Prof. Peter Sandborn

Dedication

To my wife, Kylie. Words cannot express my gratitude; this dissertation would not have happened without you. And to my brother, Ransom, whose actions encouraged me to pursue engineering as a career.

Acknowledgments

I owe my gratitude to all the people who have made this thesis possible and because of whom my graduate experience has been one that I will cherish for the rest of my life.

First and foremost I'd like to thank my advisor and co-advisor, Professor Michael Pecht and Dr. Michael Azarian, for giving me the invaluable opportunity to be a part of the team at the Center for Advanced Life Cycle Engineering (CALCE). Prof. Pecht has always made himself available for help and advice. It has been a pleasure to work with and learn from him. Without Dr. Azarian's extraordinary ideas and experimental expertise, this thesis would have been a distant dream. Many of the experiments and analytical methods used in this thesis were initiated due to conversations and suggestions from him. Many thanks are due to Professor Thomas Antonsen, Professor Abhijit Dasgupta, Professor Bongtae Han, and Professor Peter Sandborn for agreeing to serve on my thesis committee and for sparing their invaluable time reviewing this research.

My colleagues at CALCE have enriched my graduate life in many ways and deserve a special mention. Anto Peter and Chris Hendricks provided advice and friendship for many years both in and out of the lab. My interactions with Arvind Vasan, Jing Tian, Guru Prasad, and Dr. Myongsu Kang (a man whose memory will be cherished by all who knew him) been very fruitful. I'd also like to thank Cheryl Wurzbacher, David Eisner, and Justin Cline for being, among many other things, most excellent Friday lunch partners.

I would also like to acknowledge help and support from some of the staff members. Dr. Robert Utter's technical help and advice is highly appreciated. He has always made himself available for assistance with tough chemistry problems. The nanoindentation and FTIR work would not have been possible without the patience and guidance of Dr. Carlos Morillo. Of course, Dr. Bhanu Sood deserves mention for his role as CALCE lab director during my first few years there.

I owe my deepest thanks to my family - my wife Kylie has always stood by me and guided me through my career, and has pulled me through against impossible odds at times. Words cannot express the gratitude I owe her. My parents and sister have been steady and encouraging throughout my entire life, and this is something I highly value.

It is impossible to remember all, and I apologize to those I've inadvertently left out.

Table of Contents

List of Tables

List of Figures

List of Abbreviations

j	imaginary unit $\left(\sqrt{-1}\right)$
ω	angular frequency (rad/s)
f	frequency in Hertz
C	capacitance (F)
L	inducatance (H)
R	AC or DC resistance (Ω)
R_i	insulation resistance (Ω)
X	reactance (Ω)
Z	impedance (Ω)
ρ	correlation coefficient (Pearson or Spearman)

AWG	American Wire Gauge
FTIR	Fourier transform infrared (generally refers to a method of infrared (IR) spectro
NEMA	National Elecronics Manufacturing Association
NRC	Nuclear Regulatory Commission
ORNL	Oak Ridge National Laboratory
SIF	Safety instrumented function
SNL-NM	Sandia National Laboratory–New Mexico
SOV	solenoid-operated valve

Chapter 1: Introduction

1.1 Motivation

Electromagnetic coils are fundamental energy conversion and transformation components of many systems, widely used in motors, transformers, and solenoids, which are subsequently used in intelligent control of electro-pneumatic braking systems in motor vehicles, diesel fuel injection control systems, automobile transmission control, process control, and in critical safety-instrumented functions. A few examples are shown below in Figure 1.1. Their functionality lies in the conversion of electrical energy to mechanical energy as is the case with electric motors or solenoid-operated valves (SOVs); or alternately, as with alternators, the conversion of mechanical energy to electrical energy. In the case of transformers, electrical energy is transferred from one circuit to another.

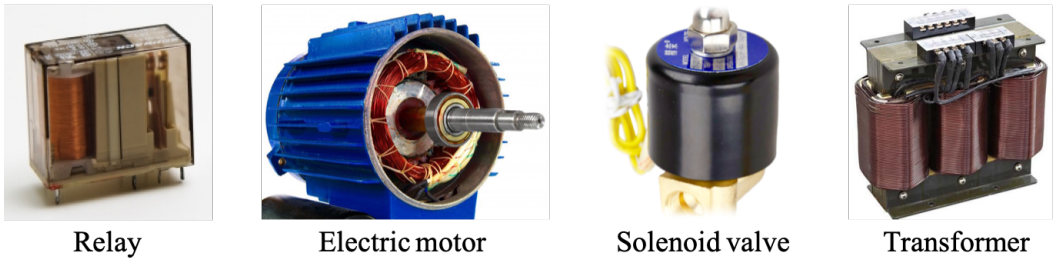

Figure 1.1: Examples of electromagnetic coil uses

A study conducted by Oak Ridge National Laboratory (ORNL) [1–3] showed that over 50% of solenoid-operated valve (SOV) failures in U.S. nuclear power plants were attributed to electromagnetic coil faults (e.g., coil opens and shorts). The breakdown of the ORNL study on SOVs is shown in Figure 1.2. The IEEE Motor Reliability Working Group [4, 5] found that electromagnetic coil insulation problems contribute to one-quarter of motor failures, while Thorsen and Dalva found the same contribution to be approximately one-third [6]. A survey of 1199 hydrogenerators carried out by CIGRE (International Council on Large Electric Systems) study committee SC11, EG11.02 gave detailed results of 69 incidents, finding that 56% of the failed machines showed insulation damage [7]. Downtime caused by these unplanned outages can be quite costly [8], hence identifying insulation degradation at an early stage of progress can reduce operations and maintenance costs by enabling condition-based maintenance or replacement.

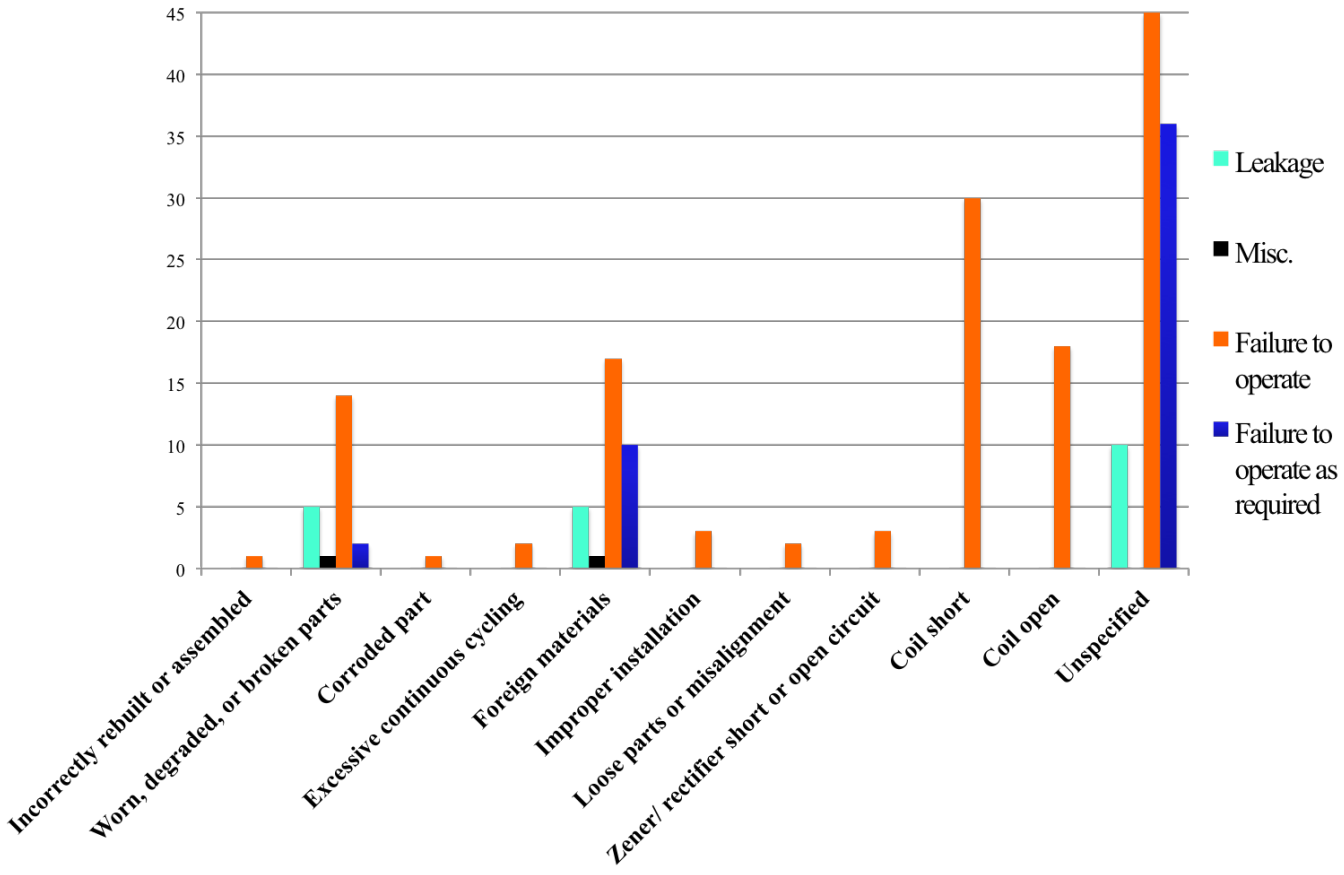

Figure 1.2: SOV failure data in the nuclear industry as compiled by ORNL [1]

Electromagnetic coils are constructed of magnet wire, which is defined by the NEMA 1000 standard as: an insulated electrical conductor, most commonly copper or aluminum that when wound into a coil and energized creates a useful electrical field [9]. A cross section of AWG38 (American Wire Gauge 38) with a copper conductor is shown in Figure 1.3. In this figure, the diameter of the conductor is shown along with the thickness of the insulation. The insulation, or enamel, is separated into thermal classes based on the temperature at which the material is expected to survive for 20,000 hours. This is computed by exposing the material to 3 different elevated temperatures (at which the polymer is expected to degrade relatively quickly) and determining the times when the material experiences dielectric breakdown. The times and temperatures are then fit to an Arrhenius model, and the temperature at which the model meets 20,000 hours is considered as the rated temperature. Some common classes are:

- Class A: 105 °C
- Class B: 130 °C

- Class F: 155 °C
- Class H: 180 °C

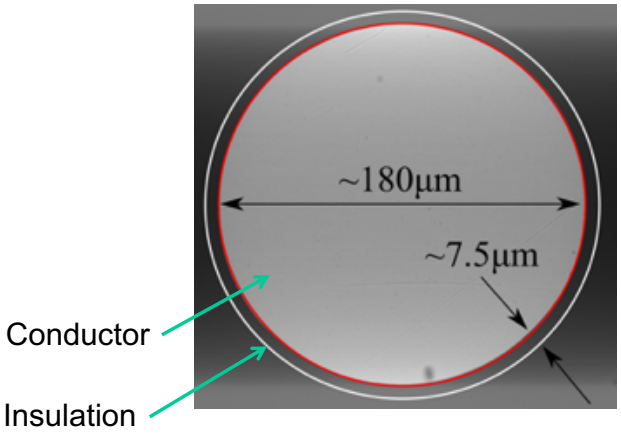

Figure 1.3: Cross sectional view of AWG 38 magnet wire with a copper conductor (outer edge outlined in red) and single build polyester-imide insulation (outer edge outlined in white).

Angadi *et al.* [10,11] conducted accelerated testing of SOVs and concluded that SOVs are susceptible to "coupled electrical-thermal-mechanical failure mechanisms." The stresses driving these mechanisms were described as follows: Joule heating of the conductor wire from electrical power subjects the insulation to thermal stresses from the temperature rise and mechanical stresses from the expansion of the conductor. One challenge is to monitor the health of the electromagnetic coil insulation in-situ. SOVs are often applied in safety-instrumented functions (SIFs), with between 2-4% of all solenoid valves used in chemical process plants being devoted to use in SIFs [12]. SIFs require high reliability, but are generally in-line with the process, rendering SIF functional tests disruptive and costly. A method that can assess the in-situ health of SOV electromagnetic coil insulation can improve the reliability of SIFs without affecting the process.

The degradation of magnet wire enamel is a primary reason that shorts form in the coil [10, 11, 13]. Magnet wire enamel is generally a polymeric material, hence the study of magnet wire enamel is akin to studying the degradation of polymers.

Thermal oxidation initiates when heat induces free-radical formation at some point along the polymer chain. A sequence of reactions follows, first proposed by Bolland and Gee [14], generally referred to as the basic auto-oxidation scheme: chain initiation, chain propagation, chain termination. Oxidation introduces acid groups into the polymeric insulation, which can alter the electrical characteristics of the insulation. The process results in a polymer with a lower average molecular weight, embrittling the polymer and causing the polymer to form cracks, and thus changing the mechanical properties [15, 16]. Depolymerization is a gradual process that converts polymers into monomers. This phenomenon, where polymer chains break into

shorter units, occurs in all polymers including cellulose at elevated temperatures even in the absence of oxygen. This reaction is, in general, a much slower one than oxidation, but at high temperatures, it can become an important factor.

Similarly, when a polymer is exposed to moisture, it can undergo a hydrolysis process, which also results in polymer chain scission leading to lower molecular weight and increased deformation at low stresses (i.e. decreased elastic modulus). Moisture exposure can also result in absorption of moisture, leading to changes in the mechanical properties, a reduction of the glass transition temperature, T_g, and changes in the dielectric properties of the polymer [15, 16]. Moreover, exposure to high humidity/moisture environment can lead to delamination of the enamel from the conductor. However, the humidity level can be tempered by the local temperature around the coil. In other words, the humidity level of the environment in which the coil is used will likely be greater than the humidity in the immediate vicinity of the powered electromagnetic coil. This is due to the Joule heating of the coil and its effects on the local temperature of the coil, which generally drive down relative humidity.

1.2 A Preliminary Experiment

To gain understanding about insulation degradation in electromagnetic coils, an experiment was performed. The goal of this experiment was to purposefully degrade magnet wire insulation, while taking electrical impedance measurements, in order to explore health monitoring capability of electrical measurements.

Figure 1.4: SOV used in 80 °C/50 % RH experiment

1.2.1 Experimental Setup

A generic solenoid valve (shown in Figure 1.4) with a DC resistance of about 10.3 Ω was aged in a temperature/humidity chamber at its rated temperature of 80 °C and a relative humidity (RH) of 50 %RH. (Note: the valve was unrated with regards to relative humidity.) The insulation material was not disclosed in the data

sheet, but using Fourier transform infrared (FTIR) spectroscopy, the material was found to be a combination of polystyrene and polyethylene terephthalate. The wire gauge was also undisclosed in the data sheet, but the diameter was measured to be about 380 µm and the insulation thickness was measured to be about 27 µm, hence the magnet wire was determined to be AWG (American Wire Gauge) 26.5. A turn-to-turn short formed in the SOV electromagnetic coil after about 3120 hours. Considering the function of the insulation is to provide electrical isolation, 3120 hours is taken to be the time at which the insulation failed.

As the coil insulation was degraded, an LCR (inductance-capacitance-resistance) meter was used to take impedance measurements of the coil. The reason behind taking impedance measurements of the coil is as follows. If the coil is viewed from a lumped parameter viewpoint, then the relationship between two turns of wire can be visualized using the circuit in Figure 1.5.

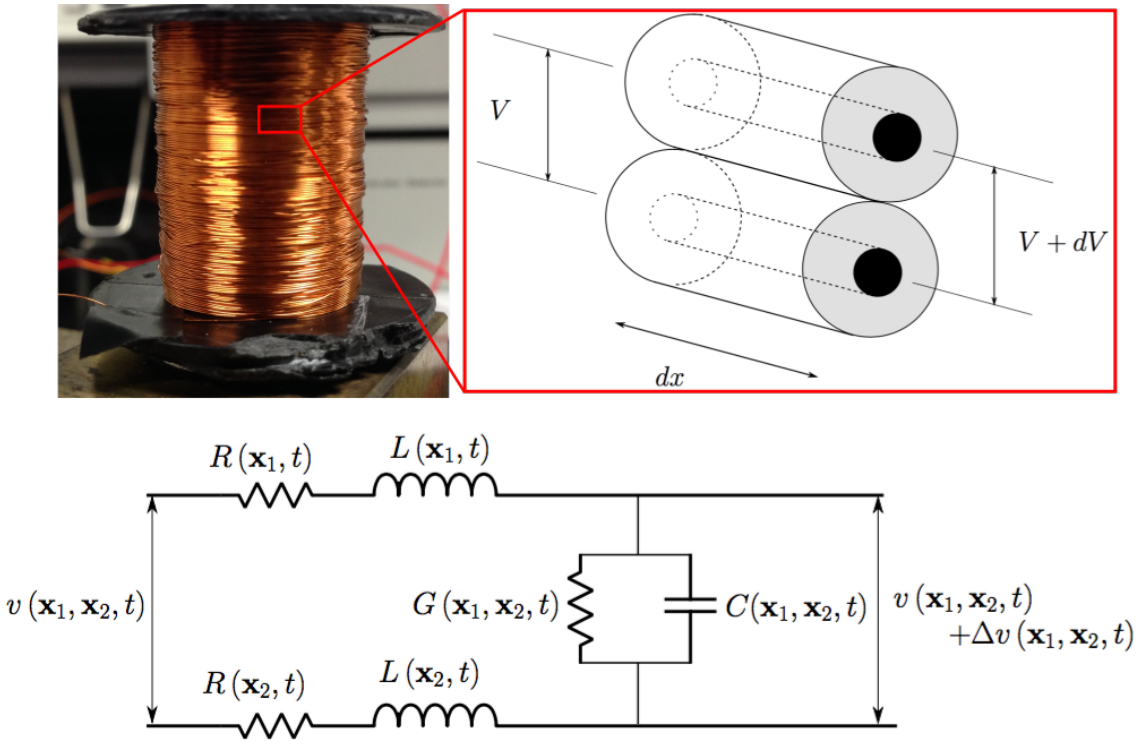

Figure 1.5: Theoretical lumped parameter model for an electromagnetic coil

Hence, each turn of the coil has a resistance per unit length (based upon the conductor material, cross-sectional area, and turn circumference), an inductance per unit length, and the insulation has a capacitance and conductance per unit length (based upon the insulation material, thickness, and turn-to-turn geometry). In the model shown in Fig. 1.5, these parameters are dependent upon the location in the coil (i.e., $\mathbf{x}_1$ or $\mathbf{x}_2$) and the time, t. These parameters will interact among all the turns of the coil resulting in a terminal impedance in which all the parameters are

represented, such that $Z_{total} = f(\omega, \boldsymbol{R}, \boldsymbol{L}, \boldsymbol{C}, \boldsymbol{G})$, where the bold letters represent the total values of each parameter. Therefore, by taking bulk impedance measurements, the values of insulation conductance and capacitance will be captured, which can be useful in characterizing the health of the insulation.

In this experiment, the SOV was removed from the temperature/humidity chamber once every 48 hours, and the impedance spectrum was measured. Using an Agilent 16047E four-terminal fixture, the coil was connected to an Agilent E4980A LCR meter and impedance was measured at frequencies ranging from 20 Hz-2 MHz (501 frequencies equally spaced in the base-10 logarithmic domain), with a root mean square voltage signal of 500mV. The measured spectra are considered to be isothermal with the coil DC resistance used as a proxy for coil temperature, such that once the DC resistance reached a steady-state value, impedance measurements were taken. Hence, each impedance measurement was taken at room temperature, which ranged between 22 °C and 26 °C. The measurement time varied according to the frequency from 220-480 ms. This measurement setup for the SOV electromagnetic coil terminal impedance is illustrated in Figure 1.6.

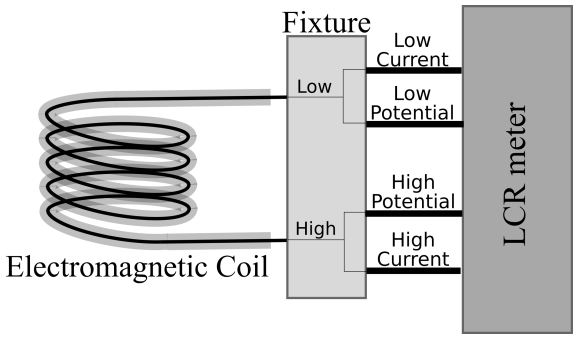

Figure 1.6: Measurement setup for terminal impedance measurements of the SOV.

At each frequency, 8 impedance measurements were taken sequentially and averaged to produce one final output measurement. The impedance data can be represented as a time vector and impedance matrix, as shown in Equation 1.1.

$$\mathbf{t} = \begin{bmatrix} t_0 & t_1 & \cdots & t_{T-1} & t_T \end{bmatrix}$$

$$\mathbf{Z} = \begin{bmatrix} Z(t_0, f_1) & Z(t_1, f_1) & \cdots & Z(t_{T-1}, f_1) & Z(t_T, f_1) \\ Z(t_0, f_2) & Z(t_1, f_2) & \cdots & Z(t_{T-1}, f_2) & Z(t_T, f_2) \\ Z(t_0, f_3) & Z(t_1, f_3) & \cdots & Z(t_{T-1}, f_3) & Z(t_T, f_3) \\ \vdots & \vdots & \ddots & \vdots & \vdots \\ Z(t_0, f_{N-1}) & Z(t_1, f_{N-1}) & \cdots & Z(t_{T-1}, f_{N-1}) & Z(t_T, f_{N-1}) \\ Z(t_0, f_N) & Z(t_1, f_N) & \cdots & Z(t_{T-1}, f_N) & Z(t_T, f_N) \end{bmatrix} \tag{1.1}$$

In this experiment, $N = 501$ ($f_{501} = 2$ MHz) and $T = 41$ ($t_{41} \approx 3120$ hours). Some analysis methods are discussed in the next subsections.

1.2.2 Electrical Impedance

Electrical impedance, similar to resistance, is an expression of the opposition to electron flow and is measured in Ohms (Ω). It is complex-valued and frequency-dependent, and can be expressed as: $Z(\omega) = R(\omega) + jX(\omega)$, where $j = \sqrt{-1}$ is the imaginary unit. The real part is called resistance and the imaginary part is called reactance. Resistance is the opposition to electrical current, and reactance is the opposition to a change in voltage or current due to capacitive or inductive behavior. Reactance is generally expressed as a combination of inductive and capacitive behavior: $X(\omega) = X_L(\omega) + X_C(\omega)$. The impedance of an ideal resistor is purely real (R), while the impedance of an ideal inductor ($j\omega L$) or capacitor $\left((j\omega C)^{-1}\right)$ is purely imaginary. Positive reactance is considered as inductive reactance, while negative reactance is considered as capacitive reactance. The resonance of any given circuit is the frequency where inductive reactance is exactly balanced by capacitive reactance; i.e., $X(\omega_r) = X_L(\omega_r) + X_C(\omega_r) = 0$.

1.2.3 Spearman Rank Correlation Coefficient

When searching for a health indicator to be used in a diagnostic or prognostic application, a desirable trait is for the health indicator to trend monotonically over the specified lifetime of the component or system. The Spearman rank correlation coefficient is a measure of the monotonic relationship between two variables and can be employed to discover features useful for health monitoring. Essentially, the Spearman correlation coefficient is computed in the same manner as the Pearson correlation coefficient, except the raw data is transformed into rankings. For a dataset of size n and where each point is distinct and non-repeated, the Spearman rank correlation coefficient is calculated as:

$$\rho = 1 - \frac{6}{n\left(n^2 - 1\right)} \sum_{i=1}^{n} d_i^2 \tag{1.2}$$

In this computation, the raw samples, X_i, Y_i, are converted into ranks x_i, y_i, and $d_i = x_i - y_i$ is the distance between the ranks. Identical values (rank ties or value duplicates) are assigned a rank equal to the average of their positions in the ascending order of the values. The Spearman correlation coefficient ranges from $+1$ to -1 such that when $\rho = +1\,(-1)$, each of the variables is a perfect monotonically increasing (decreasing) function of the other.

The Spearman correlation coefficient can be used to measure linear or non-linear monotonic relationships between two variables. Hence, the measure is more general than the Pearson correlation coefficient, which measures only the linear correlation between two variables.

1.2.4 Experimental Results

The time evolution of the impedance spectrum response to the temperature/humidity aging is shown in Figure 1.7. In total, there were 42 impedance spec-

trum measurements, including the spectrum measured when the short was formed.

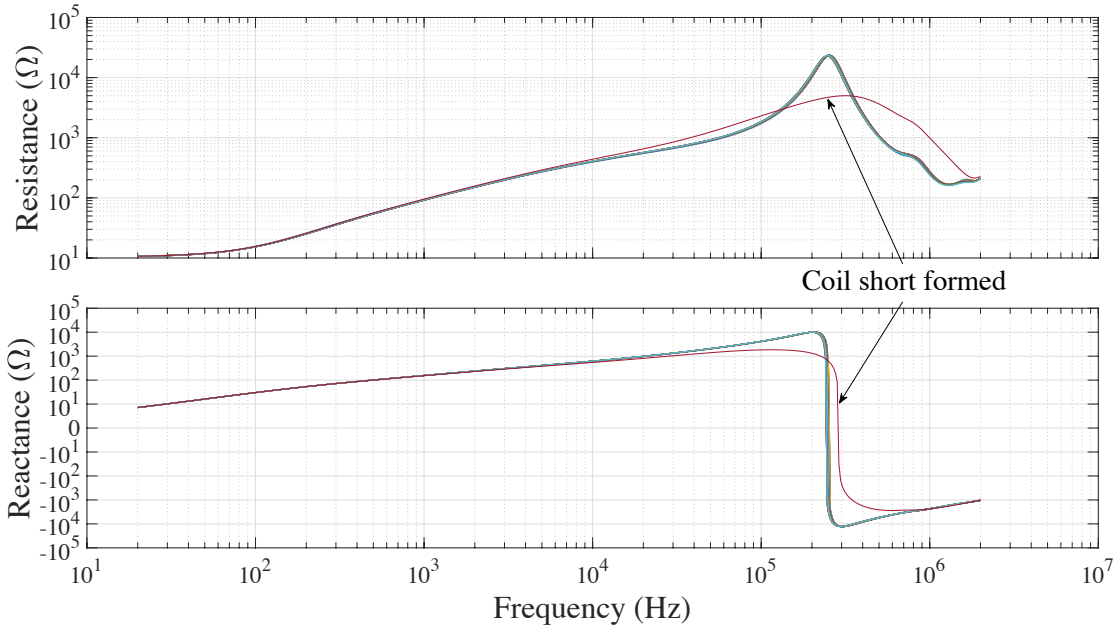

Figure 1.7: Time evolution of solenoid valve electromagnetic coil impedance spectrum (above: resistance; below: reactance) resulting from exposure to 80 °C/50% RH environment. Every impedance measurement up to and including the first measurement of a short is shown, totaling 42 separate impedance spectra. The initial resonant frequency was 251.5 kHz.

Despite a 2.5% decrease in the resonant frequency prior to the formation of the short, the spectra do not visually reveal the magnitude of shifts that were experienced by the coil prior to the formation of the short. Using the Spearman rank correlation coefficient, each frequency can be independently assessed as an indicator of aging [17]. The Spearman correlation coefficient can be used to identify regions of the frequency spectrum that closely correspond to the exposure time. This is important when attempting to find a health indicator for diagnostics and prognostics. The Spearman correlation coefficient for all frequencies, separated for resistance and reactance, was calculated using the measurements at each frequency as a time series (i.e., each row of the impedance matrix from Equation 1.1) and then correlating these data with the time vector.

Figure 1.8 shows the correlations of all frequencies to the total exposure time prior to the formation of the turn-to-turn short. The frequencies with highest correlations must be further investigated to understand the trends and find features to use for insulation diagnostics and prognostics. However, some preliminary observations can be made. First, the resistance measurements at frequencies below resonance are positively correlated with the exposure time, while at frequencies above resonance, resistance is negatively correlated with aging time. Second, reactance is positively correlated with exposure time, except for a small region of frequencies around reso-

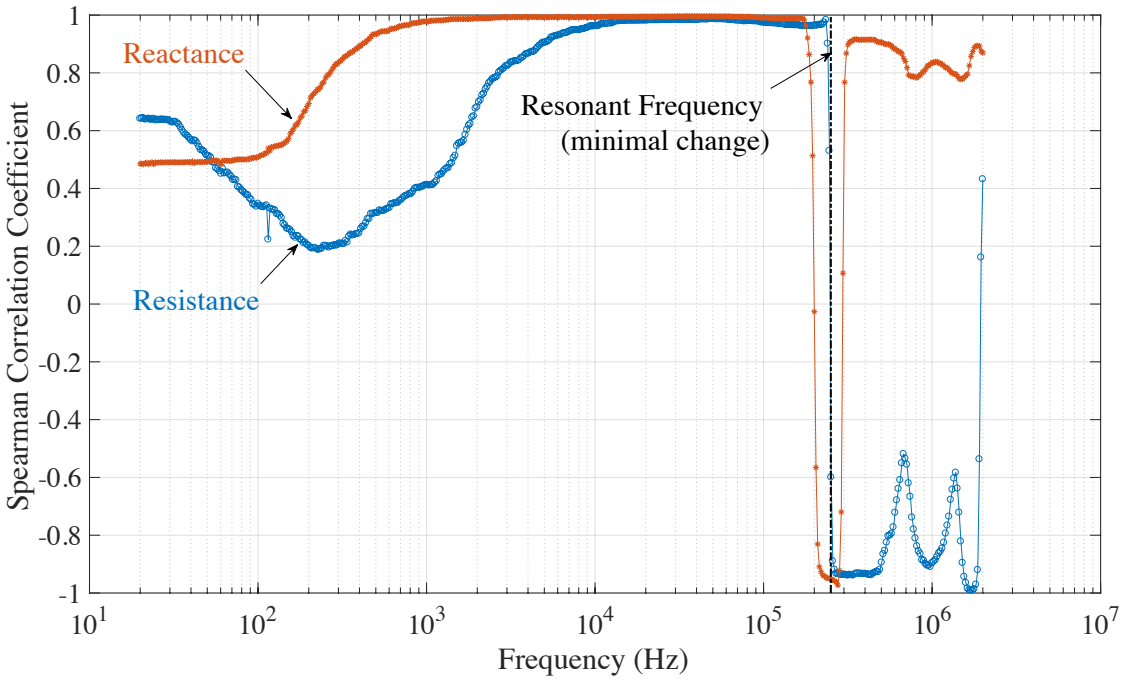

Figure 1.8: Spearman correlation coefficient spectrum for 80 °C/50% RH aging (using data prior to formation of coil short). The movement of the resonant frequency is not shown since the resonant frequency only decreased by about 2.5% prior to insulation failure.

nance where reactance is negatively correlated with exposure time. The resistance and reactance measurements for some of the higher correlated frequencies are shown in Figures 1.9 and 1.10. The Spearman correlation coefficients for each frequency are shown in the figures. In the reactance figures, the mathematical expressions of inductive and capacitive reactance are shown.

The measurements presented in Figures 1.9 and 1.10 show that key frequencies in the impedance spectrum contain information that can be used to perform prognostics for the coil insulation. Furthermore, it should be noted that the time series at these frequencies showed much greater sensitivity to insulation health than the coil resonant frequency, which has been proposed as an insulation health indicator in past research. In this experiment, the resonant frequency decreased by about 2.5%, while reactance at 276.1 kHz decreased by about 25% and resistance at 240.4 kHz increased by about 14%.

This experiment showed how impedance data can be analyzed to reveal frequencies at which the measurements are sensitive to insulation degradation. Using the Spearman correlation spectrum, frequencies can be identified where impedance measurements thereof can be used for insulation prognostics. Furthermore, the Spearman correlation spectrum raises several research questions regarding the degradation process of insulation and how the degradation affects the electromagnetic coil

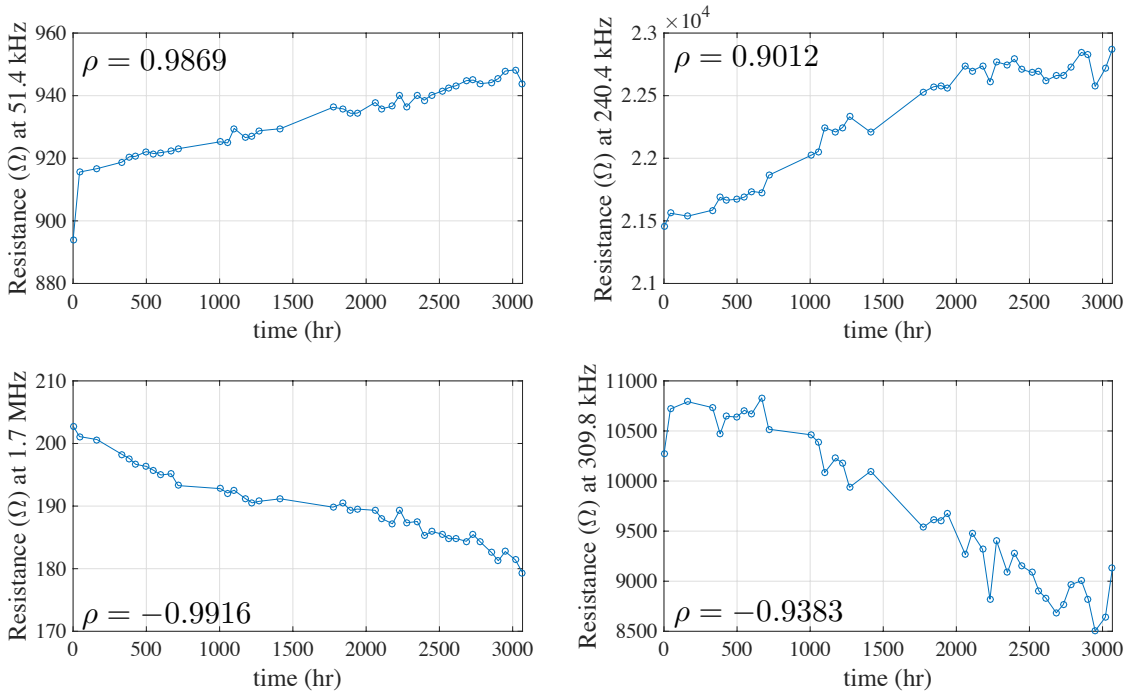

Figure 1.9: Resistance time series resulting from temperature/humidity exposure at (clockwise from upper left to lower left): 51.4 kHz; 240.4 kHz; 1.7 MHz; 309.8 kHz. The Spearman correlation coefficients for each time series are shown.

impedance. As discussed previously, resistance ($\mathrm{Re}\{Z(\omega)\}$) was positively correlated with aging time at frequencies below resonance and negatively correlated at frequencies above resonance. Reactance ($\mathrm{Im}\{Z(\omega)\}$) was positively correlated with aging time at most frequencies above and below resonance, except a small region of frequencies around resonance. What changes in the insulation material and/or geometry caused the impedance to change in such a manner? What do the changes in the impedance measurements tell us about the physical state of the insulation material? Are certain frequencies in the spectrum more sensitive to changes in the insulation properties?

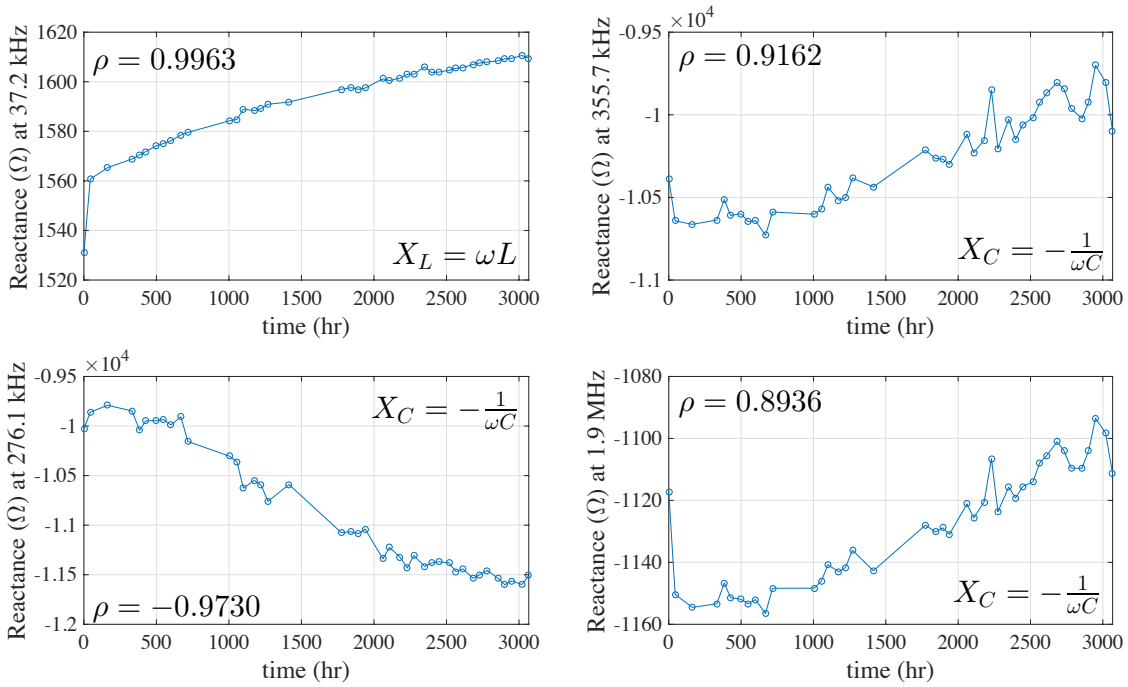

Figure 1.10: Reactance time series resulting from temperature/humidity exposure at (clockwise from upper left to lower left): 37.2 kHz; 355.7 kHz; 276.1 kHz; 1.9 MHz. The Spearman correlation coefficients for each time series are shown.

Chapter 2: Literature Review

In the following chapter, a thorough review of the available literature on insulation health monitoring and insulation material analysis is presented. This is done to expose the research gaps and illuminate available avenues for further research.

2.1 Traditional Approaches to Insulation Health Monitoring

Traditional methods of insulation health monitoring generally rely on direct contact with the insulation under investigation. In 2004, Dr. Greg Stone *et al.* [13] released the book *Electrical Insulation for Rotating Machines: Design, Evaluation, Aging, Testing, and Repair*, which has become a standard reference for insulation used in rotating machinery. In the book, the available methods of diagnostics for insulation were discussed. These methods include the measurement of the dissipation factor (DF), insulation capacitance (C), polarization index, insulation resistance (IR), insulation power factor, and offline partial discharge. A common theme for the methods discussed is direct access to the insulation. In other words, in order to measure the insulation capacitance, for example, one must have the ability to place electrodes outside the insulation, in effect using the insulation as a dielectric between the inner conductor and the outer electrodes, as shown in Figure 2.1. (An alternate technique for measuring insulation capacitance was discussed by Sheldon and Bowler in 2014 [18], yet this still requires direct access to the insulation under investigation.) The goal of these methods is to provide a parameter (or parameters) that can be measured and trended over time, thus providing a means to understand when the the coil should be replaced prior to insulation failure. However, these methods cannot, in general, be applied in-situ, nor to systems in which the coil is inaccessible, such as when an SOV electromagnetic coil is encased in epoxy and/or enclosed in a cover.

Since these methods are difficult or impossible to apply in-situ, other methods are available to provide a measure that is sensitive to insulation degradation. For high-voltage machines, partial discharge (PD) has been used as such a measure in insulation health-monitoring activities. According to Tavner [19]: "Electrical discharges are transitory, low-energy disturbances that radiate electromagnetic, acoustic, and thermal energy. That conducted energy cause perturbations to the voltage and current waveforms at the terminals." There is a vast body of literature describing how characteristics of PD can be used as diagnostic and prognostic features for insulation health monitoring [13, 20–25]. Generally, online partial discharge testing is only applicable to high-voltage (generally > 2.3kV) machines. (It is worth men-

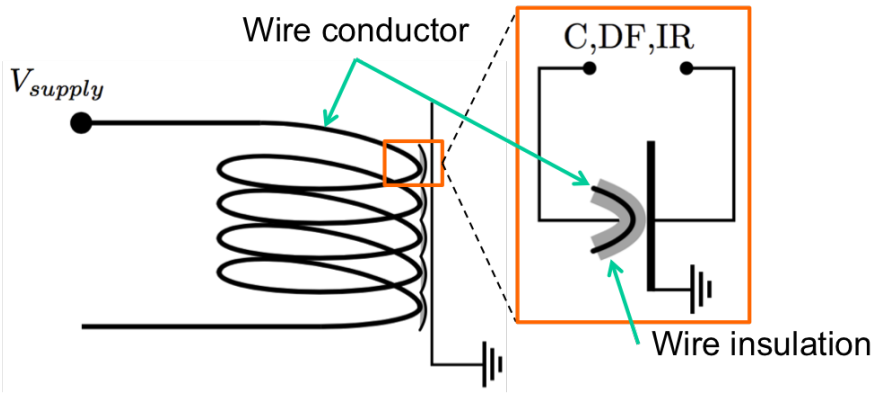

Figure 2.1: Traditional insulation electrical parameter measurement

tioning that machines driven by voltage inverters can experience over-voltages and surge currents due to pulse-width modulated (PWM) signals, leading to PD even in medium- to low-voltage induction machines [26, 27].) Hence, for a system like the SOV, which operates in 120 VAC and generally $<$ 30 VDC, partial discharge monitoring is infeasible.

Others however, have developed methods of investigation into the health of electromagnetic coil insulation that do not rely on the need for direct access to the coil insulation. The idea to measure broadband impedance as a method of predicting stator-winding failure was first put forth in 2001 and 2002 in a series of patents by Kendig and Rogovin [28, 29]. Yet, the methods were never fully elucidated in the technical literature, hence the theoretical and experimental work has continued to investigate the use of impedance in electromagnetic coil health monitoring.

2.2 Coil Impedance Modeling and Measurement

ORNL released a follow-up study to their investigation into solenoid valve failures in nuclear plants in the United States, where Dr. Robert Kryter attempted to find methods of performing health monitoring of solenoid valves [2, 3]. He proposed a set of methods for monitoring the health of the valves mechanical components as well as the electromagnetic coil. In order to monitor the health of the electromagnetic coil, Dr. Kryter suggested the use of an equivalent circuit model (ECM). His suggested ECM is shown in Figure 2.2, which is also a commonly applied model for inductors [30–32].

To test this ECM, Kryter tested a healthy and a faulty solenoid valve by holding the valve at 30 VDC and measuring the dynamic voltage response after stepping the voltage down to 0 VDC. The healthy valve coil was new, while the faulty valve coil had $\approx 6\%$ of its turns shorted. The dynamic responses are shown in Figure 2.3. From the data gathered in these dynamics responses, Kryter was able to fit the parameters of the ECM using Equations 2.1 - 2.3.

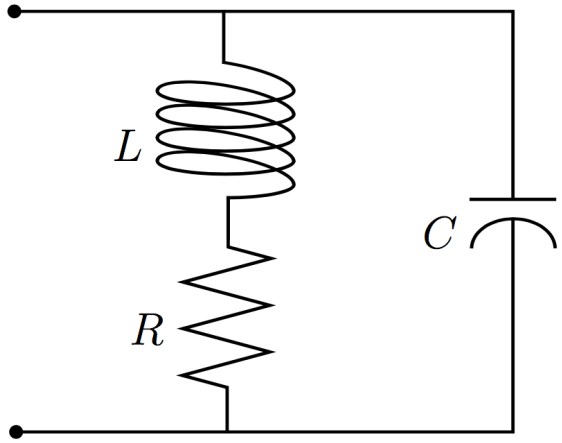

Figure 2.2: Equivalent circuit model used by Kryter [2, 3] in his simulations of a healthy and faulty SOV electromagnetic coil.

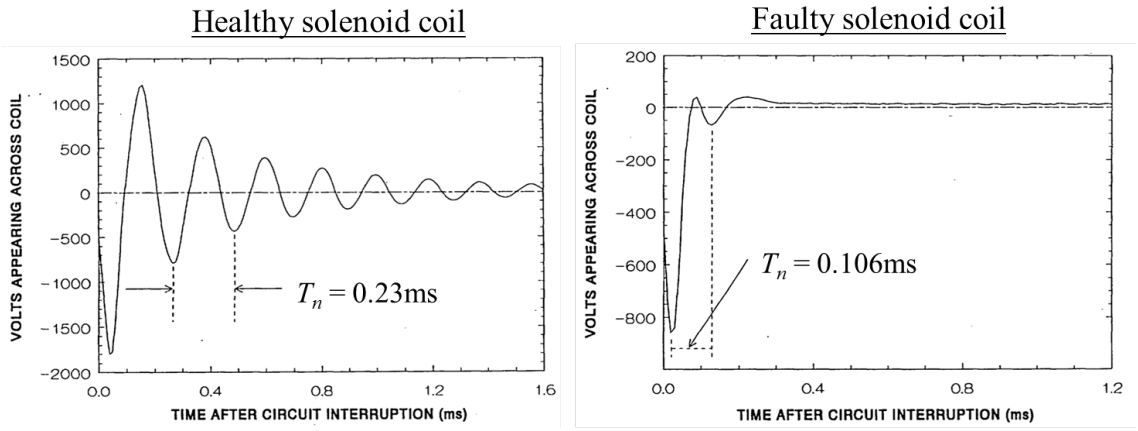

Figure 2.3: Dynamic responses of healthy (left) and faulty (right) SOV coils after stepping down to 0 VDC from 30 VDC [3].

$$V(t) = \frac{V_0 T_n}{2\pi L} e^{-\alpha t} \sin\left(2\pi \frac{t}{T_n}\right) \tag{2.1}$$

$$T_n = 2\pi \sqrt{\frac{1}{LC} - \frac{R^2}{4L^2}} \tag{2.2}$$

$$\alpha = \frac{R}{2L} \tag{2.3}$$

Although he was able to replicate the behavior of the healthy coil, he found that he was unable to use the ECM to replicate the measured responses of the faulty coil. He thusly concluded that the ECM was not sensitive enough to perform health monitoring of the SOV electromagnetic coil insulation.

Perisse *et al.* [33] constructed a complex equivalent circuit model (shown in Figure 2.4), where Ls represents the overhang and slot section inductance, Rs is the equivalent series resistance, Ci is the turn-to-turn insulation capacitance, and Ri is the dielectric loss resistance. He showed that changes in the turn-to-turn capacitance of the electromagnetic coil (the parameter Ci was changed in a bulk fashion) were reflected in the coil resonant frequency, finding that insulation capacitance was inversely related coil resonant frequency. He only simulated the changes in coil resonant frequency in response to changes in insulation capacitance, neglecting how changes in other electrical parameters, such as the insulation resistance, might affect the coil impedance response.

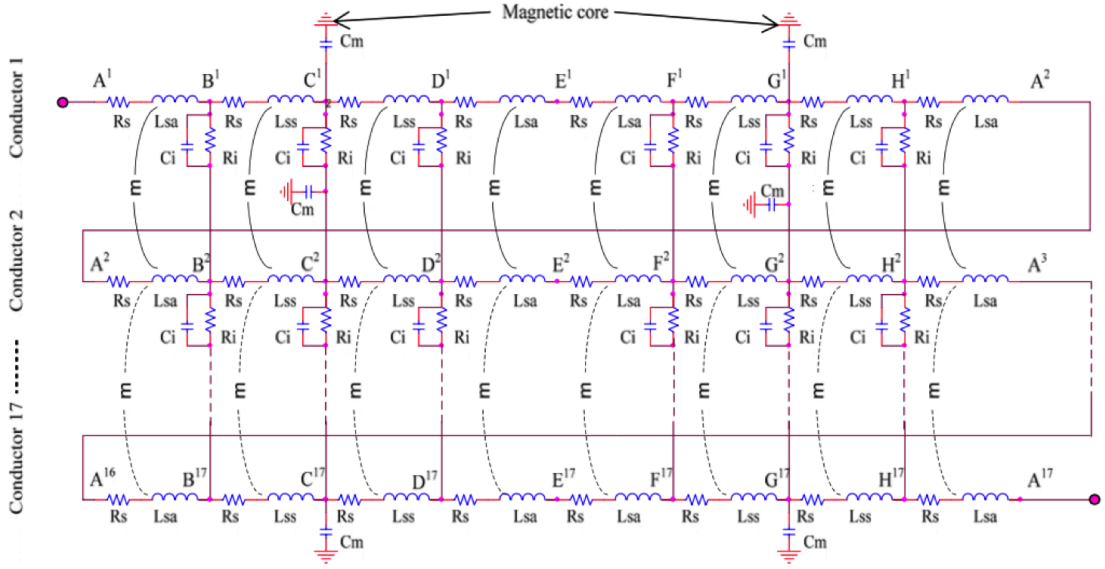

Figure 2.4: ECM used by Perisse *et al.* [33] in their simulations testing the effect of insulation capacitance migration on coil resonant frequency.

In 2009, Perisse *et al.* [34] tested a method for measuring AC motor coil resonant impedance frequency over a small range of frequencies while an AC motor was powered, and presented a decision-making process regarding the aging of the machine insulation. In this experiment, it was observed that the resonant impedance shifted to lower frequencies as the motor coil aged. The failure threshold was set at 95% of the healthy resonant frequency; no explanation was provided for this choice of failure threshold. Moreover, further experimental analyses (shown in the present study) have shown that resonant frequency is not the most sensitive indicator for insulation health.

Neti and Grubic [35] also constructed an extensive ECM for a motor coil, showing results similar to those found in [33]. Next, they connected variable capacitors and resistors in parallel with motor coils and measured the impedance response of the system. The variable capacitors and resistors were intended to simulate changes in the turn-to-turn capacitance and resistance and the ground-wall capac-

itance and resistance (insulation between the electromagnetic coil and the external metal casing, typically seen in electric motors). Their experimental measurements showed that variations in the parallel resistors and capacitors produced changes in the impedance response of the motor coils. Unfortunately, no experimental data were presented showing how aging produced changes in the insulation capacitance or insulation resistance. Nor is it clear how connecting electrical components in parallel relates to the changing electrical properties of insulation.

2.3 Temperature-driven Insulation Impedance Changes

Werynski *et al.* [36] investigated the ability of a magnetic field sensor to detect changes in the high-frequency resonant impedance of a motorette. (Motorettes are designed to be small-scale models of electric motor stator windings [37, 38].) First, however, the group placed twisted pairs (i.e., a pair of magnet wires twisted together, as shown in Figure 2.5) with polyester-imide insulation under thermal stress and found that the insulation capacitance (measured at an undisclosed frequency) increased as breakdown voltage (measured at 50 kHz) decreased. Since breakdown voltage is a measure of insulation degradation, this study showed that as the insulation degraded, the insulation capacitance increased. Then they measured the phase shift between an injected high-frequency signal and the resulting magnetic field. They claimed that this phase difference could be used as a health indicator for the insulation, but did not perform any life testing to verify that a magnetic field sensor could be used in a health-monitoring capacity.

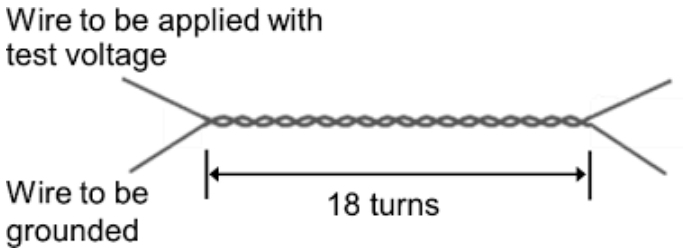

Figure 2.5: Example of a magnet wire twisted pair [39].

A contradicting set of studies was published by Lee *et al.* [40] and Younsi *et al.* [41], who used a high-sensitivity current transformer to measure the differential current of the line and neutral end of each phase winding of a three-phase AC motor. The results showed that as the insulation aged, the loss angle decreased, where the loss angle was defined as $\delta = \tan^{-1}\left(\tilde{I}_R/\tilde{I}_C\right)$, and I is the current, and the subscripts R and C refer to resistive or capacitive, respectively. The authors of this study concluded that the reduction in conductivity was faster than loss in capacitance, which is contrary to the claim by Werynski *et al.* that the capacitance increased over the aging period.

In 2011 and 2013, Savin *et al.* [42, 43] performed testing on twisted pairs of magnet wire with two-layer polyester-imide/polyamide-imde insulation. He showed

that as the pairs aged at elevated temperatures, the partial discharge inception voltage (PDIV), which is an indication of insulation degradation, decreased as the turn-to-turn capacitance (measured at 10 kHz) increased.

In 2008, Diaham *et al.* [44] aged polyimide film at 300 °C in air and N_2 for up to 167 hours. They found that the electrical dissipation factor decreased in air at frequencies between 100 Hz and 200 kHz, but increased in N_2 at frequencies between 0.8 Hz and 1 MHz, where the dissipation factor is expressed as:

$$\mathrm{DF}\left(\omega\right) = \tan\delta\left(\omega\right) = \frac{\mathrm{Im}\left\{\varepsilon\left(\omega\right)\right\}}{\mathrm{Re}\left\{\varepsilon\left(\omega\right)\right\}} = \frac{\varepsilon''\left(\omega\right)}{\varepsilon'\left(\omega\right)} \tag{2.4}$$

They also found that during the aging period, the DC conductivity of the polyimide films decreased when aged in air, but increased when aged in N_2. In order to compute the DC conductivity, they used a relationship between low frequency AC conductivity and the DC conductivity as shown in Equation 2.5.

$$\sigma_{AC}\left(\omega\right) = \omega\varepsilon_0\varepsilon''\left(\omega\right) = \sigma_{DC} + K\omega^n \tag{2.5}$$

Li *et al.* [45] aged Kapton® (a commercial aromatic polyimide) at 400 °C, 425 °C, 450 °C, and 475 °C, and measured the real part of permittivity ($\varepsilon'\left(\omega\right)$) at 1 kHz. They showed that as the polyimide aged for up to 5 hours (the polyimide failed after 3 hours at 465 °C), the real permittivity increased. The also measured the dissipation factor (same expression as Equation 2.4) for the polyimide exposed to 475 °C, and found that the dissipation factor increased for frequencies between 1 kHz and 2 MHz.

2.4 Chemical Analysis of Degraded Insulation

Dakin [46] proposed to model insulation deterioration as a chemical rate phenomenon. He suggested that any physical property, P, of an insulation (e.g., tensile strength) was proportional to the concentration, C, of a chemical constituent within the insulation (i.e., $P = f\left(C\right)$). In general, the concentration follows a rate relationship according to:

$$\dot{C} = KC^n \tag{2.6}$$

where n is the order of the reaction. For a first-order reaction (i.e., $n = 1$), concentration follows an exponential relationship of time and a reaction rate constant, K, which in turn follows an Arrhenius relationship:

$$\begin{aligned} C\left(t\right) &= C_0 \exp\left(-Kt\right) \\ K &= A\exp\left(-\frac{B}{T}\right), \end{aligned} \tag{2.7}$$

where A and B are constants and T is the absolute temperature. Dakin examined experimental data from past experiments in which tensile strength as the property under investigation, and plotted the values of tensile strength against aging time at various elevated temperatures. He found that the tensile strength decreased when insulation was exposed to elevated temperatures. The assumption of a first order reaction only approximately fit the experimental data.

Petitgas *et al.* [47] studied the effect of high temperature exposure on copper wire with polyester-imide, polyamide-imide, and polyimide enamels. They found that as the temperature was raised from room temperature to 400 °C at a rate of 2 °C/minute in an N_2 atmosphere, all insulation materials exhibited an increase in electrical $\tan\delta$ (at 1 kHz), indicating higher losses in the dielectric. They also found that after exposure to a 400 °C air atmosphere, all the samples experienced decreased $\tan\delta$ (at an undisclosed frequency). During this timed exposure test, the polyester-imide and polyester-imide/polyamide-imide experienced dielectric breakdown at 35 minutes and 105 minutes, respectively. In all cases except polyimide, and after 2 hours of aging at temperatures greater or equal to 300 °C, chemical changes were detected using Fourier transform infrared (FT-IR) spectroscopy. An example of the detected changes in polyester-imide is shown in Figure 2.6. The authors stated that the emergence of the peak at 1605 cm^{-1} may be the result of the cleavage of some ester functionalities with hydrogen (esters made from ethylene glycol, for example) into carboxylic acid and ethylenic end-chains.

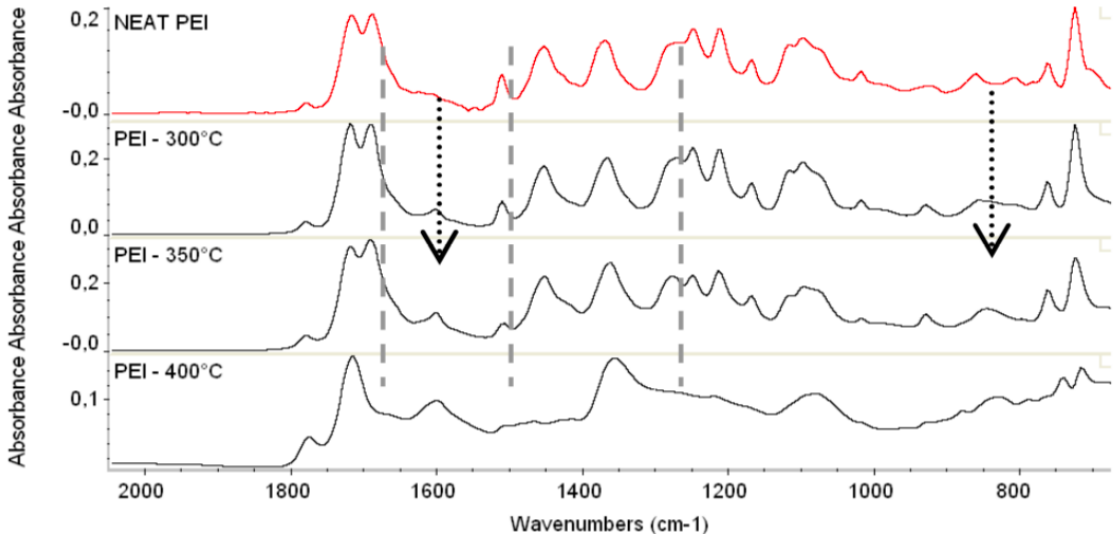

Figure 2.6: Evolution of FTIR spectrum of polyester-imide aged for 2 hours at 300 °C, 350 °C, 400 °C from Petitgas *et al.* [47].

2.5 Mechanical Analysis of Degraded Insulation

A set of studies were performed by Angadi *et al.* [10,11] to understand the effect of Joule heating on the relative displacements of the solenoid valve electromagnetic coil conductor and insulation. In the first study, a finite element analysis model was used to understand the stresses placed on the coil insulation resulting from the expansion of the conductor due to Joule heating. The model results predicted that solenoid coils were subjected to multiple stresses originating with Joule heating of the conductor and causing the insulation to be stressed by conductor expansion and heating, and ultimately failing due to the expansion of the conductor. In the second study, 22 automotive solenoid valves were subjected to accelerated stress conditions. The valves were rated for 12 VDC, 61.2 Hz cycling frequency, and temperatures ranging from -30 °C to 130 °C; the valves were tested at 16.8 VDC, 60 Hz cycling frequency, and 100 °C. After 24 hours of testing, 11 of the 22 valves had failed. The failed valves were analyzed revealing that the insulation between wires failed, allowing the formation of turn-to-turn shorts. One of the failed valves is shown in Figure 2.7.

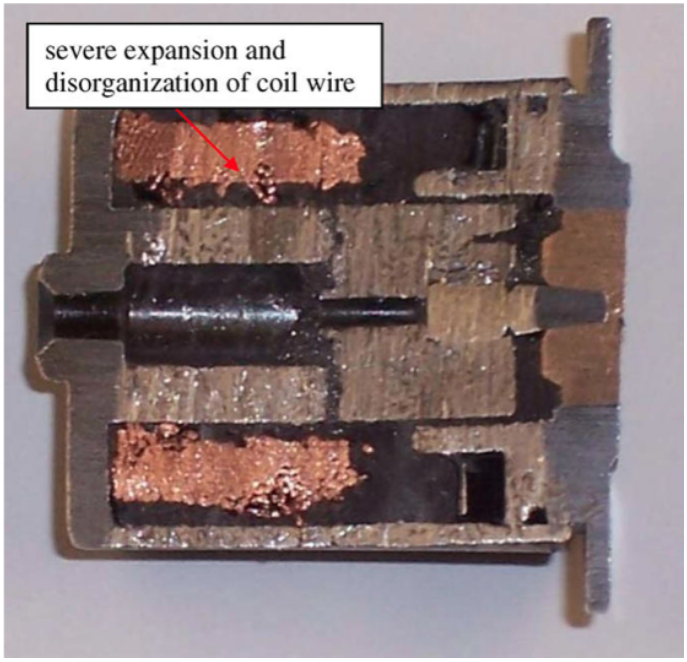

Figure 2.7: Example of a failed automotive SOV from Angadi *et al.* [11].

Petitgas *et al.* [47] measured the mechanical $\tan\delta$ of polyester-imide enamel while increasing the temperature at a heating rate of 3 °C/minute under air atmosphere, with a frequency of 1 Hz, amplitude oscillation 15 μm, and static force of 0.08 Newton. The results showed that as temperature rose from 50 °C to ≈215 °C, the mechanical $\tan\delta$ increased to a maximum, but decreased from ≈215 °C to ≈250 °C. After one run, a second run was performed in which the maximum value of mechanical $\tan\delta$ was shifted to ≈225 °C. The authors concluded that a postcure

effect occurred during the first ramp, causing an increase in the network density of the material. However, this test only explored the change in mechanical $\tan\delta$ during a temperature ramp rather than an exposure test, which would reveal how the insulation mechanical properties change as the insulation ages, perhaps providing insight into a failure mechanism.

2.6 Detection of Insulation Faults

It would be incomplete to neglect the mention of the research into methods of detecting insulation faults (e.g., turn-to-turn shorts). Chow *et al.* [48,49] proposed a method of detecting turn-to-turn insulation faults (that is, a short formed between two adjacent turns of an electromagnetic coil) using a neural network with input torque and angular speed measurements. Rahimpour *et al.* [50] and Narayana *et al.* [51] used frequency responses to diagnose mechanical damage in transformer coils. Blanquez *et al.* [52] used frequency response analysis to detect inter-turn faults (e.g., turn-to-turn shorts) in electric motors. Rahmatian *et al.* [53] used data analysis and machine learning techniques to detect faults in transformer windings during impulse tests. Heindl *et al.* used frequency responses of transformers to construct a transfer function of the coil [54], and then to construct an equivalent circuit model (ECM) [55], which the authors claimed could be used for fault detection in the coil, though they did not confirm this claim. While these studies deal with fault detection in electromagnetic coils, a method for detecting the degradation of the insulation, which is more desirable since this allows the replacement of the insulation prior to the formation of a harmful turn-to-turn short, was not addressed. Hence, while valuable and similar to the present research, these studies do not add to the foundation established for the research addressed herein.

2.7 Research Gaps

The literature review revealed that most of the available methods for health monitoring of electromagnetic coils are not suitable to detect insulation degradation in systems that use enclosed coils. These coils are inaccessible for traditional insulation tests, which rely on direct contact with the insulation. Further, when used as part of a safety instrumented function (SIF), solenoid valves can remain inactive for long periods of time, either powered on or powered off, depending upon the SIF design. These valves are part of a larger process, which implies that performing functional testing (i.e., powering on/off) can disturb the overall process, and for sensitive processes, this disturbance is generally unwanted. Further, the methods that are developed, such as partial discharge testing, are not useful for low-voltage coil applications, which do not experience electrical discharge events. Hence, impedance measurements could be a useful means to assess the state of insulation health.

Second, there are no experimental analyses concerning the evolution of coil impedance spectrum over the lifetime of electromagnetic coils, showing how the impedance spectrum changes as the insulation transitions from healthy to failed.

Disagreement exists in how the electromagnetic coil capacitance changes when subjected to thermal stress. For example, Lee *et al.* [40] and Younsi *et al.* [41] found that insulation capacitance decreased as the insulation aged, while Werynski *et al.* [36] and Savin *et al.* [42, 43] found that insulation capacitance increased when the insulation was exposed to elevated temperatures. In order to apply impedance-based health monitoring, the relationship between degradation and measured electrical parameters must be established. Further, to help quantify the degradation and correlate degradation with electrical parameters, it is necessary to relate changes in electrical impedance parameters to changes in mechanical and chemical properties.

2.8 Research Objectives

Based upon the identified research gaps, the objectives of this research are as follows. First, it is necessary to develop and demonstrate the capability to use the impedance spectrum to monitor the health of electromagnetic coil insulation over the lifetime of a coil. This method of using impedance as a health indicator is advantageous because a low-voltage signal can be used, which minimizes disturbances to the system, and the insulation in enclosed coils can be assessed without the need for direct contact with the insulation. In Section 1.2, a preliminary experiment showed that impedance measurements correlated with insulation aging, and that these correlations were dependent upon the frequency at which impedance was measured. Hence, it is clear that impedance can be used to assess insulation health, but it necessary to further quantify the specifications on the frequencies to monitor, and to establish the underlying physical changes that prompted the changes in impedance and health. Therefore, a second research objective is to relate the changes in the impedance spectra to changes in the electrical, mechanical, and chemical properties of the insulation. Changes in these properties can be used to provide explanations for the overall evolution of coil impedance, thus relating the physical state of the insulation to the impedance health indicator.

Chapter 3: Insulation Electrical Parameter Sensitivity Analysis

An equivalent circuit model (ECM) is designed to reproduce the electrical behavior of a system, while providing a mathematical model that can be used for analysis [56, 57]. A lumped-parameter ECM of an electromagnetic coil allows for a mathematical and physics-based treatment of the frequency-dependent impedance response. In this chapter, an ECM is used to model a single electromagnetic coil, and then the insulation parameters are used in a sensitivity analysis to understand the effect that changes in these insulation parameters have on the coil impedance spectrum. Then an experiment is presented in which the electrical parameters of the electromagnetic coil insulation are measured in conjunction with the coil impedance, allowing for a comparison to be performed between the expected theoretical changes and the experimental changes.

3.1 Lumped Parameter Equivalent Circuit Model Derivation

Consider the equivalent circuit model for an electrical coil shown in Figure 3.1. This model incorporates bulk parameters for the coil resistance and inductance, as well as the total coil insulation capacitance and insulation resistance. The insulation is modeled as a capacitance, C, in parallel with a resistance, R_i, while the coil inductance is modeled as an inductor, L, and the total coil DC resistance is modeled as a resistor, R_c. A variant of this ECM that did not include the insulation resistance variable was applied by Kryter [2, 3] to model solenoid valve electromagnetic coils (see Figure 2.2), inductors [30–32], and lossy coils [58, 59] (in modeling lossy coils, the insulation capacitance was neglected along with the insulation resistance). The justification for using this ECM rather than that shown in Figure 2.2 or the complex ECM used by Perisse *et al.* shown in Figure 2.4 is two-fold. First, it was important to account for the different electrical behavior characteristics of the electromagnetic coil, and in the proposed model (Figure 3.1), the inductance and resistance of the coil are accounted for, in addition to the capacitance and resistance of the insulation. Second, in contrast with Perisse's ECM, the proposed ECM is simple enough to be examined analytically using sensitivity analysis.

The parameters in the ECM shown in Figure 3.1 are the unit length values integrated over the entire coil. For example, R_c can be computed using the well-know formula: $R_c = \rho L_c / A_c$, where ρ is the resistivity of the conductor material, L_c is the total length of the conductor, and A_c is the cross-sectional area of the conductor. While a more challenging computation, the capacitance and resistance of the insulation can be effectively computed using the total contact surface area,

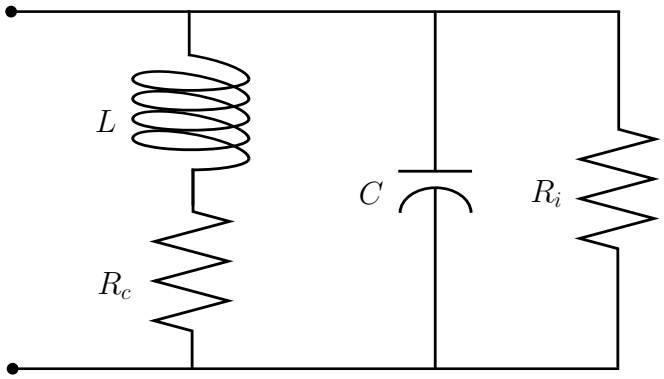

Figure 3.1: Equivalent circuit model of a single electromagnetic coil with lumped parameters

the separation distance, and the dielectric properties of the insulation material. While some researchers have attempted to compute the exact value of the insulation capacitance in an electromagnetic coil [30–32], these computations are beyond the scope of this research. The impedance for this model is given by Eq. 3.1, where $j = \sqrt{-1}$. As with all ECMs, this model is approximate, but it is correct in the limit of DC excitation: $\lim_{R_i \to \infty, \omega \to 0} = R_c$.:

$$\begin{aligned} Z(\omega) &= \left[\frac{1}{j\omega L + R_c} + j\omega C + \frac{1}{R_i} \right]^{-1} \\ &= \frac{R_c R_i + j\omega L R_i}{R_c + R_i + j\omega \left(L + R_c R_i C \right) - \omega^2 R_i C L} \end{aligned} \tag{3.1}$$

Separating the real and imaginary parts, the resistance and reactance are:

$$\mathrm{Re}\left\{ Z(\omega) \right\} = R(\omega) = \frac{R_c^2 R_i + R_c R_i^2 + \omega^2 L^2 R_i}{\omega^2 L^2 + 2 R_c R_i + R_i^2 \left(\omega^2 L C - 1 \right)^2 + R_c^2 \left(\omega^2 C R_i + 1 \right)} \tag{3.2}$$

$$\mathrm{Im}\left\{ Z(\omega) \right\} = X(\omega) = \frac{\omega R_i^2 \left[L - C \left(R_c^2 + \omega^2 L^2 \right) \right]}{\omega^2 L^2 + 2 R_c R_i + R_i^2 \left(\omega^2 L C - 1 \right)^2 + R_c^2 \left(\omega^2 C R_i + 1 \right)} \tag{3.3}$$

Since the resonant frequency defined as $\omega_r \stackrel{\text{def}}{=} \{ \omega : X(\omega) = 0, \omega > 0 \}$, the resonant frequency of the ECM is:

$$\begin{aligned} & \omega R_i^2 \left[L - C \left(R_c^2 + \omega^2 L^2 \right) \right] = 0 \\ & \implies \omega_r = \sqrt{\frac{L - R_c^2 C}{L^2 C}} = \sqrt{\frac{L/C - R_c^2}{L^2}} \end{aligned} \tag{3.4}$$

The analysis of the effect of capacitance performed by Perisse *et al.* [33, 34] does appear to be supported, as an increasing value of capacitance will lead to a lower value of the resonant frequency. However, according to this model, the value of the insulation resistance plays no role in the location of the resonant frequency, implying

that resonant frequency in an incomplete health indicator. The insulation resistance does, however, play a role in the magnitude of impedance at the resonant frequency, and according to the experiments performed by Younsi *et al.* [41], insulation resistance is clearly a health indicator for the magnet wire insulation. Letting $\omega = \omega_r$, the value of resonant impedance is:

$$R\left(\omega = \omega_r\right) = \frac{LR_i}{L + CR_cR_i}$$

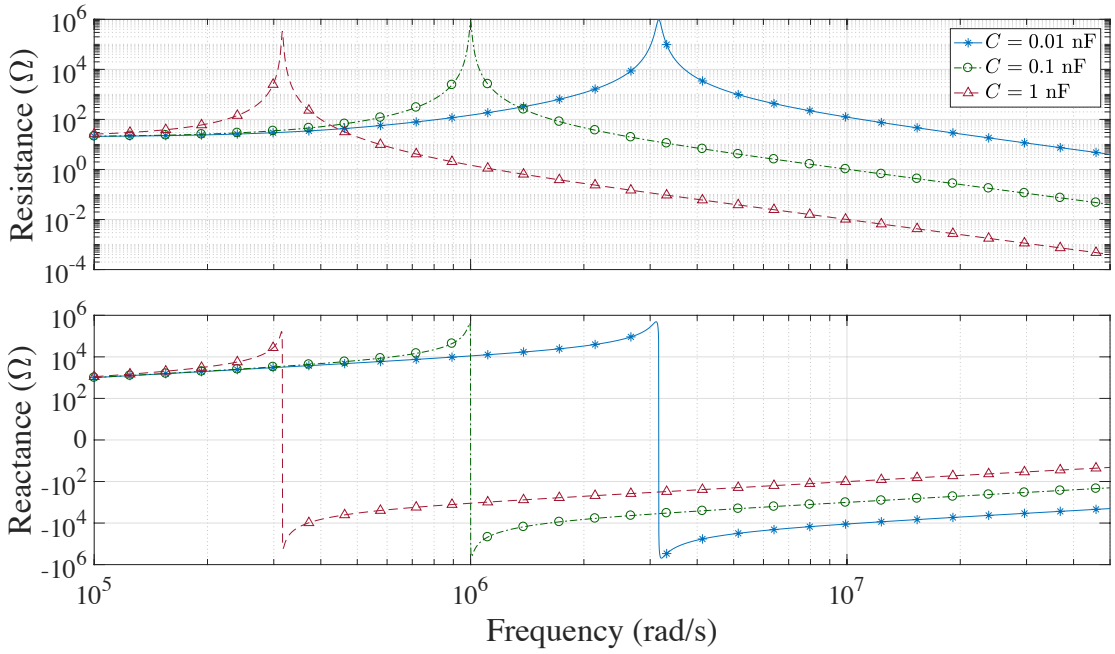

Figure 3.2: ECM resistance (above) and reactance (below) spectra for differing values of insulation capacitance, simulated using 3.2 and 3.3 with $L = 0.01$ H, $R_c = 20\ \Omega$, and $R_i = 1\ \text{M}\Omega$.

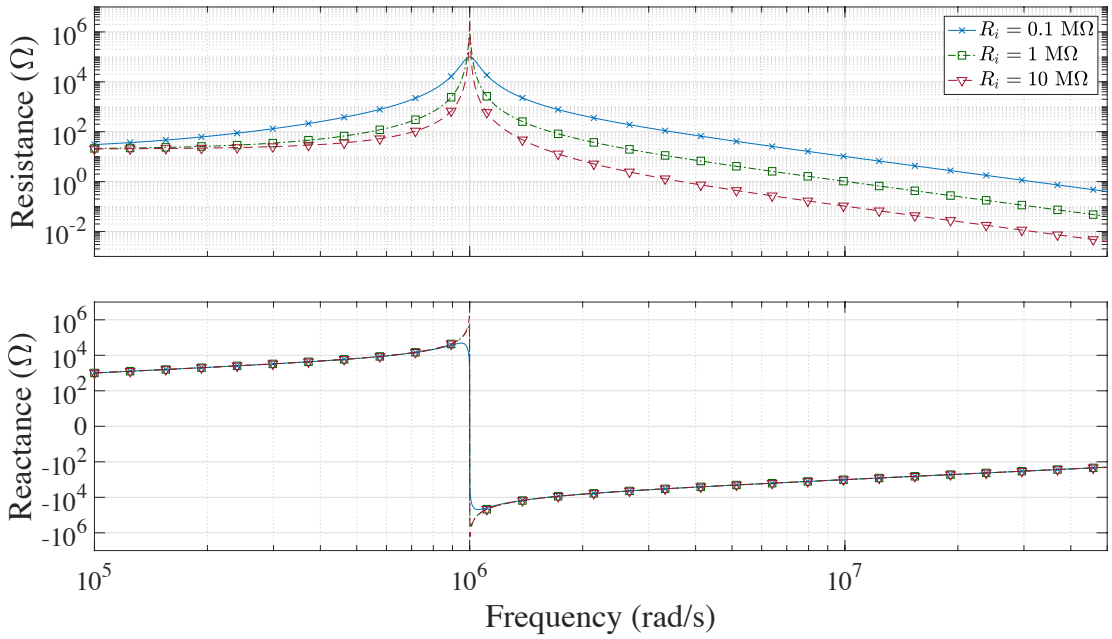

Figure 3.3: ECM resistance (above) and reactance (below) spectra for differing values of insulation capacitance, simulated using Equations 3.2 and 3.3 with $L = 0.01$ H, $R_c = 20\ \Omega$, and $C = 0.1$ nF.

3.2 Model Sensitivity Analysis

Parameter selection is key to effective health monitoring. An important tool in parameter selection is sensitivity analysis, which is used to determine how input variables affect output behavior [60]. The most widely used approach to sensitivity analysis is known as the local approach, where small perturbations around nominal values of the parameters are examined. This consists of calculating or estimating the partial derivatives of the model. For example, given a model $Y = f(\mathbf{X})$, where $\mathbf{X} = \{X_i\}_{i=1}^{n}$ represents the model input variables, the local sensitivity index measuring the effect on Y of perturbing X_j is given in 3.5.

$$S_j = \frac{\partial Y}{\partial X_j} \tag{3.5}$$

Typically, this analysis is performed in a one-at-a-time (OAT) manner [61,62]. This means that inference about the behavior of Y is made by changing one factor, X_j, at a time and investigating the corresponding change in Y.

Since insulation degradation is expected to change the values of insulation capacitance and insulation resistance as a function of the loading conditions [16], we first examine the partial derivatives of resistance and reactance, taken with respect to insulation capacitance and insulation resistance. The partial derivatives resistance

and reactance with respect to insulation capacitance are given in Equations 3.6 and 3.7.

$$\frac{\partial R}{\partial C} = -\frac{2\omega^2 R_i^3 \left(\omega^2 L^2 + R_c R_i + R_c^2\right)\left(C\left(\omega^2 L^2 + R_c^2\right) - L\right)}{\left(\omega^2 L^2 + 2R_c R_i + R_i^2\left(\omega^2 LC - 1\right)^2 + R_c^2\left(\omega^2 R_i^2 C^2 + 1\right)\right)^2} \tag{3.6}$$

$$\begin{aligned}\frac{\partial X}{\partial C} =& \frac{2\omega^3 R_i^4 \left(C\left(\omega^2 L^2 + R_c^2\right) - L\right)^2}{\left(\omega^2 L^2 + 2R_c R_i + R_i^2\left(\omega^2 LC - 1\right)^2 + R_c^2\left(\omega^2 R_i^2 C^2 + 1\right)\right)^2} \\ & - \frac{\omega R_i^2\left(\omega^2 L^2 + R_c^2\right)}{\omega^2 L^2 + 2R_c R_i + R_i^2\left(\omega^2 LC - 1\right)^2 + R_c^2\left(\omega^2 R_i^2 C^2 + 1\right)}\end{aligned} \tag{3.7}$$

These computed sensitivity coefficients are shown as a function of frequency in Figure 3.4. For each plot in Figure 3.4, the inductance and coil resistance were held constant at $L = 0.01$ H and $R_c = 20\ \Omega$. In Figure 3.4(a) and 3.4(b), the value of the partial derivative of $R(\omega)$ with respect to insulation capacitance, C, is shown over a range of frequencies. In Figure 3.4(c) and Figure 3.4(d), the partial derivative of $X(\omega)$ with respect to C is shown over a range of frequencies.

Figure 3.4(a) shows $\partial R/\partial C$ at three values of insulation capacitance (0.01 nF, 0.1 nF, and 1 nF) while holding insulation resistance constant at $R_i = 1$ MΩ. Figure 3.4(b) shows $\partial R/\partial C$ at three values of insulation resistance (0.1 MΩ, 1 MΩ, and 10 MΩ) while holding insulation capacitance constant at $C = 0.1$ nF. The resonant frequency is the frequency where $\partial R/\partial C$ crosses 0, and where $\partial X/\partial C$ is at its minimum value. At frequencies below resonance, $\partial R/\partial C$ is positive, while at frequencies above resonance, $\partial R/\partial C$ is negative. This implies that at frequencies below resonance, resistance, $R(\omega)$, changes in the same direction as insulation capacitance, C. At frequencies above resonance, however, $R(\omega)$ changes in the opposite direction on insulation capacitance. The maximum and minimum of $\partial R/\partial C$ (i.e., the frequencies at which $R(\omega)$ is most sensitive to changes in C in positive and negative directions, respectively) are within ±2% of the resonant frequency.

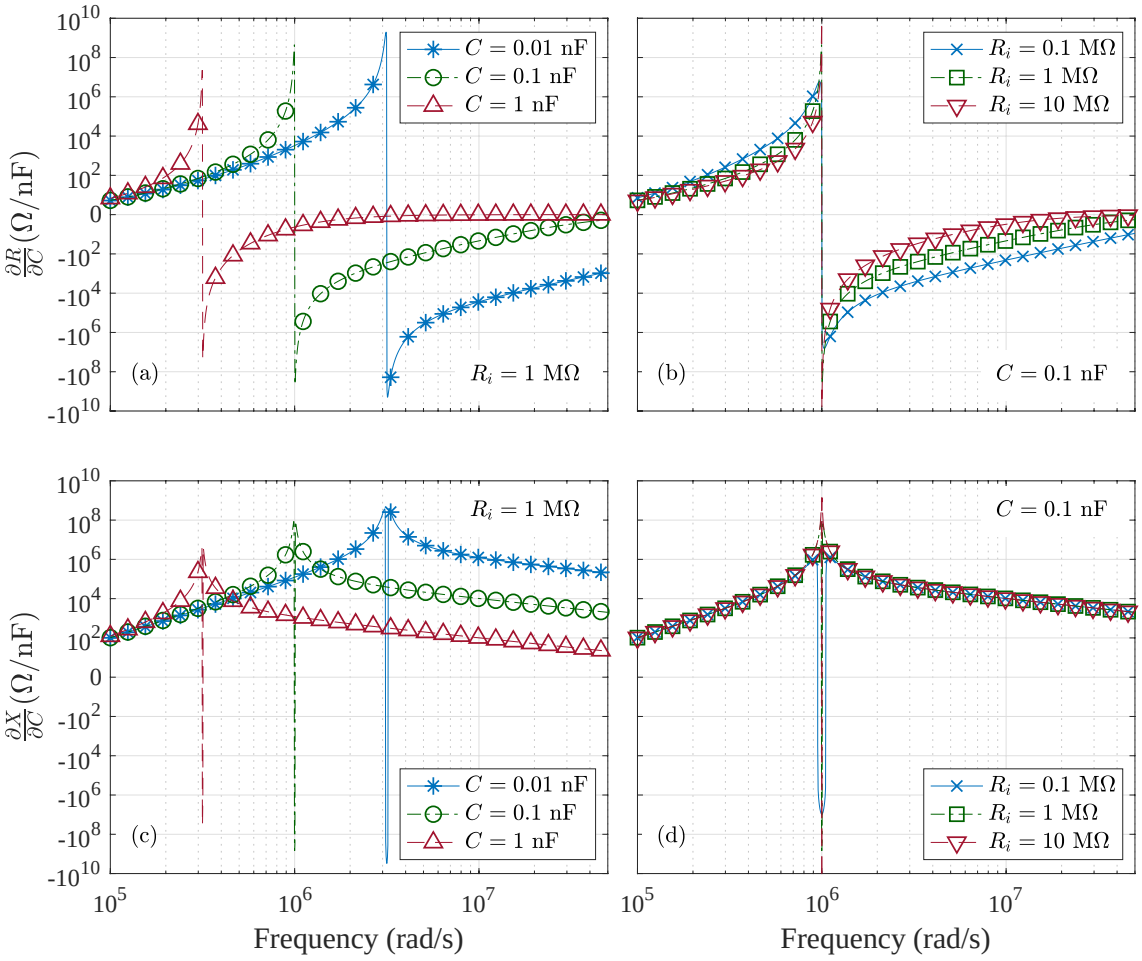

Figure 3.4: Sensitivity coefficients for resistance and reactance with respect to insulation capacitance, having $L = 0.01$ H and $R_c = 20$ Ω. (a) and (b) show the sensitivity coefficient for resistance to insulation capacitance over the frequency spectrum for different values of insulation capacitance and insulation resistance. (c) and (d) show the sensitivity coefficient for reactance to insulation capacitance for different values of insulation capacitance and insulation resistance.

Figure 3.4(c) shows $\partial X/\partial C$ at three values of insulation capacitance (0.01 nF, 0.1 nF, and 1 nF) while holding insulation resistance constant at $R_i = 1$ MΩ. Figure 3.4(d) shows $\partial X/\partial C$ at three values of insulation resistance (0.1 MΩ, 1 MΩ, and 10 MΩ) while holding insulation capacitance constant at $C = 0.1$ nF. At most frequencies above and below resonance, $\partial X/\partial C$ is positive, implying that at these frequencies, reactance, $X(\omega)$, changes in the same direction as insulation capacitance. At a small range of frequencies around resonance, $X(\omega)$ changes in the opposite direction as insulation capacitance. At resonance, the value of $\partial X/\partial C$ is expressed as:

$$\left.\frac{\partial X}{\partial C}\right|_{\omega=\omega_r} = -\frac{L^2 R_i^2}{(L + R_c R_i C)^2}\sqrt{\frac{L/C - R_c^2}{L^2}} \tag{3.8}$$

Hence, the derivative of reactance with respect to insulation capacitance, when evaluated at resonant frequency, is negative and inversely related to the value of insulation resistance (i.e., as insulation resistance increases, $\left.\frac{\partial X}{\partial C}\right|_{\omega=\omega_r}$ becomes more negative, eventually converging, $\lim_{R_i\to\infty} \left.\frac{\partial X}{\partial C}\right|_{\omega=\omega_r} = -L^2/(R_c C)^2)$, but directly related to the value of insulation capacitance (i.e., as insulation capacitance increases, $\left.\frac{\partial X}{\partial C}\right|_{\omega=\omega_r}$ becomes less negative such that $\lim_{C\to\infty} \left.\frac{\partial X}{\partial C}\right|_{\omega=\omega_r} = 0$). The value of $\left.\frac{\partial X}{\partial C}\right|_{\omega=\omega_r}$ for the values of C and R_i used in Figure 3.4 is provided in Table 3.1.

Table 3.1: Values of $\left.\frac{\partial X}{\partial C}\right|_{\omega=\omega_r}$ measured in (Ω/nF) for various values of insulation capacitance and insulation resistance.

		Insulation capacitance		
		0.01 nF	0.1 nF	1 nF
Insulation resistance	0.1 MΩ	$-3.15\,(10^7)$	$-9.61\,(10^6)$	$-2.20\,(10^6)$
	1 MΩ	$-3.04\,(10^9)$	$-6.94\,(10^8)$	$-3.51\,(10^7)$
	10 MΩ	$-2.20\,(10^{11})$	$-1.11\,(10^{10})$	$-7.17\,(10^7)$

The plots in Figure 3.4 provide insight into how the sensitivities of resistance and reactance to changes in insulation capacitance are affected by changes in the insulation parameters. As the value of insulation capacitance decreases, the sensitivity of resistance and reactance to further changes in insulation capacitance decreases. However, decreasing the value of insulation resistance causes $\partial R/\partial C$ to increase at most frequencies, except at a small range of frequencies around, but not equal to, resonance. For reactance, decreasing the value of insulation resistance causes $\partial X/\partial C$ tp decrease at all frequencies, but the decrease is most pronounced at frequencies just below and above resonance.

Next, the sensitivity of the ECM to the insulation resistance parameter, R_i, is examined. The sensitivity coefficients are the frequency-dependent partial derivatives of resistance, $R(\omega)$, and reactance, $X(\omega)$, with respect to insulation resistance, R_i. The partial derivatives of resistance and reactance with respect to insulation resistance are given in Equations 3.9 and 3.10.

$$\frac{\partial R}{\partial R_i} = -\frac{2R_i\left(\omega^2L^2+R_cR_i+R_c^2\right)\left(\omega^2R_c^2R_iC^2+R_c+R_i\left(\omega^2LC-1\right)^2\right)}{\left(\omega^2L^2+2R_cR_i+R_i^2\left(\omega^2LC-1\right)^2+R_c^2\left(\omega^2R_i^2C^2+1\right)\right)^2} + \frac{\omega^2L^2+R_cR_i+R_c^2}{\omega^2L^2+2R_cR_i+R_i^2\left(\omega^2LC-1\right)^2+R_c^2\left(\omega^2R_i^2C^2+1\right)} \tag{3.9}$$

$$\frac{\partial X}{\partial R_i} = \frac{2\omega R_i\left(\omega^2L^2+R_cR_i+R_c^2\right)\left(L-C\left(\omega^2L^2+R_c^2\right)\right)}{\left(\omega^2L^2+2R_cR_i+R_i^2\left(\omega^2LC-1\right)^2+R_c^2\left(\omega^2R_i^2C^2+1\right)\right)^2} \tag{3.10}$$

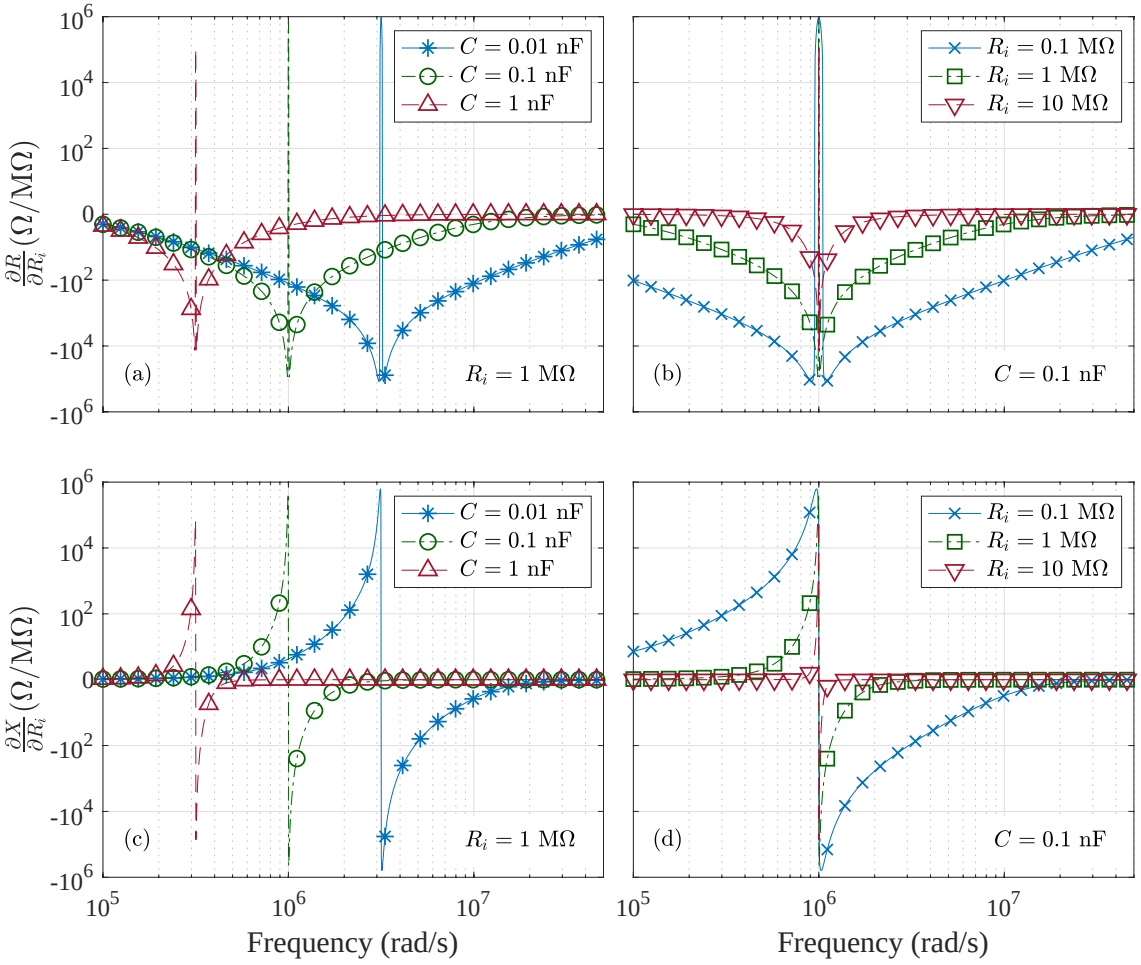

Figure 3.5: Sensitivity coefficients for resistance and reactance with respect to insulation resistance, having $L = 0.01$ H and $R_c = 20\ \Omega$. (a) and (b) show the sensitivity coefficient for resistance to insulation resistance over the frequency spectrum for different values of insulation capacitance and insulation resistance. (c) and (d) show the sensitivity coefficient for reactance to insulation resistance for different values of insulation capacitance and insulation resistance.

These computed sensitivity coefficients are plotted in Figure 3.5. Figure 3.5(a) shows $\partial R/\partial R_i$ for three values of insulation capacitance (0.01 nF, 0.1 nF, and 1 nF) while holding insulation resistance constant at $R_i = 1$ MΩ. Figure 3.5(b) shows $\partial R/\partial R_i$ for three values of insulation resistance (0.1 MΩ, 1 MΩ, and 10 MΩ) while holding insulation capacitance constant at $C = 0.1$ nF. Figure 3.5(c) shows $\partial X/\partial R_i$ for three values of insulation capacitance while holding insulation resistance constant at $R_i = 1$ MΩ. Figure 3.5(d) shows $\partial X/\partial R_i$ at three values of insulation resistance while holding insulation capacitance constant at $C = 0.1$ nF.

The $\partial R/\partial R_i$ curves shown in Figure 3.5 show that at most frequencies above and below resonance, the sensitivity coefficient is negative, implying that for most frequencies in the spectrum, $R(\omega)$ will increase if R_i decreases, and vice versa. However, for a small range of frequencies around and including resonance, $\partial R/\partial R_i$ is positive, implying that at these frequencies, $R(\omega)$ will decrease if R_i decreases and vice versa. This is confirmed in Figure 3.3, where increasing values of R_i caused $R(\omega)$ to decrease, except around resonance where increasing R_i caused increased $R(\omega)$. The value of $\partial R/\partial R_i$ at resonance is given by Equation 3.11.

$$\left.\frac{\partial R}{\partial R_i}\right|_{\omega=\omega_r} = \frac{L^2}{(L + R_c R_i C)^2} \tag{3.11}$$

In this case, the value of $\partial R/\partial R_i$ at resonant frequency is inversely related to both insulation resistance and insulation capacitance. The value of $\left.\frac{\partial R}{\partial R_i}\right|_{\omega=\omega_r}$ for the values of C and R_i used in Figure 3.5 is provided in Table 3.2.

Table 3.2: Values of $\left.\frac{\partial R}{\partial R_i}\right|_{\omega=\omega_r}$ measured in (Ω/MΩ) for various values of insulation capacitance and insulation resistance.

		Insulation capacitance		
		0.01 nF	0.1 nF	1 nF
Insulation resistance	0.1 MΩ	$9.96\,(10^5)$	$9.61\,(10^5)$	$6.94\,(10^5)$
	1 MΩ	$9.61\,(10^5)$	$6.94\,(10^5)$	$1.11\,(10^5)$
	10 MΩ	$6.94\,(10^5)$	$1.11\,(10^5)$	$2.27\,(10^3)$

Figure 3.5(c) and Figure 3.5(d) show that the sensitivity coefficient of reactance with respect to insulation resistance is positive at frequencies below resonance and negative at frequencies above resonance, but at resonance, the value of the sensitivity coefficient is zero. Hence, at frequencies below resonance, $X(\omega)$ will change in the same direction as R_i, but at frequencies above resonance, $X(\omega)$ will change in the opposite direction as R_i.

The plots in Figure 3.5 indicate that the sensitivities of resistance and reactance change as the values of insulation resistance and insulation capacitance change. As the value of insulation resistance increases, the sensitivity coefficients decrease.

Similarly, as the value of insulation capacitance increases, the sensitivity coefficients decrease.

Previous studies proposed that resonant frequency be used as a health indicator. Earlier in this chapter, it was shown that according to the developed ECM, changes in insulation resistance are not reflected in resonant frequency measurements (see Equation 3.4). However, even as a health indicator that reflects changes in insulation capacitance, resonant frequency sensitivity coefficients are often lower in magnitude than those of impedance measurements around resonance. To show this, consider the sensitivity coefficient for the resonant frequency with respect to insulation capacitance in Equation 3.12.

$$\frac{\partial \omega_r}{\partial C} = -\frac{1}{2}\sqrt{\frac{1}{C^3\left(L - CR_c^2\right)}} \tag{3.12}$$

The resonant frequency sensitivity coefficient, $\partial\omega_r/\partial C$, is plotted against insulation capacitance in Figure 3.5, which should be compared to the plots of $\partial R/\partial C$ and $\partial X/\partial C$ in Figure 3.4. At every frequency shown, the maximum sensitivity coefficients for resistance and reactance are between one and four hundred times larger than $\partial\omega_r/\partial C$. this implies that the resistance and reactance measurements at these frequencies are generally more sensitive to changes in the insulation capacitance than measurements of resonant frequency.

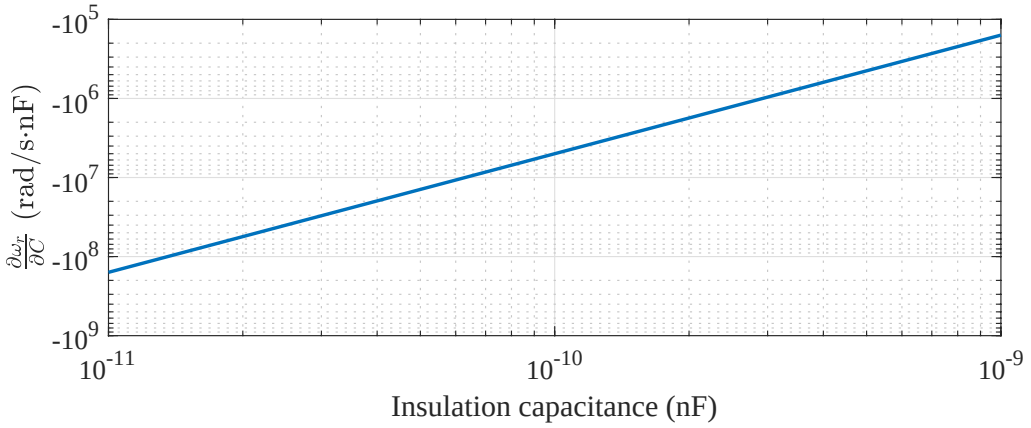

Figure 3.6: Sensitivity coefficient of resonant frequency to insulation capacitance simulated using 3.12 with $L = 0.01$ H and $R_c = 20\ \Omega$.

Based on Figures 3.4, 3.5, and 3.6, the regions to look for insulation health information in the frequency spectrum of an electromagnetic coil are slightly below and above resonance. In the simulations shown in this paper, the maximum and minimum of the sensitivity curves are within $\pm 2\%$ of the resonant frequency. However, the maximum and minimum of each curve move relative to the resonance based upon the value of the model parameters (i.e., for a higher insulation capacitance, the resonant frequency decreases and the range enclosed by the maximum and minimum of the sensitivity curve increases). At frequencies around, but not exactly

equal to, resonance, resistance and reactance show the greatest sensitivity with respect to insulation resistance and capacitance. This sensitivity analysis shows that measurement of a strategically chosen range of frequencies is more responsive to changes in the insulation parameters than monitoring only the resonant frequency, demonstrating both the effectiveness of impedance measurements for health monitoring purposes and the necessity of monitoring the impedance at carefully selected frequencies. This is advantageous since measurement of electromagnetic coil resonant frequency requires high resolution in the measurement frequencies, whereas measurements at a range of frequencies around resonance can provide more sensitive information but do not require the same resolution of frequencies. A summary of the analysis results is presented in Table 3.3.

Table 3.3: Summary of sensitivity analysis

Parameter	Below resonance	At resonance	Above resonance
Resistance, $R(\omega)$	Positive	$\frac{LR_i}{L+R_cR_iC}$	Positive
Reactance, $X(\omega)$	Positive	0 (by definition)	Negative
$\partial R/\partial C$	Positive (maximum slightly below resonance)	0	Negative (minimum slightly above resonance)
$\partial R/\partial R_i$	Negative (minimum slightly below resonance)	$\frac{L^2}{(L+R_cR_iC)^2}$	Negative (minimum slightly above resonance)
$\partial X/\partial C$	Positive (maximum slightly below resonance)	$-\frac{L^2R_i^2}{(L+R_cR_iC)^2}\sqrt{\frac{L/C-R_c^2}{L^2}}$	Positive (maximum slightly above resonance)
$\partial X/\partial R_i$	Positive (maximum slightly below resonance)	0	Negative (minimum slightly above resonance)

3.3 Preliminary Experiment Revisited

In the Section 1.2, an experiment was introduced in which a generic solenoid-operated valve was aged in a 80 °C/50 %RH environment. With the sensitivity analysis in mind, this data can be further analyzed. First, the equivalent circuit model from Figure 3.1 is fit to the healthy data to predict where in the impedance spectrum we should expect to see the greatest sensitivities to changes in the insulation electrical parameters. With a nonlinear least-squares algorithm, a transfer function model was fit to the resistance and reactance data, yielding electrical parameters, $L = 5.75$ mH, $R_c = 10.36\ \Omega$, $C = 70.41$ pF, and $R_i = 22.99$ kΩ (this value of insulation resistance attempts to capture all parallel electrical paths through the insulation integrated over the entire coil, including all layer-to-layer and turn-to-turn

interactions over about 34 layers with about 62 turns per layer). The theoretical sensitivity coefficients for resistance and reactance are shown in Figure 3.7.

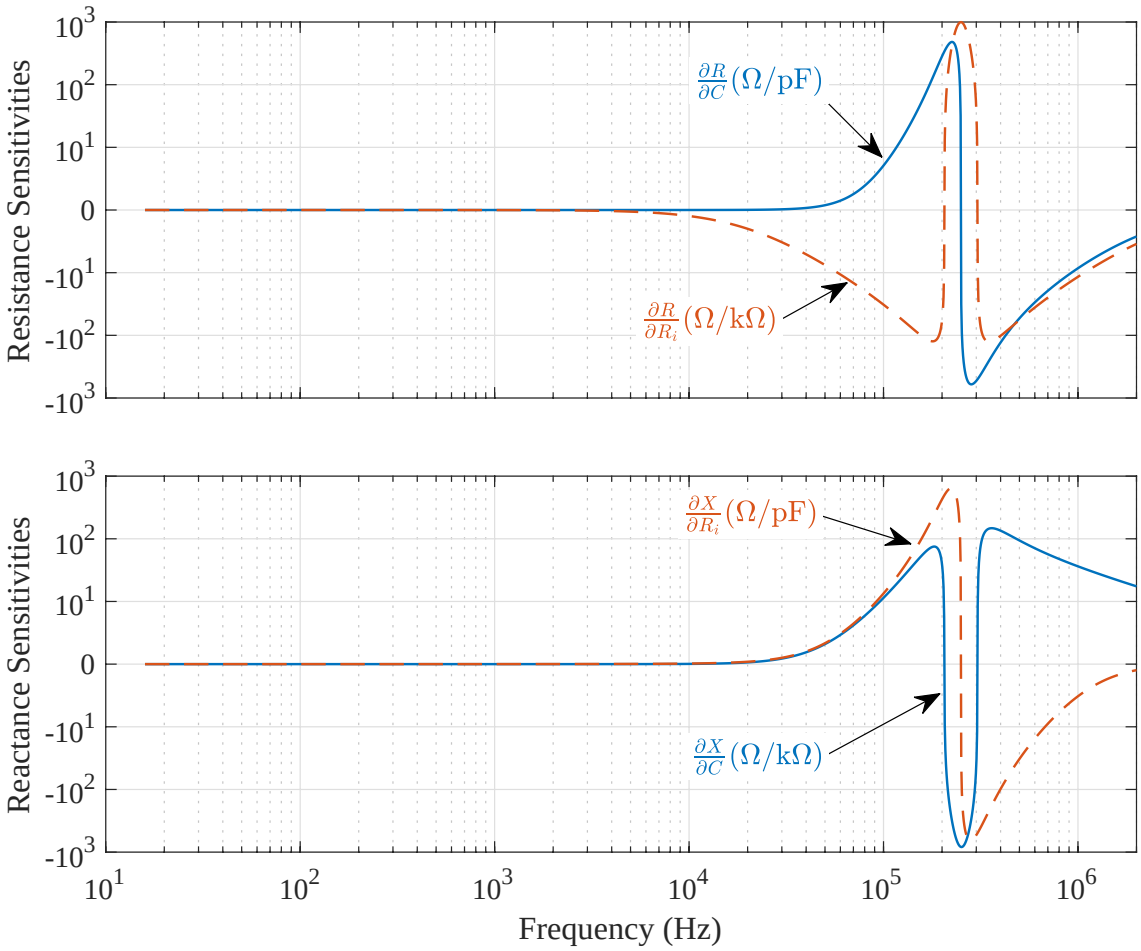

Figure 3.7: Computed sensitivity coefficients for the generic SOV used in the preliminary experiment (see Section 1.2). The sensitivity coefficients were computed using the parameter values fit to the ECM in FIgure 3.1 using a nonlinear least squares algorithm.

Once again, the Spearman correlation spectrum can be computed for the degradation data. However, to understand the amount of change that each time series underwent, a linear model was fit to each time series and the slope of the line is used to modify the size of each data point in the Spearman correlation spectrum. Hence, as indicated in Figure 3.8, the size of each data point is proportional to the absolute value of the slope of a linear model fit to the corresponding time series. The Spearman correlation spectra in Figure 3.8 confirms the ECM sensitivity analysis in that time series at frequencies around resonance have the highest linear slopes, indicating that they changed to a greater degree than the time series at other frequencies. Previous studies on the degradation of polyethylene (identified as the insulation material in the SOV electromagnetic coil) [63–65] showed that when sub-

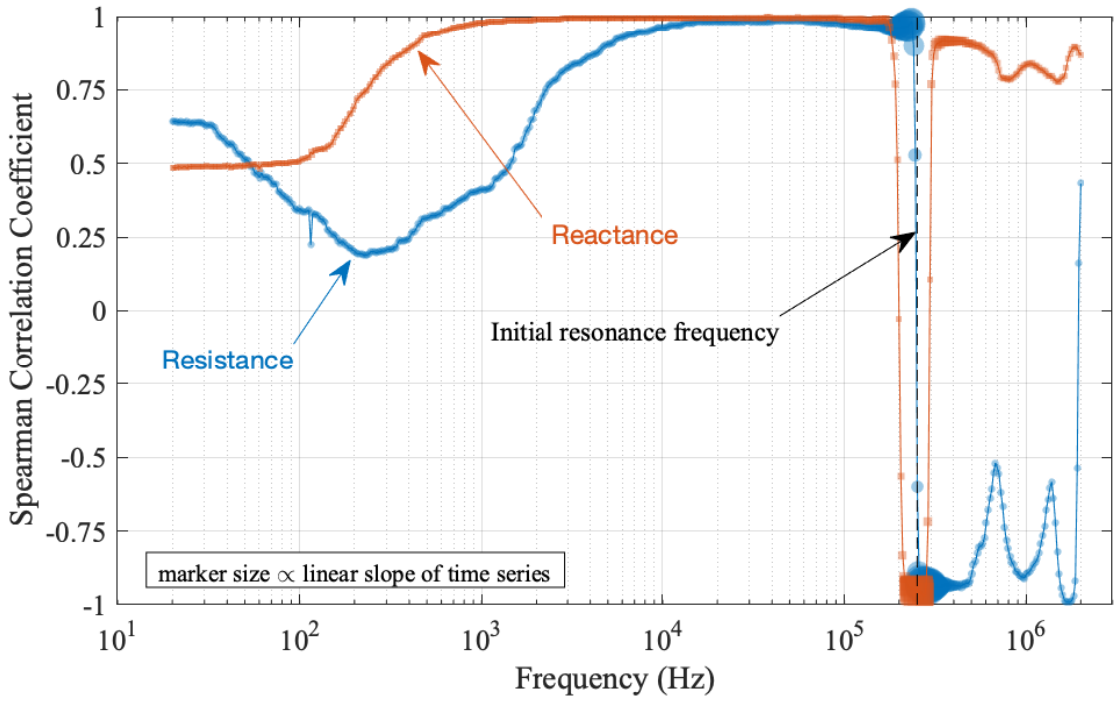

Figure 3.8: Spearman correlation coefficient spectrum for 80 °C/50 %RH aging (using data prior to formation of coil short). The movement of the resonant frequency is not shown since the resonant frequency only decreased by about 2.5% prior to insulation failure. The size of each data point marker is directly related to the slope of the linear fit of the time series at that particular frequency.

jected to thermal and/or oxidative degradation, the relative permittivity (directly related to the capacitance) increased, while the resistance of the polyethylene decreased. The observation that the solenoid valve coil resonant frequency decreased prior to the formation of a short supports the finding that capacitance increased over the aging period.

According to the ECM analysis, and assuming the results of the previous experiments on polyethylene are applicable, resistance should increase at frequencies below resonance, while at frequencies above resonance, the changes in capacitance and insulation resistance are expected to drive resistance in opposite directions (increasing capacitance should cause the resistance to decrease, while decreasing insulation resistance should cause resistance to increase). The influence of increasing insulation capacitance and decreasing insulation resistance are compounded at frequencies just above and below resonance and at resonance.

The converse is true for reactance: at frequencies below resonance, the changes in insulation capacitance and insulation resistance are expected to drive the reactance in opposite directions (increasing capacitance should cause the reactance to increase, while decreasing insulation resistance should cause reactance to decrease), while at frequencies above resonance, reactance should increase. The experimental

results show reactance is negatively correlated with the aging time at frequencies around resonance (between 204.7 kHz and 289.1 kHz). This frequency range is wider than predicted in the ECM analysis shown in Figure 3.7, although decreasing insulation resistance could contribute to the decreasing reactance at frequencies below resonance. As expected from the ECM sensitivity analysis, the highest slopes occur at the frequencies around, but not exactly equal to, resonance.

For the theoretical SOV ECM sensitivity analysis shown in Figure 3.7, the sensitivity to changes in insulation capacitance are approximately equal to the sensitivity to changes in insulation resistance. Experimentally, changes in capacitance generally appear to dominate at frequencies farther away from resonant frequency, as the Spearman correlation spectra for resistance and reactance match well with predictions shown in Figure 3.7, given increasing insulation capacitance. However, around resonance, the influence of decreasing insulation resistance can be seen. The resistance data show large negative slopes around resonance, where it is highly sensitive to changes in insulation resistance. Reactance data begins to decrease at frequencies lower than predicted from the $\partial X/\partial C$ curve shown in Figure 3.7, likely due to decreasing insulation resistance.

As mentioned in Section 1.2, the valve coil showed a 2.5% decrease in resonant frequency prior to the formation of a short, while at 276.1 kHz, reactance decreased by over 25%, and at 240.4 kHz, resistance increased by over 14% during the same time period. This highlights the advantages of the method developed herein over the method developed in [34]. Given that the electrical parameters of the insulation change during degradation, examining frequencies around resonance, rather than at resonant frequency, yields more sensitive health indicators and is experimentally more practical.

3.4 Double Wound Coil Experiment

A more comprehensive experiment and analysis is presented in this section. This experiment and the experimental objects are referenced throughout the remainder of the paper in examining the electrical, mechanical, and chemical characteristics of degraded insulation.

3.4.1 Experimental Setup

Four dual-wound electromagnetic coils were manufactured by Magnecomp, Inc., a coil manufacturing company located in South Carolina, USA. The dual-wound coils were constructed by winding two piece of magnet wire around the same bobbin, leaving the insulation as the dielectric between the two coils (see Figure 3.9(a)). The parallel magnet wires were wound on a rectangular Pyroglass bobbin. An example of this winding arrangement (though not a replica of the arrangement of the experimental coils) is illustrated in Figure 3.9(b), where the base numbers indicate the turn number and the superscript numbers indicate the two parallel windings of magnet wire. Each winding had 220 turns of AWG 26 (conductor

diameter of 361 ± 3 µm) with heavy Allex® polyimide (an aromatic polyimide rated for 240 °C [66]) insulation (thickness of 25.25 ± 3.75 µm). Each winding had a DC resistance of about 1.9 Ω at 25 °C.

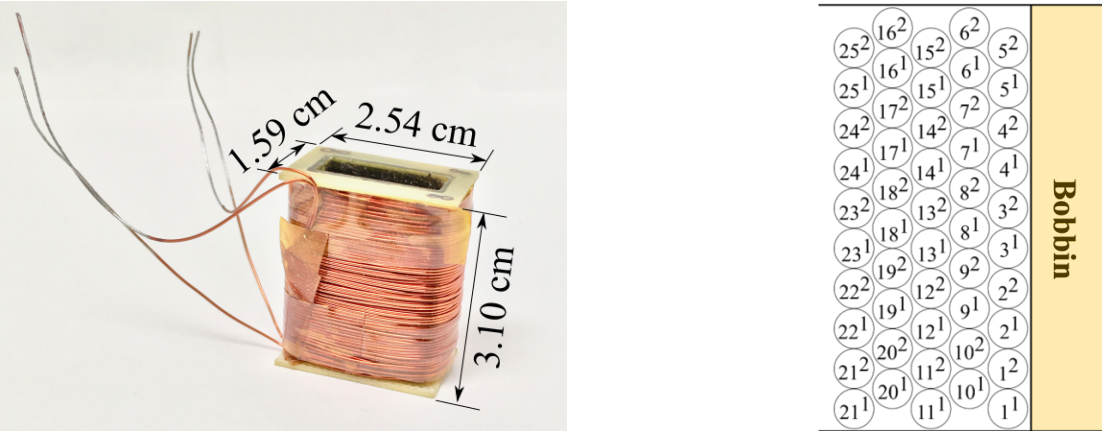

(a) Received unit

(b) Winding arrangement schematic

Figure 3.9: Magnecomp dual-wound coil construction.

To age the insulation in a manner that would likely occur in fielded application conditions, one of the parallel windings was powered to produce an average internal temperature of 200 °C. The average internal coil temperature was determined using the temperature-resistance relationship as shown in Equation 3.13, where $\alpha = 0.0039/°\text{C}$ is the temperature coefficient of resistance for copper, and R_0 is the reference resistance at temperature, T_0. The final average temperature of the coil is given by $T(R_T)$ and the final resistance is given by R_T. The required voltage was between 6.7 and 7.1 V, and after transients settled, the current was between 1.95 and 2.05 A.

$$T(R_T) = \frac{1}{\alpha}\left(\frac{R_T}{R_0} + \alpha T_0 - 1\right) \tag{3.13}$$

Each time the coils were removed from power, three measurements were performed. First, the terminal impedance of the windings was measured using an Agilent E4980A LCR meter at 501 distinct frequencies over the frequency range $f \in [20, 2\,(10^6)]$ Hz with a 500 mV RMS (root mean square) signal. Second, the impedance of the insulation was measured using an Agilent E4980A LCR meter at 201 distinct frequencies in the frequency range $f \in [20, 2\,(10^6)]$ Hz with a 1 V RMS signal. This measurement was performed by shorting the terminals of each winding as illustrated in Figure 3.10, which allowed the electric field to be directed through the insulation only. In this illustration, the terminals of each winding are connected, and a voltage is applied across the insulation separating the windings. Third, the response of the insulation to a step application of 100 VDC was measured, allowing

for measurement of DC resistance characteristics of the insulation. This measurement was performed with the coil windings in the same setup as for the insulation impedance (Figure 3.10). For this measurement, 100 VDC was placed across the insulation and held for 20 minutes, while the current was sampled once per second.

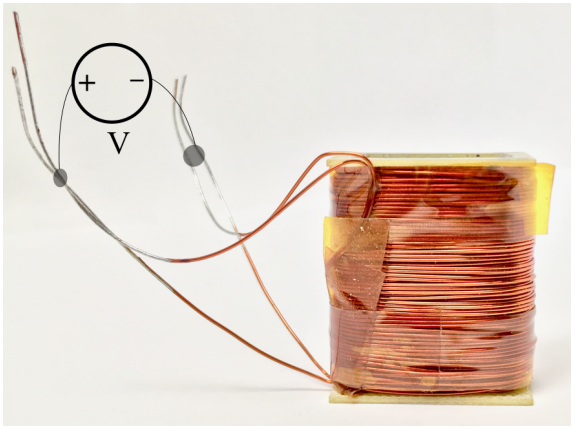

Figure 3.10: Setup for measurement of dual-wound coil insulation electrical parameters (i.e., insulation impedance and insulation resistance).

3.4.2 Experimental Results

The insulation impedance was measured at 201 distinct frequencies, equally spaced on the base-10 logarithmic scale. Insulation impedance measurements were first split into real and imaginary parts. The results for one coil (referenced as "Coil 1" for the remainder of this report) over an entire aging experiment is shown in Figure 3.11. Both resistance ($\mathrm{Re}\{Z(\omega)\}$) and reactance ($\mathrm{Im}\{Z(\omega)\}$) increased over the course of aging.

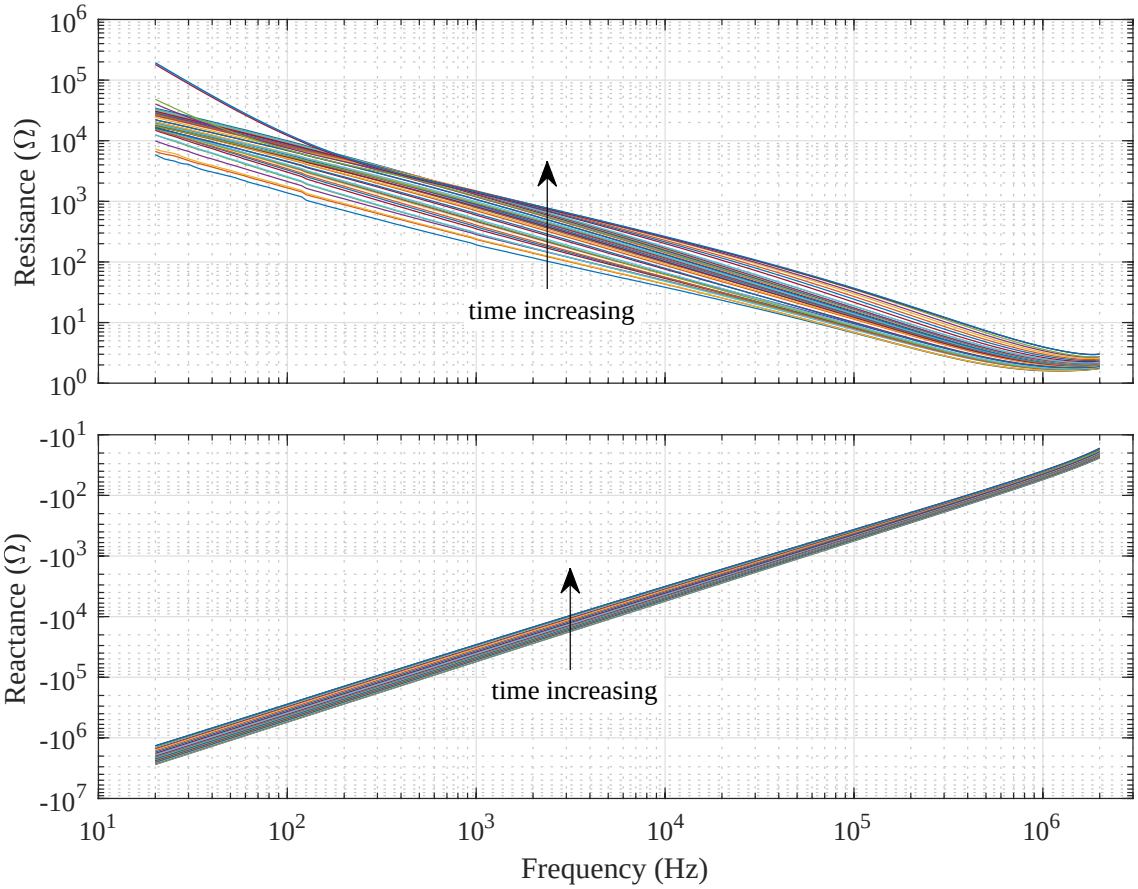

Figure 3.11: Insulation impedance of "Coil 1" as the dual-wound coil was aged at an average internal temperature of 200 °C

Insulation capacitance can be computed from reactance by fitting a model to the reactance and removing the inductive portion of reactance. Recall that reactance is expressed as a function of frequency in rad/s as $X(\omega) = \omega L - (\omega C)^{-1}$, or equivalently as a function of frequency in Hz as $X(f) = 2\pi f L - (2\pi f C)^{-1}$. Hence, by fitting a model of the form $\hat{X}(f) = af - bf^{-1}$, where $a = 2\pi L$ and $b = (2\pi C)^{-1}$ are weighting coefficients, the insulation reactance measurements can be evaluated for the amount of inductive reactance and capacitive reactance comprising the measurements. The result of fitting for the first Coil 1 insulation reactance measurement is shown in Figure 3.12. This model is an excellent fit with a coefficient of determination value of $R^2 = 1.0$. There is some slight divergence between the model and the data at frequencies between about 1 MHz and 2 MHz.

In order to compute the insulation capacitance, the reactance measurements can be adjusted using the model fit, i.e., $X_C = -(2\pi f C)^{-1} = X(f) - af$. It is assumed that the inductive portion of reactance will not change over the course of aging, so the initial model fit is sufficient to be used to adjust all the insulation reactance measurements. The adjusted capacitance spectra over the aging period for Coil 1 are shown in Figure 3.13, and the capacitance at 100 kHz for all the coil

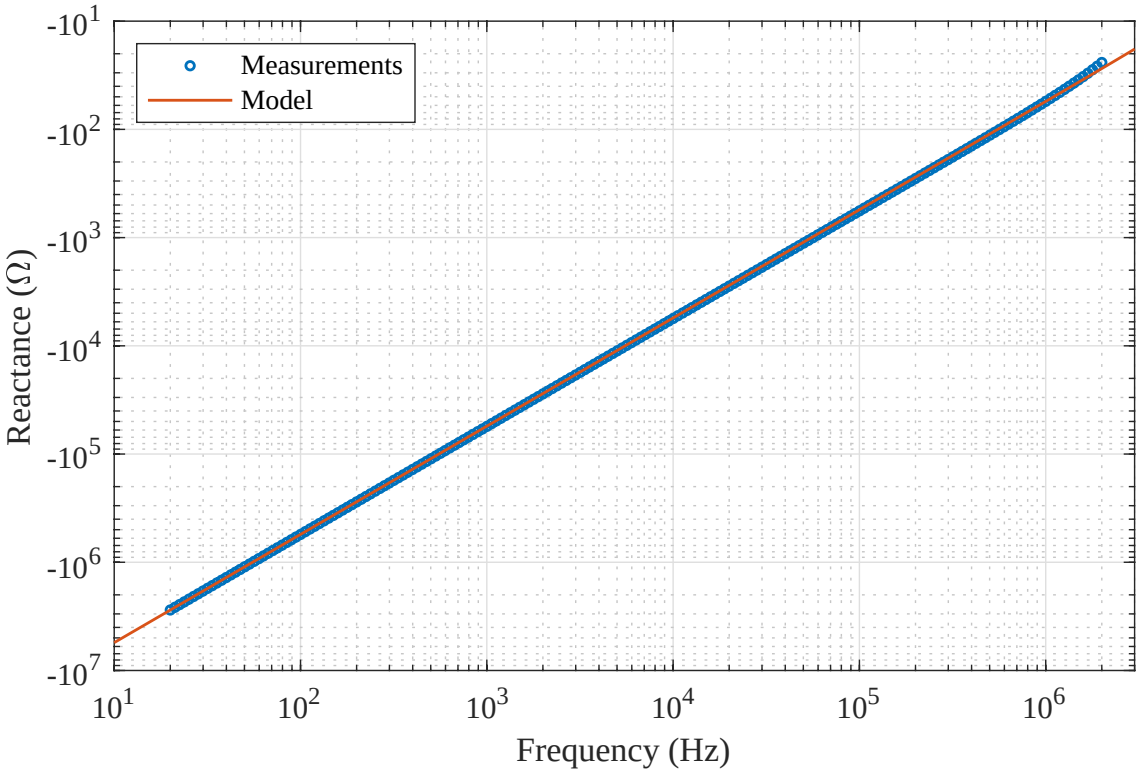

Figure 3.12: Insulation reactance and model fit for the first insulation reactance measurement of Coil 1. The fit model is $\hat{X}(f) = 1.042\,(10^{-7})\,f - 5.525\,(10^{7})\,f^{-1}$. The model has a coefficient of determination value of $\mathrm{R}^2 = 1.0$.

samples, and their respective percent's change, is shown in Figure 3.14.

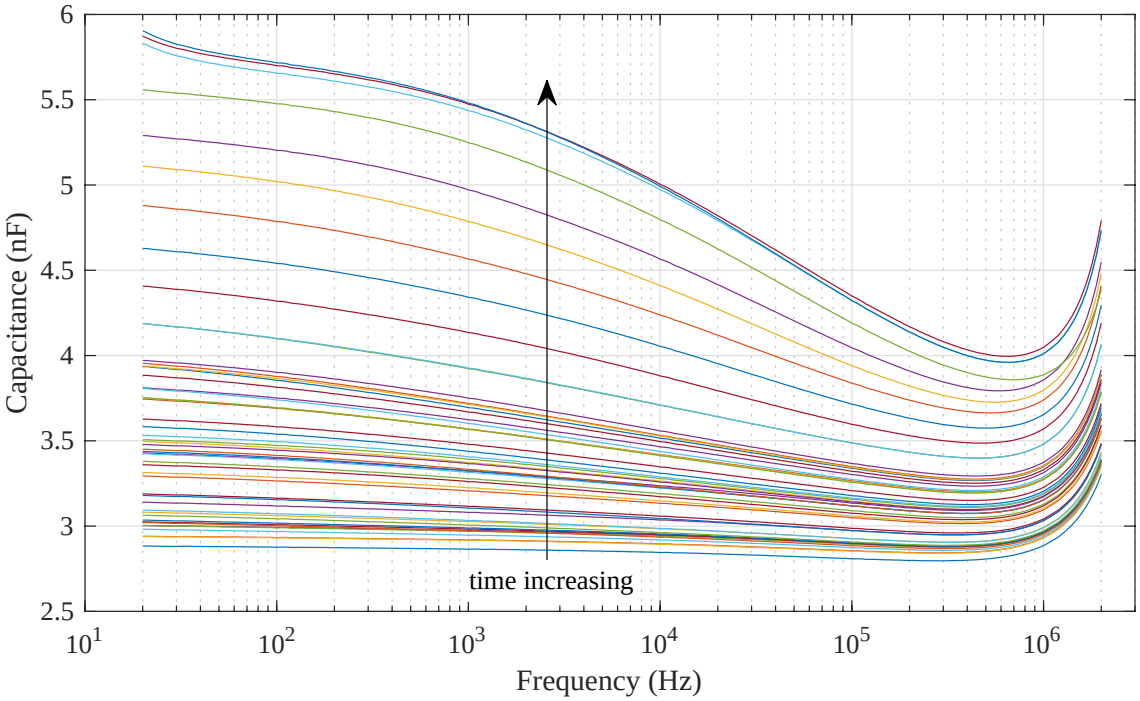

Figure 3.13: Insulation capacitance for Coil 1 as the coil thermo-mechanically aged, calculated by converting reactance to capacitance, $C = \frac{1}{2\pi f\left(1.042\left(10^{-7}\right) f - X\left(f\right)\right)}$. The "time increasing" arrow is meant to denote the direction of movement for the spectra as the insulation aged for over 4000 hours.

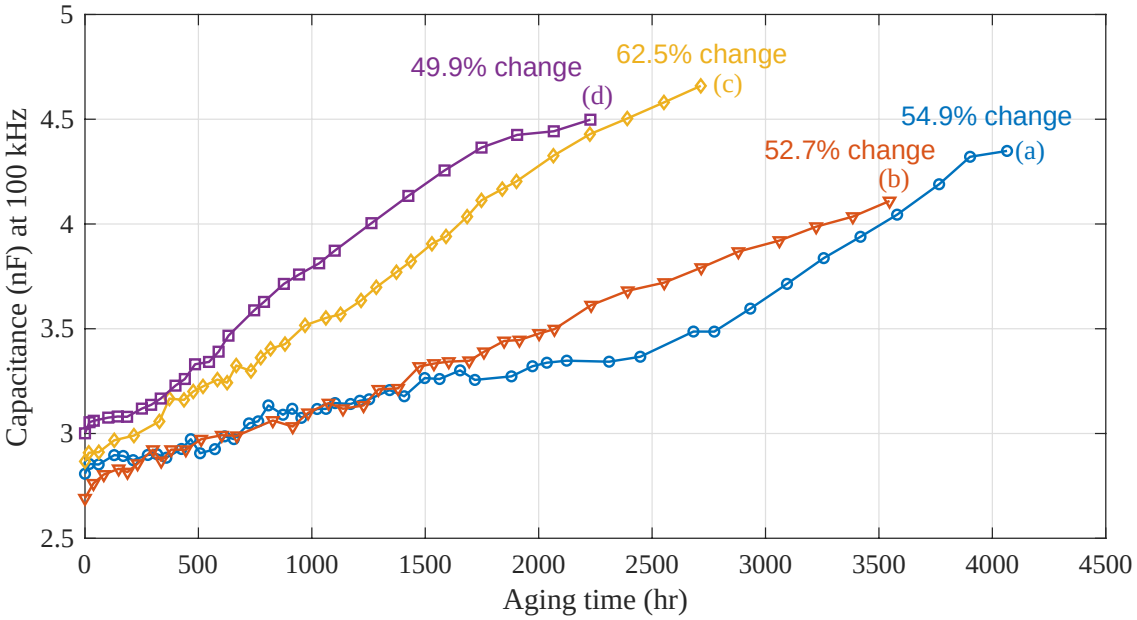

Figure 3.14: Insulation capacitance measured at $f = 100$ kHz for all coil samples: (a) Coil 1; (b) Coil 2; (c) Coil 3; (d) Coil 4. The percent change for each sample is also noted in the figure.

The insulation resistance behaves according to the law first proposed by Jaques Curie [67] and Egon Ritter von Schweidler [68], which is also stated in IEEE Standard 43 [69]. According to this law, sometimes called the "universal response", when a DC voltage is placed across a dielectric, the current will decrease according to a power law. Assuming the current will reach a steady-state value, the current as a function of charging time can be expressed as in Equation 3.14.

$$i\left(t\right) = at^{-b} + c \tag{3.14}$$

Here, $i\left(t\right)$ is the current as a function of time, t, a is the short-time current, b is the decay rate, and c is the steady-state current. In IEEE Standard 43, a is said to be a function of the particular insulation system and the applied voltage, and b is said to be a function of the particular insulation system. While IEEE 43 does not specify the exact nature of the steady-state current, it is reasonable to say that c is a combination of leakage and conduction currents and is a function of the particular insulation system (which includes the insulation material) and the applied voltage. This power law response is related to the Debye response, which claims the current through a dielectric will decrease according to an exponential model, rather than a power law. A power law can be considered as a weighted infinite sum of exponential functions with infinitely many time constants, as shown in Equation 3.15:

$$t^{-n} = \frac{1}{\Gamma\left(n\right)} \int_0^\infty \tau^{-n-1} e^{-t/\tau} d\tau, \tag{3.15}$$

where $\Gamma()$ is the Gamma function.

To find the initial values of these parameters for each coil, a voltage was placed across the insulation in the coil for 13.8 hours, and the current was sampled once every 5 seconds. Three such measurements for one coil are shown in Figure 3.15. The raw current data are shown through 13.8 hours (or 49,680 seconds) and the curve fits are extrapolated to show the steady-state behavior of the curves. The models were fit using non-linear least squares, where instead of adjusting the curve using according the squared residuals, a least absolute residual (LAR) scheme was employed, which reduced the influence of outliers in the fitting algorithm.

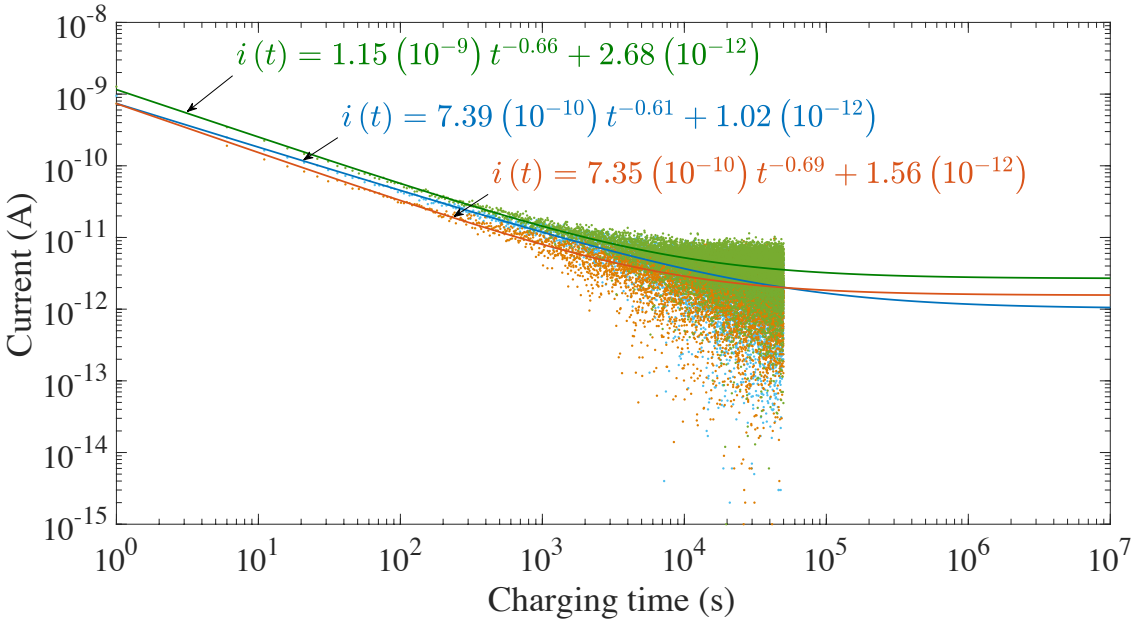

Figure 3.15: Three separate measurements of insulation current on a single coil (Coil 4). The insulation was subjected to 100 VDC for 13.8 hours and the current sampled once every 5 seconds. There are curve fits for each measurement extrapolated to show steady-state behavior.

The insulation current values over the lifetime of Coil 1 are shown in Figure 3.16. The current measurements were taken once per second for 20 minutes at a voltage of 100 VDC. Initially, the insulation behaved according to the "universal law," but as it aged, the behavior began to resemble that of an Ohmic material, i.e., the current remained relatively constant after the application of voltage.

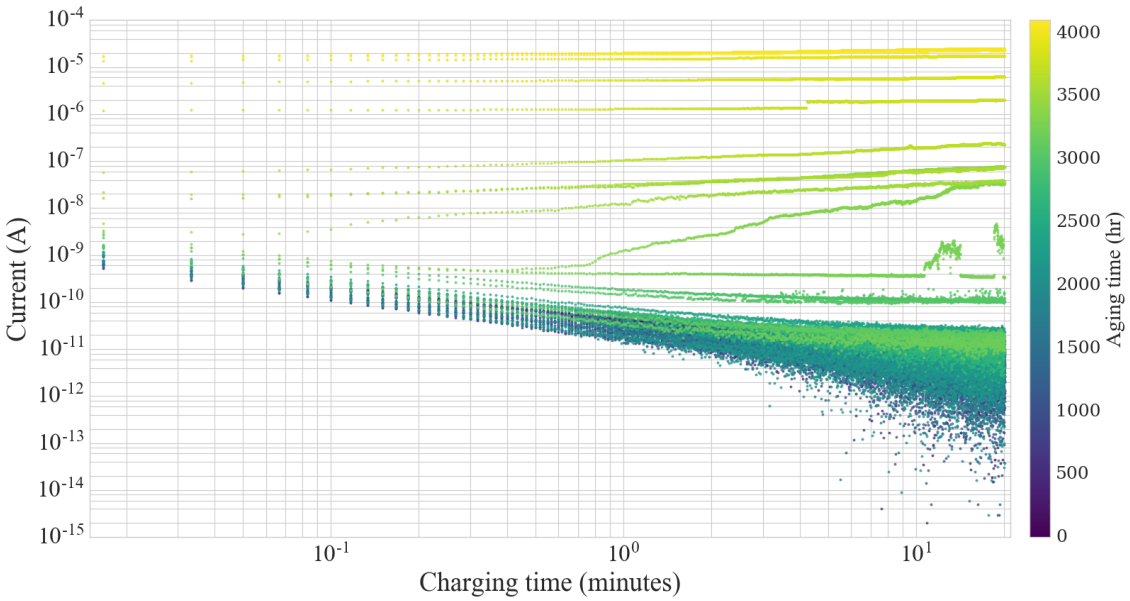

Figure 3.16: Insulation current over the lifetime of Coil 1 when subjected to a step voltage of 100 VDC for 20 minutes. The marker color indicates the aging time of the coil.

In Figure 3.17, the average value of insulation resistance for the final 1.5 minutes of charging is shown over the entire aging process. As the insulation aged, the value of the steady-state current changed. Initially, the resistance increased, but as the coil continued to age, the insulation resistance decreased. While insulation resistance changes gradually at the early stages of degradation, there is a point in the insulation lifetime where the insulation resistance decreases rapidly, from which the insulation resistance decreases until failure, which is defined in IEEE Standard 43 as insulation resistance less than 5 MΩ [69].

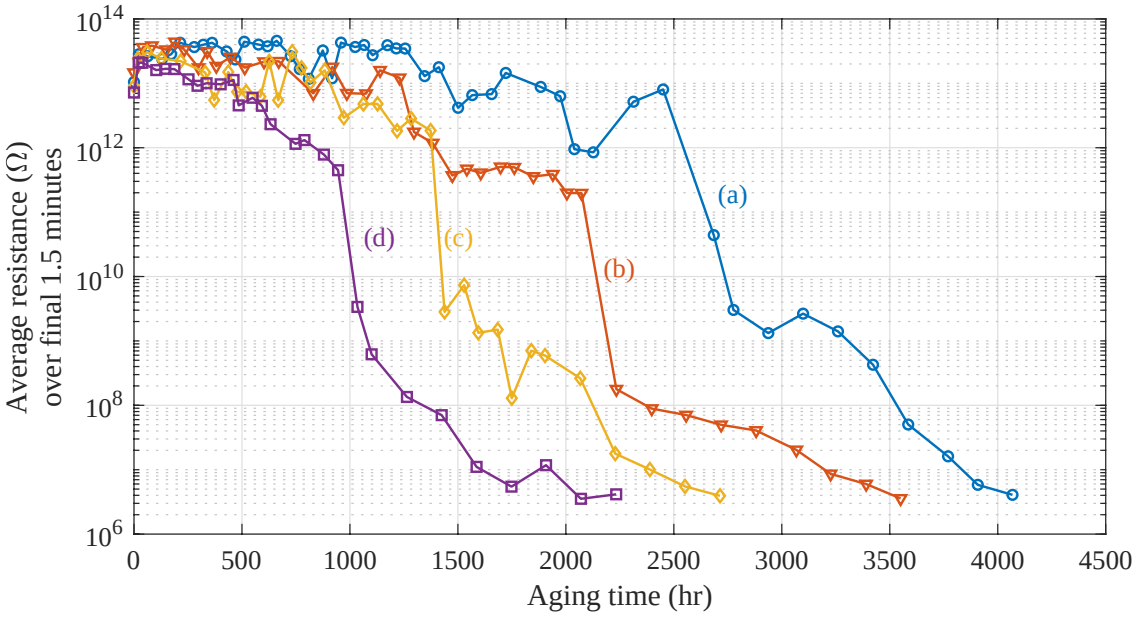

Figure 3.17: Average end-of-charging resistance values for all dual-wound coil samples: (a) Coil 1; (b) Coil 2; (c) Coil 3; (d) Coil 4.

Finally, the impedance measurements of one winding of Coil 1 are shown in Figure 3.18. As the coil aged, the resonant frequency decreased along with the magnitude of impedance at resonance. Over the course of the experiment, impedance measurements were performed for one winding for both Coil 1 and Coil 2, while both windings were measured for Coil 3 and Coil 4.

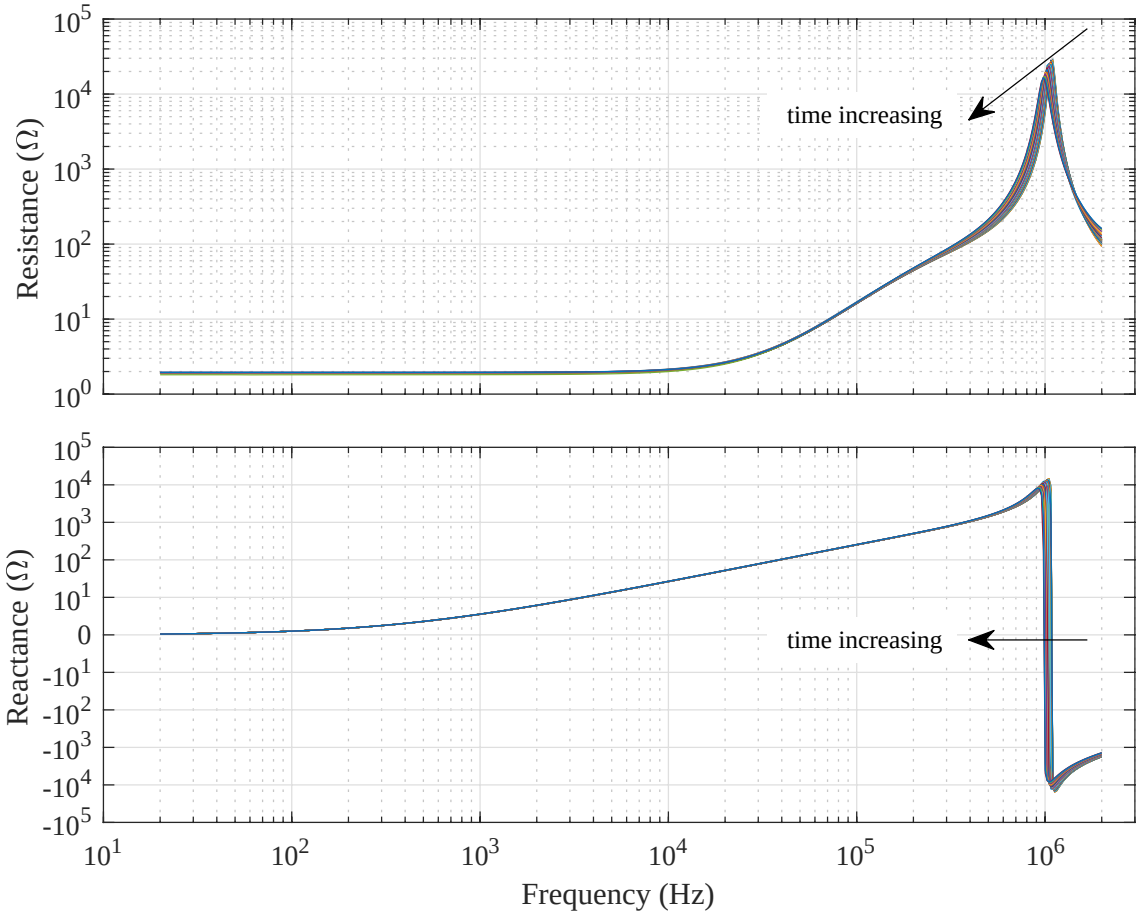

Figure 3.18: Impedance spectra of one winding in Coil 1. As the coil aged, the resonant frequency decreased along with the impedance magnitude at resonance, as indicated in the figure.

According the ECM proposed (see Figure 3.1), the resonant frequency is related to the insulation capacitance via Equation 3.4. This equation can re-arranged to:

$$L\omega_r^2 + \frac{R_c^2}{L} = \frac{1}{C} \tag{3.16}$$

Hence, the veracity of the hypothesized relationship between insulation capacitance and resonant frequency can be established by plotting the square of the resonant frequency against the inverse of capacitance. In Figure 3.19, the inverse of the insulation capacitance is plotted against the squared resonant frequency for four coils. For two of the coils (Coil 1 and Coil 2), the impedance was measured for only one winding; for the other two coils (Coil 3 and Coil 4), impedance was measured for both windings (second and third row of plots). The bottom four plots show the data from two coils, with the resonant frequency from each of the two distinct windings

on the coil. The Pearson correlation coefficient is shown in the upper left corner of each plot, quantifying the extent of the linear relationship between ω_r^2 and C^{-1}. The color of the data points indicates the aging time, proceeding from darker to lighter. These plots demonstrate the hypothesized relationship given the ECM, and moreover, provide a basis for estimating relative changes in insulation capacitance given resonant frequency measurements.

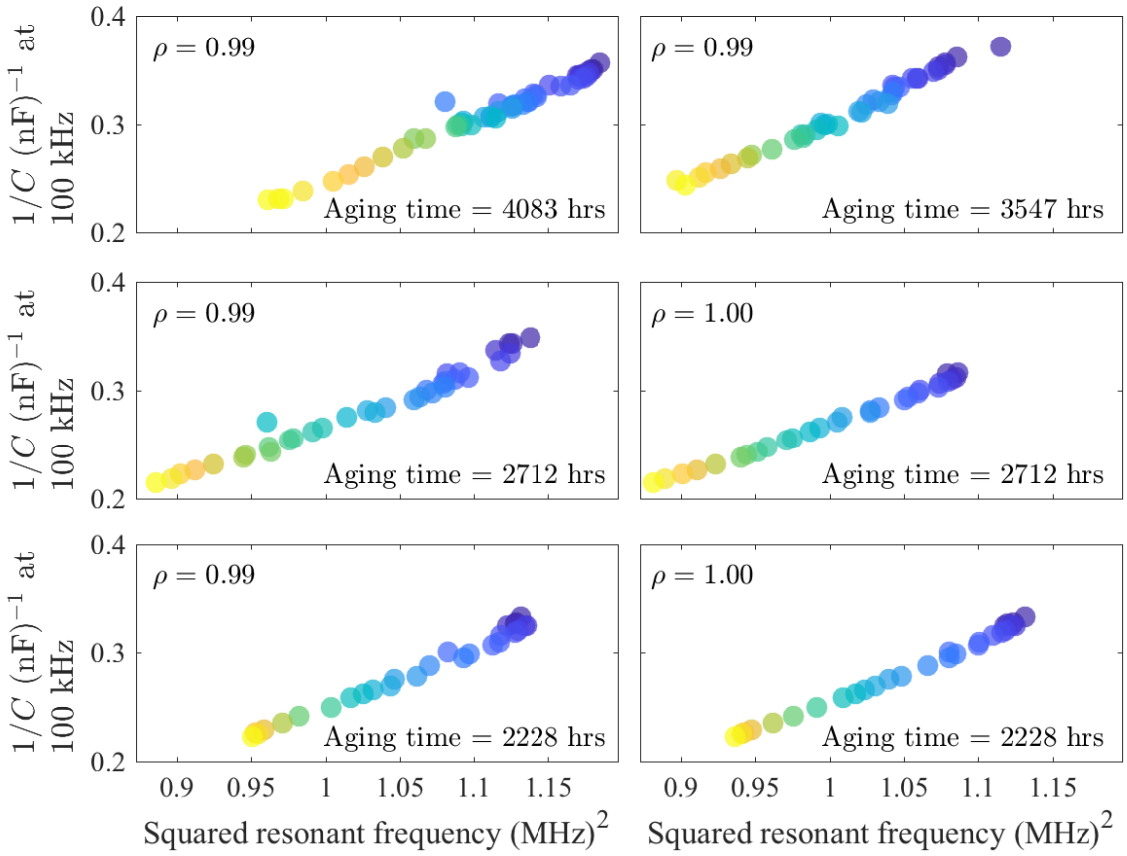

Figure 3.19: Inverse of capacitance plotted against the square of the resonant frequency. The Pearson correlation coefficient is shown in the upper left corner of each subfigure, quantifying the linear relationship between inverse capacitance and squared resonant frequency shown in Equation 3.16. The relationship is plotted for Coil 1 (upper left), Coil 2 (upper right), Coil 3 (middle row), and Coil 4 (bottom row). The color of the data points indicates the aging time, proceeding from darker to lighter.

The data from the winding impedance can be evaluated using the Spearman correlation spectrum, where the Spearman correlation coefficient is plotted against frequency. The Spearman correlation spectrum can be enhanced by sizing each data point according to the linear slope of the time series at a particular frequency, thus providing an understanding of not only which frequencies are sensitive to changes in the insulation electrical parameters, but also the degree of the aforementioned

sensitivity. The data point size represents the slope of a best-fit line through the time series.

From the Spearman correlation spectra shown in Figures 3.20 and 3.21, the behavior of resistance and reactance over the given frequency range can be observed. Below resonance, both resistance and reactance evolve in the same direction as insulation capacitance and in the opposite direction as insulation resistance. Above resonance, reactance evolves in the same direction as insulation capacitance and in the opposite direction as insulation resistance, while resistance has differing behaviors above resonance: at some frequencies, resistance evolves in the same direction as insulation resistance and in the opposite direction as insulation capacitance, while at higher frequencies, resistance evolves in the same direction as insulation capacitance and in the opposite direction as insulation resistance. At resonance, resistance changes from positive to negative correlation, while reactance shows negative correlation at a small range of frequencies around resonance. Importantly, the frequencies where resistance and reactance are most sensitive to changes in insulation parameters are those close to resonance. However, at frequencies below 10 kHz, the Spearman correlation coefficient for resistance lies between 0.25 and 0.75, which indicates that the strength of the positive monotonic trends is weak.

Consider the sensitivity analysis on the equivalent circuit model performed earlier in this section (see Section 3.2). This analysis predicted that the reactance would evolve in the same direction as insulation capacitance at all frequencies except a small range around resonance, where reactance is expected to evolve in the opposite direction as insulation capacitance. On the other hand, the analysis showed that at frequencies below resonance, reactance is expected to evolve in the same direction as insulation resistance, while at frequencies above resonance, reactance is expected to evolve in the opposite direction as insulation resistance. Given that insulation capacitance increased while insulation resistance decreased, the Spearman correlation spectra for reactance show that reactance is more sensitive to changes in insulation capacitance than insulation resistance. Though between about 10 kHz and 200 kHz, the Spearman correlation coefficient slightly decreases, which may indicate the influence of the reduced insulation resistance.

The sensitivity analysis further showed that below resonance, resistance is expected to evolve in the same direction as insulation capacitance, and in the opposite direction as insulation resistance. At frequencies above resonance, resistance is expected to evolve in the opposite direction of insulation capacitance and insulation resistance. Hence, given insulation capacitance increased and insulation resistance decreased, resistance is expected to generally increase at frequencies below resonance. This is realized in the provided results, except between 20 Hz and about 10 kHz, where the Spearman correlation coefficient is weak, lying between 0.25 and 0.75.

Table 3.4 shows the maximum absolute percent change for the electrical parameters of coil impedance, and the frequencies (if applicable) at which these changes occurred. The greatest values of linear slope for both resistance and reactance are in the frequency region around resonance. Furthermore, the greatest magnitude of percent change occurs in resistance at frequencies just below resonance, which

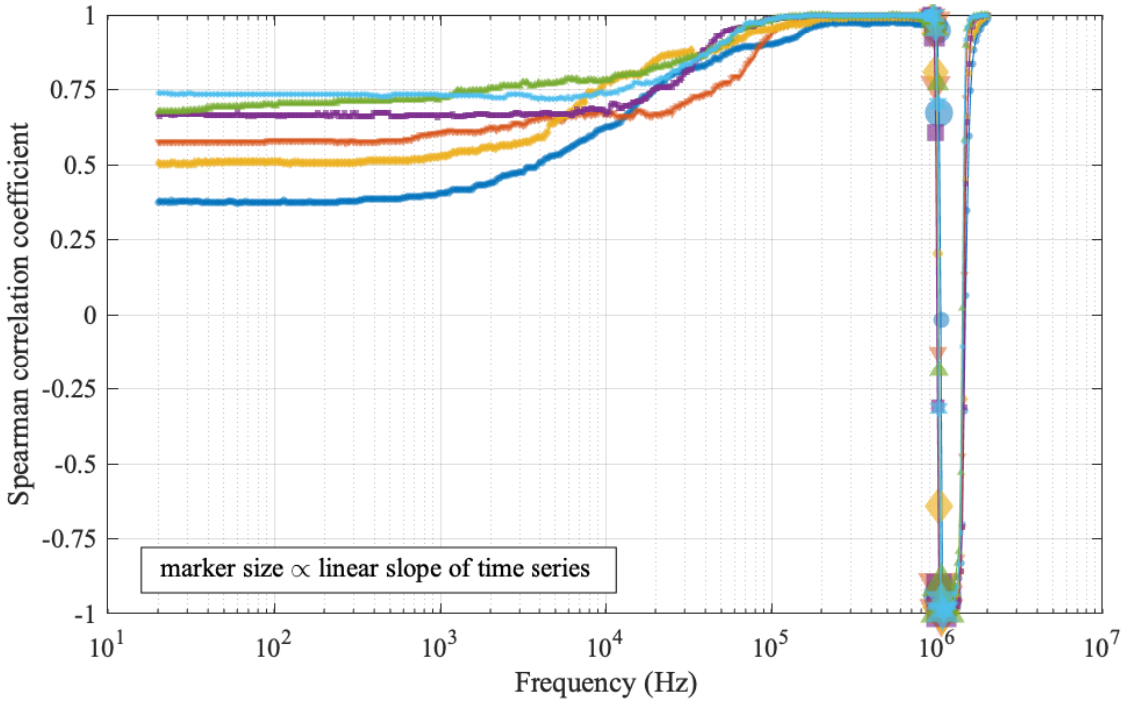

Figure 3.20: Resistance Spearman correlation spectra of 6 windings from Magnecomp dual-wound coils. The size of each data point marker is directly related to the slope of the linear fit of the time series at that particular frequency.

is where the prior sensitivity analysis predicted the greatest sensitivity to changes in insulation capacitance and resistance. At these frequencies, the changes in insulation resistance and insulation capacitance are compounded. The difference in percent change values between the resistance and reactance measurements and resonant frequency reinforce the conclusion that resonant frequency is not the most sensitive parameter to be measured. This is in agreement with the predicted behavior and provides a basis for improved insulation health monitoring using coil impedance measurements.

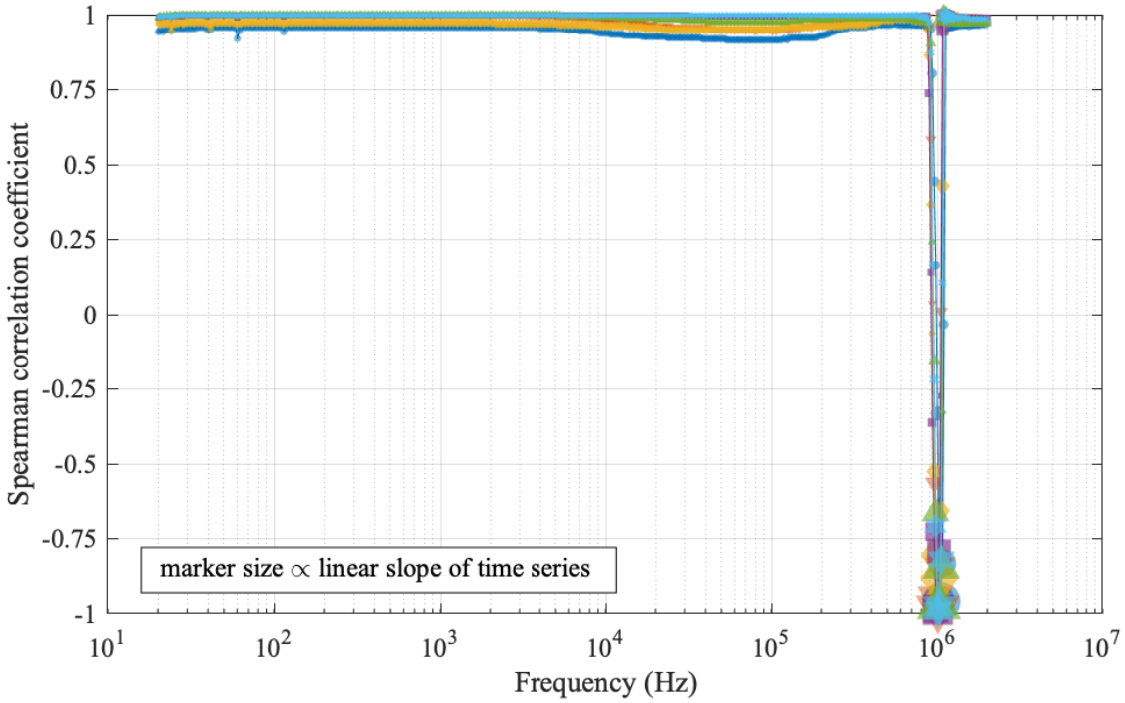

Figure 3.21: Reactance Spearman correlation spectra of 6 windings from Magnecomp dual-wound coils. The size of each data point marker is directly related to the slope of the linear fit of the time series at that particular frequency.

Table 3.4: Parameter values and their respective percent's change for the four dual-wound coils. For resistance and reactance, the highest absolute values of percent change are shown along with the frequency at which this value occurs. A positive percent change implies a decreasing value, while a negative percent change implies an increasing value.

Parameter	Percent change	Frequency
Capacitance	103.7, 96.8, 107.8, 85.7	20 Hz, 20 Hz, 20 Hz, 20 Hz
Insulation resistance	100, 100, 100, 100	–
Resonant frequency	9.45, 9.99, 11.75, 9.04	–
Resistance	-403.8, -465.9, -556.2, -386.0	957.3 kHz, 914.2 kHz, 914.2 kHz, 935.5 kHz
Reactance	185.6, 290.5, 207.4, 194.8	1.07 MHz, 1.05 MHz, 1.03 MHz, 1.05 MHz

3.4.3 Temporal Correlation

A pertinent line of inquiry is into how the Spearman correlation coefficient changes over time. The results of such an inquiry should reveal the amount of time (as a percentage of the total lifetime of the coil) is necessary for the impedance measurements to converge to the Spearman correlation spectrum as measured near the end of insulation useful life (i.e., those in Figures 3.20 and 3.21). For a given frequency, the cumulative Spearman correlation coefficient can be computed as:

$$\rho\left(t\right) = 1 - \frac{6}{n_{1:t}\left(n_{1:t}^2 - 1\right)} \sum_{i=1}^{n_{1:t}} d_i^2, \tag{3.17}$$

where $n_{1:t}$ represents the number of measurements between the first data point and the tth data point, and $d_i = x_i - y_i$ is the difference between the ranks of the data points included in the measurements from 1:t. The lowest value taken by t is t_2 (i.e., correlation requires at least two data points).

As mentioned earlier in this chapter, for Coil 1 and Coil 2, the impedance was measured for only one winding, while for Coil 3 and Coil 4, impedance was measured for both windings. For Coil 3, the measurement of the second winding was not started until about 370 hours into the experiment, which is the explanation for the missing data at the lower times of Figure 3.22(d) and Figure 3.23(d).

In both the resistance and reactance measurements, the Spearman correlation coefficients converge to the spectra shown in Figures 3.20 and 3.21 within the first approximately 25% of the total aging time. This demonstrates that, if necessary, the "best" features (i.e., the frequencies at which the impedance measurements show a Spearman correlation coefficient close to ± 1) emerge in a relatively short time, if one wants to cumulatively measure the correlation coefficient. This implies that one need not perform an entire lifetime experiment with a given coil design in order to find the frequencies that are best to monitor. One simply needs to measure the impedance until the Spearman correlation spectrum converges (plus some temporal factor of safety to ensure convergence has been reached). Once convergence of the Spearman correlation spectrum is reached, these results suggest that it is likely to be very close to the final correlation spectrum.

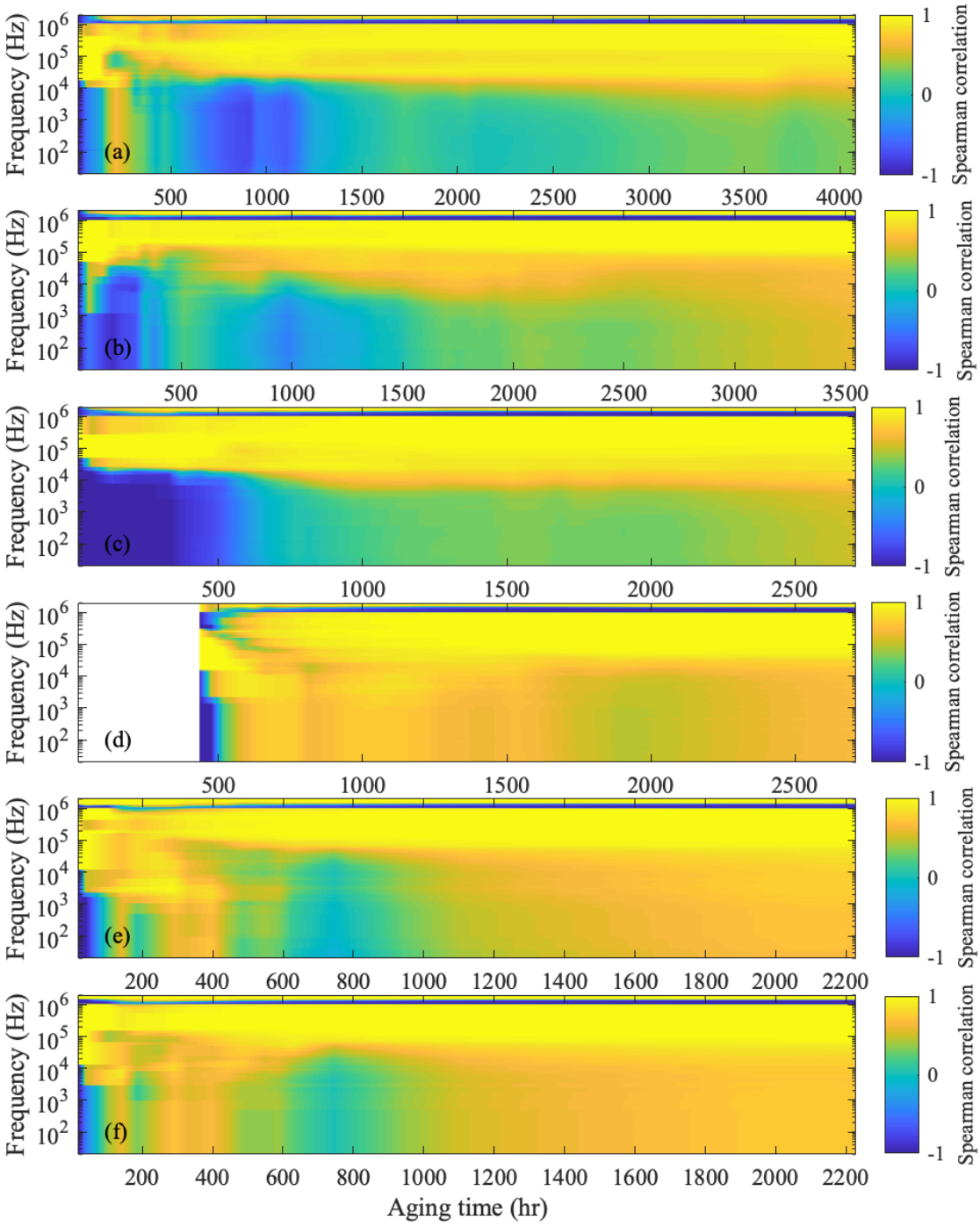

Figure 3.22: Temporal changes in Spearman correlation coefficient for the double-wound coil resistance. The y-axis is the frequency, the x-axis is the aging time, and the color shows the Spearman correlation coefficient. The relationship is plotted for (a) Coil 1 (b) Coil 2; (c) first winding of Coil 3; (d) second winding of Coil 3; (e) first winding from Coil 4; and (f) second winding from Coil 4.

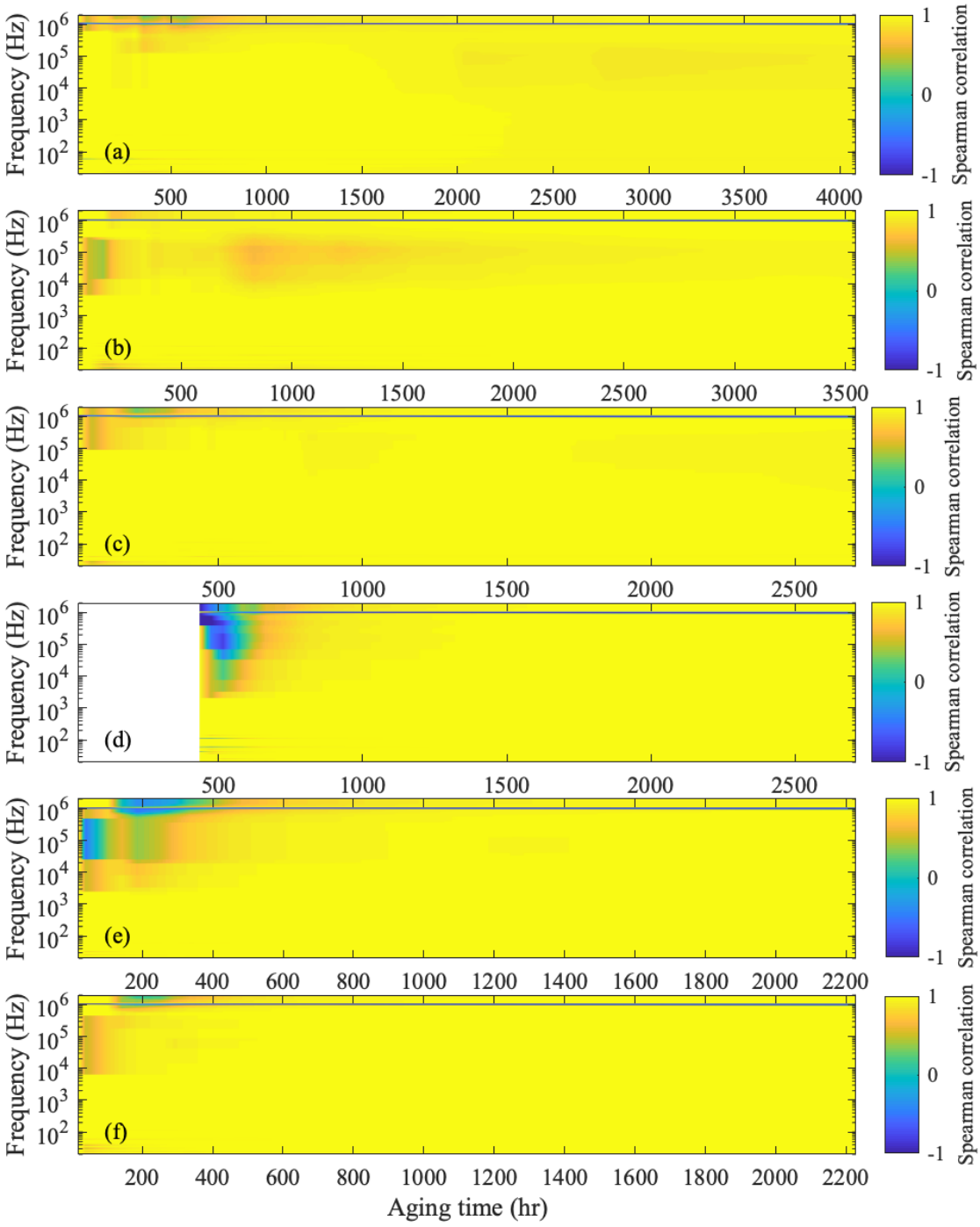

Figure 3.23: Temporal changes in Spearman correlation coefficient for the double-wound coil reactance. The y-axis is the frequency, the x-axis is the aging time, and the color shows the Spearman correlation coefficient. The relationship is plotted for (a) Coil 1 (b) Coil 2; (c) first winding of Coil 3; (d) second winding of Coil 3; (e) first winding from Coil 4; and (f) second winding from Coil 4.

Chapter 4: Insulation Mechanical Property Analysis

The mechanical properties of the insulation can play an important role in gaining insight into the root cause of the insulation failure. In associating the changes in mechanical properties with the evolution of the impedance spectra, we can gain understanding into the hidden physical process(es) evidenced by impedance measurements. The previous chapter showed how the electrical parameters change for an aromatic polyimide insulation material. In this chapter, the same dual-wound coils are used to understand how the modulus of elasticity and hardness of the material change during thermal aging. In Chapter 6, additional analysis is provided on "loose" magnet wire (magnet wire not used in a coil) with the same insulation material, showing the evolution of the modulus of elasticity and hardness as it thermally aged.

4.1 Test Setup

The mechanical properties of the insulation were measured using nanoindentation. This is a method where, using load-displacement data and contact mechanics, certain mechanical properties of the sample can be computed. Traditionally, in order to measure the modulus of elasticity, upon unloading the tip from the material, the slope of the load versus displacement curve is computed. In this work a continuous stiffness module was used to measure the contact stiffness during the loading process. The stiffness is related to the reduced modulus according to Equation 4.1.

$$S = \frac{dP}{dh} = \frac{2}{\pi}\beta E_r \sqrt{A} \tag{4.1}$$

In Equation 4.1, S is the stiffness of the contact, which can include contributions from the sample under test and the testing device; β is a correction factor; E_r is the "reduced" modulus or "combined modulus of the system", which combines the modulus of the indenter and the specimen [70]; A is the projected area of indentation at the contact depth, h_c; P is the load; and h is the displacement. The projected area is typically taken to be a function of the contact depth, often approximated by a fitting polynomial. In this work, the projected area was computed as $A = 24.56h_c^2$ [70]. The contact depth is calculated as $h_c = h_{\max} - \varepsilon P/S$, where $h_{\max}$ is the maximum penetration depth of the tip, and ε is the tip geometric factor. These concepts are illustrated in Figure 4.1.

The sample modulus of elasticity is computed according to Equation 4.2. Here, the subscript i indicates a property of the indenter tip, the subscript s indicates a

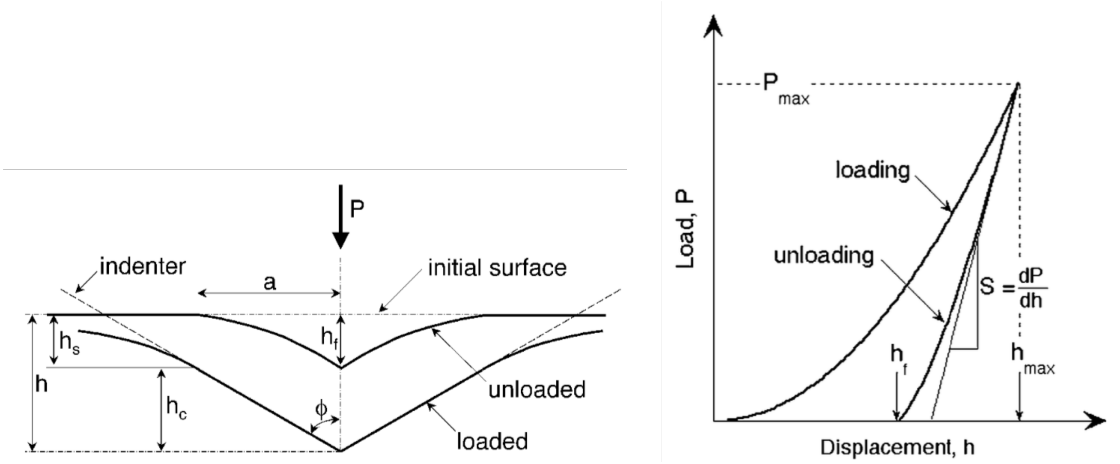

(a) Nanoindenter displacement into material (b) Nanoindenter load vs. displacement

Figure 4.1: Nanoindentation terminology (illustrations taken from [71]).

property of the specimen, and ν is Poisson's ratio.

$$\frac{1}{E_r} = \frac{1-\nu_i^2}{E_i} + \frac{1-\nu_s^2}{E_s} \tag{4.2}$$

Hardness, H, is generally taken as the mean contact pressure at a condition of a fully developed plastic zone [70]. It is calculated according to Equation 4.3.

$$H = \frac{P_{\max}}{A} \tag{4.3}$$

For the present work, modulus of elasticity and hardness were measured using nanoindentation with a Berkovich tip, which is shown in Figure 4.2. Poisson's ratio for the sample was taken as $\nu_s = 0.3$, the geometric factor for a Berkovich tip is $\varepsilon = 1.034$, and the correction factor is $\beta = 1.8326$.

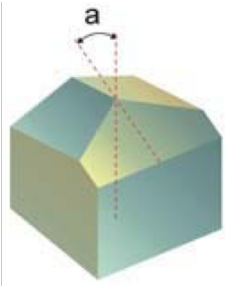

Figure 4.2: Berkovich nanoindenter tip.

There are dynamic methods for measuring the mechanical properties of a sample using nanoindentation that allow for the measurement of properties as a function of penetration depth, referred to as continuous stiffness measurement (CSM). In this

case, an oscillatory force is superimposed onto the conventional load-displacement response. Considering a single oscillatory force applied with a frequency, ω, and amplitude, P_0:

$$P(t) = P_0 e^{j\omega t} \tag{4.4}$$

The resulting displacement, h, will have the same frequency of oscillation but a phase difference, ϕ, will be introduced.

$$h(t) = h_0 e^{j(\omega t + \phi)} \tag{4.5}$$

There are several dynamic models models that can be employed to separate the dynamics of the instrument and tip-sample interactions. For more information about these models see [70] (Chapter 7). The maximum depth varied across samples from $h_{\max} = 1500$ nm to $h_{\max} = 5000$ nm, and the maximum load varied along with the maximum depth (i.e., a higher maximum depth implies a higher maximum load). However, as mentioned, the properties were measured as a function of penetration depth, and the final material property values were attained by taking an average across a range of depths.

Several authors [71–73] showed that when a sharp nanoindenter tip (such as the Berkovich tip) is interacting with a bulk, homogeneous material, there is a linear relationship (with zero y-intercept) between load and dynamic stiffness squared (i.e., $P = as^2$, where P is load, s is the dynamic contact stiffness, and a is the slope). When examining the CSM nanoindentation response, one must choose the depths over which to average the measurements to produce the final material property value. Given this linear relationship between load and stiffness squared, it is necessary to find depths over which the ratio between load and stiffness squared is constant (i.e., $P/s^2 =$ constant). However, the ratio between load and stiffness squared is often quite small and it is challenging to find the depths over which it is constant, so, in this research, the inverse ratio, s^2/P, was used.

The measurements were taken from wire samples located in the vertical center of the coils and from 4 layers within the coil (1, 3, 5, & 8). This is illustrated in Figure 4.3.

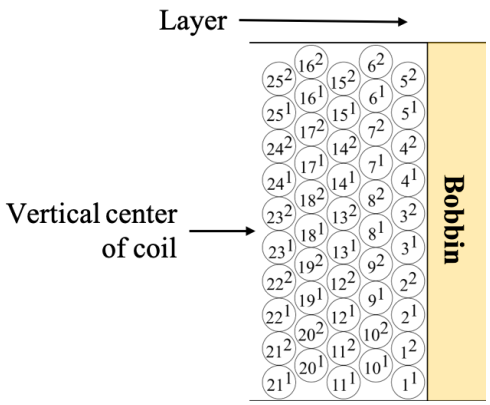

Figure 4.3: Wire insulation samples were taken from the vertical center of each coil and from 4 layers within the coil (layers increase moving from outside to inside of the coil).

4.2 Measurement Results

4.2.1 Modulus of Elasticity and Hardness

Great care must be taken when interpreting the measurements from nanoindentation. When using CSM, property measurements are produced as a function of penetration depth, yet, for a homogenous material (we reasonably assume the insulation is homogeneous), the modulus of elasticity and hardness are a single value, which means these properties cannot be dependent upon depth of penetration. However, the modulus of elasticity and hardness of the material are contained within the penetration depth dependent response. The question then concerns the depths of penetration over which we can safely assume that the bulk insulation material is being probed. As mentioned earlier, the ratio of stiffness squared to load, s^2/P, was used to determine these depths. Shown in Figure 4.4 are measurements of s^2/P versus penetration depth for a single coil, indicating the regions of depth that were used to compute the final reported values of insulation modulus and hardness.

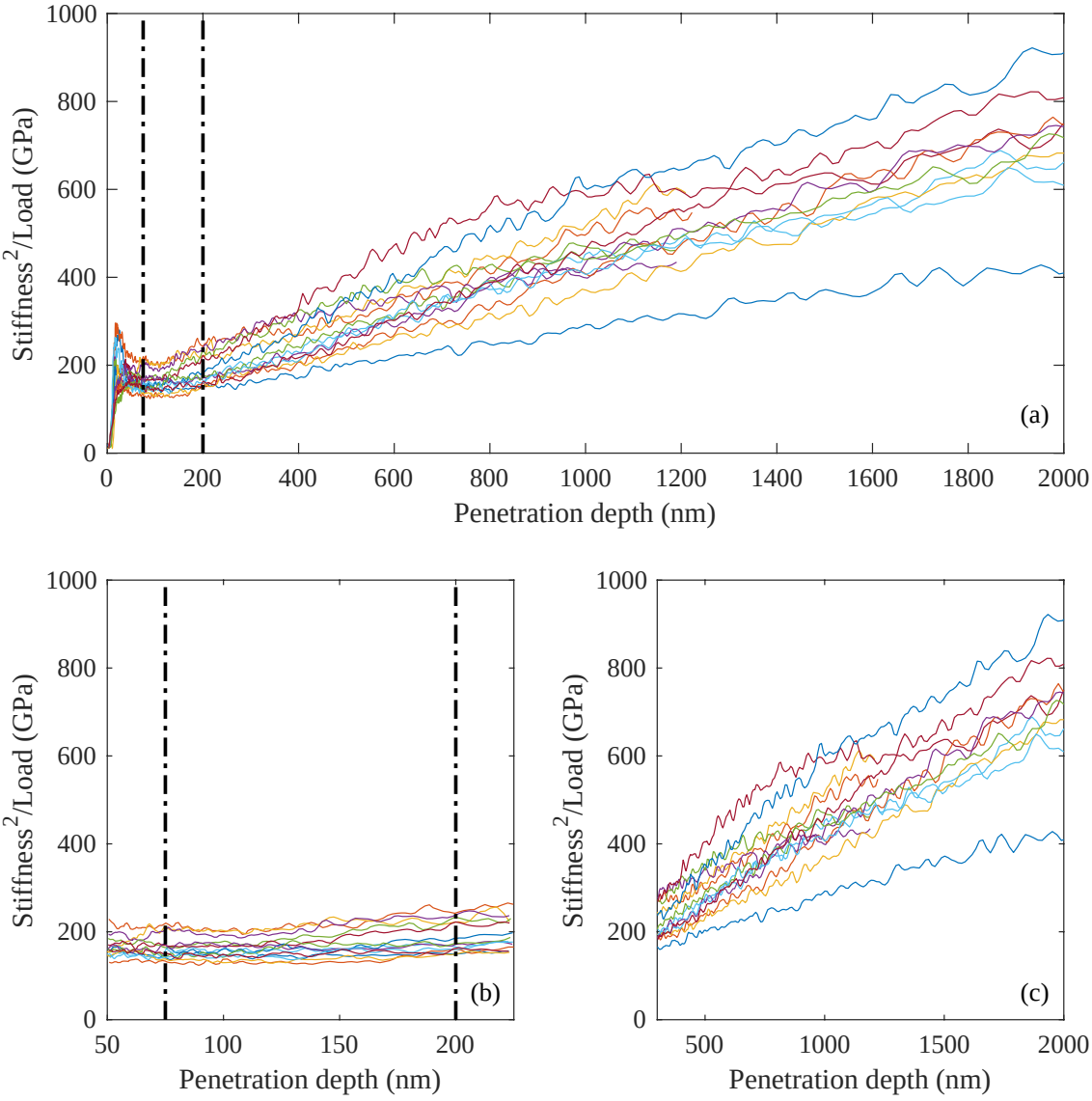

Figure 4.4: Dynamic stiffness squared divided by load, s^2/P, plotted against penetration depth for Coil 4, layer 5. Each line is a single indentation into the insulation at a unique location. The dash-dot lines indicate the depth region over which each line of s^2/P was approximately constant, and thus where measurements of modulus and hardness were taken to be representative of the insulation material properties. In these regions, the data points that make up each line were averaged to produce the final reported property value. In (a), the entire penetration depth range is shown; in (b), the depth over which each line was averaged is shown; and in (c), the values above the computed property region are shown.

The output modulus of elasticity measurements for the same coil as shown in Figure 4.4 are shown in Figure 4.5. The y-axis of this figure is labeled as "Measured Modulus of Elasticity" in order to distinguish between the values shown in the plot

and the true modulus of elasticity of the insulation material. The true modulus of elasticity and hardness was estimated by averaging the individual data points in each line over the depths between 75 nm and 200 nm for the aged insulation, and 100 nm and 1000 nm for the healthy insulation.

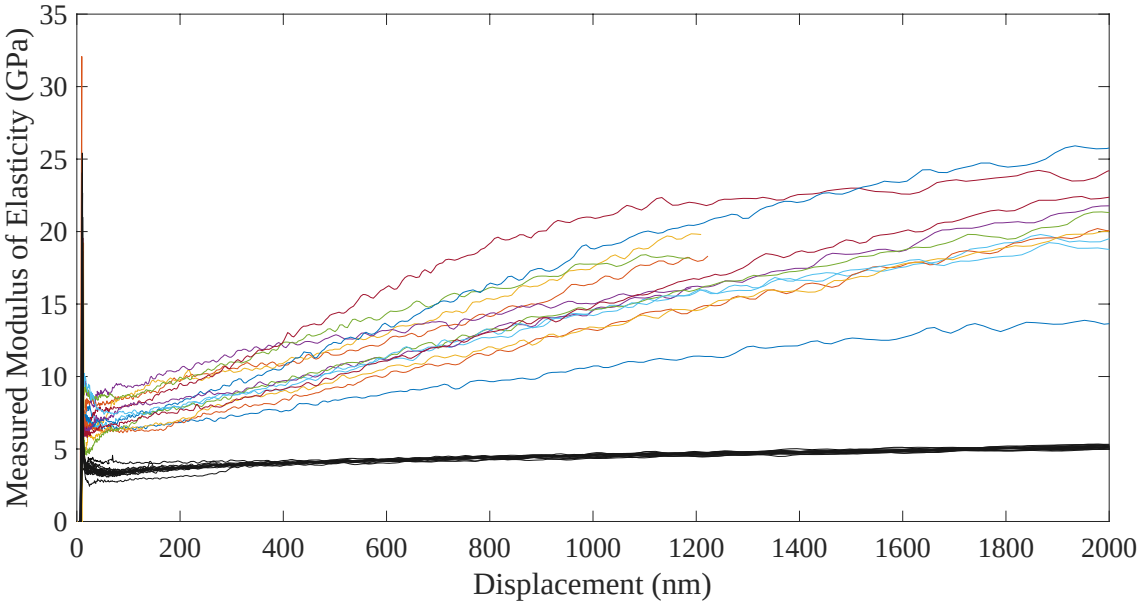

Figure 4.5: Output modulus of elasticity measurements plotted against indentation depth for Coil 4, layer 5 compared against the same measurements for the healthy insulation sample. The black lines are measurements taken from the healthy insulation sample, while the colored lines are the measurements taken from Coil 4, layer 5. As noted in Figure 4.4, the individual data points that make up each line were averaged over the depths between 75 nm and 200 nm to produce the final, reported modulus of elasticity measurements. The same procedure was used to produce the hardness values.

The computed values of the modulus of elasticity measurements for all 4 dual-wound coils are shown in Figure 4.6, and the values of hardness for each of the dual-wound coils are shown in Figure 4.7. These measurements were made after the coils were aged and are compared with a healthy sample of the magnet wire insulation. The boxplots shown in Figure 4.6 and Figure 4.7 are composed of at least 10 indents per sample. The whisker length is taken as the largest or smallest value that falls with the whisker window, which is computed as $q_3 + 1.5 \times (q_3 - q_1)$ for the upper window, and $q_1 - 1.5 \times (q_3 - q_1)$ for the lower window, where q_1 and q_3 are the first and third data quartiles, respectively. All outliers (red '+' marks) are those measurements that fall outside the whisker length.

The aged insulation registers a higher modulus and hardness than the healthy insulation at every measured layer in the coil (for most indentation samples). This could be taken as an indication that the insulation has become more brittle, lowering the resistance of the insulation to fracture in the presence of mechanical stresses.

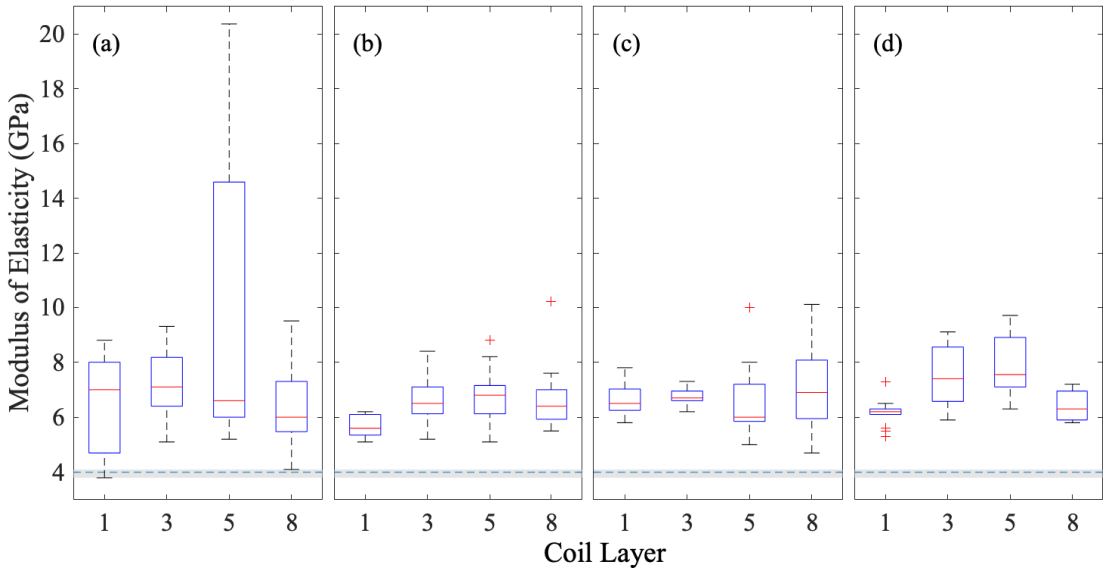

Figure 4.6: Modulus of elasticity for coil insulation samples at 4 layers within each dual-wound coil for (a) Coil 1; (b) Coil 2; (c) Coil 3; and (d) Coil 4. The dashed line and gray area shows the median value and 99% distribution of the healthy insulation modulus of elasticity measurements. The median of the healthy insulation modulus was 4.0 GPa, while the maximum value was 4.1 GPa and the minimum value was 3.8 GPa.

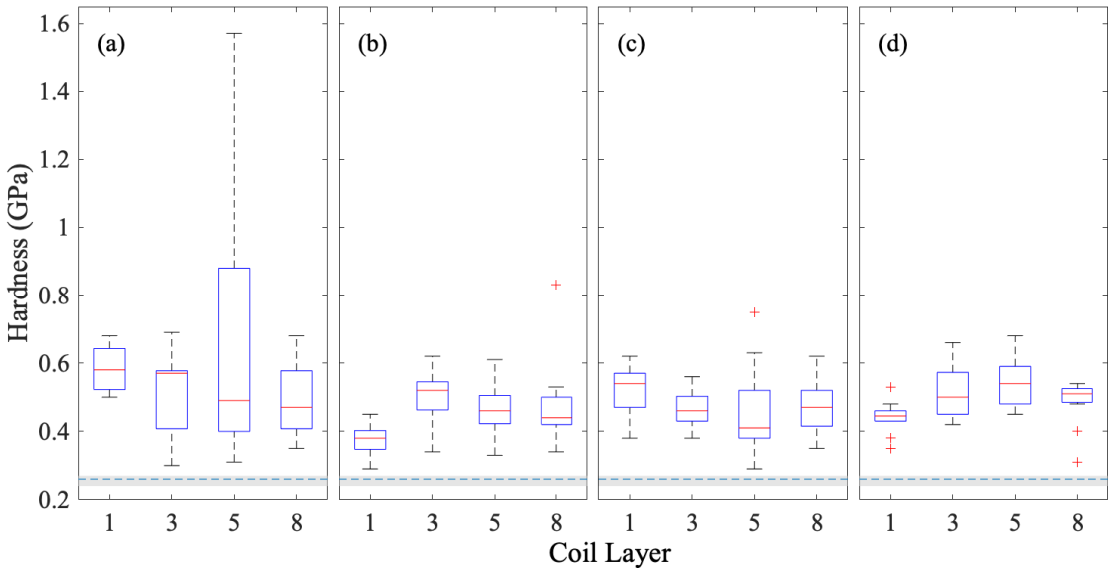

Figure 4.7: Hardness for coil insulation samples at 4 layers within each dual-wound coil for (a) Coil 1; (b) Coil 2; (c) Coil 3; and (d) Coil 4. The dashed line and gray area shows the median value and 99% distribution of the healthy insulation hardness measurements. The median of the healthy insulation hardness was 0.26 GPa; the maximum was 0.27 GPa and the minimum was 0.24 GPa.

4.2.2 Fracture Toughness

The study of brittleness is closely related to that of material fracture toughness, which is a measure of how resistant a material is to fracture once a defect is present. Fracture toughness is a measure of material brittleness and can be measured using the ratio of modulus of elasticity to hardness, E/H. The Lawn-Evans-Marshall (LEM) model [74–76] proposed that fracture toughness be computed according to Equation 4.6:

$$K_c = \alpha \frac{P_{\max}}{c^{3/2}} \left(\frac{E}{H}\right)^n, \tag{4.6}$$

where α is a calibration constant, c is the crack length measured from the center of contact to the end of the corner radial crack, and n is 1/2. Others [77, 78], among other slight differences, determined n to be 2/3. Nevertheless, the ratio of modulus of elasticity to hardness remains. This is sensible considering that a brittle material is one in which there is a tendency to fracture with very little or no detectable plastic deformation beforehand. Hardness measures the material's resistance to localized plastic deformation, modulus of elasticity measures the material's resistance to elastic deformation, and toughness is the amount of energy a material can absorb before fracture. Hence, this ratio, E/H, tends to be small for brittle materials because elastic and plastic deformations allow materials to absorb energy. The boxplots of the ratio of modulus of elasticity to hardness are shown in Figure 4.8.

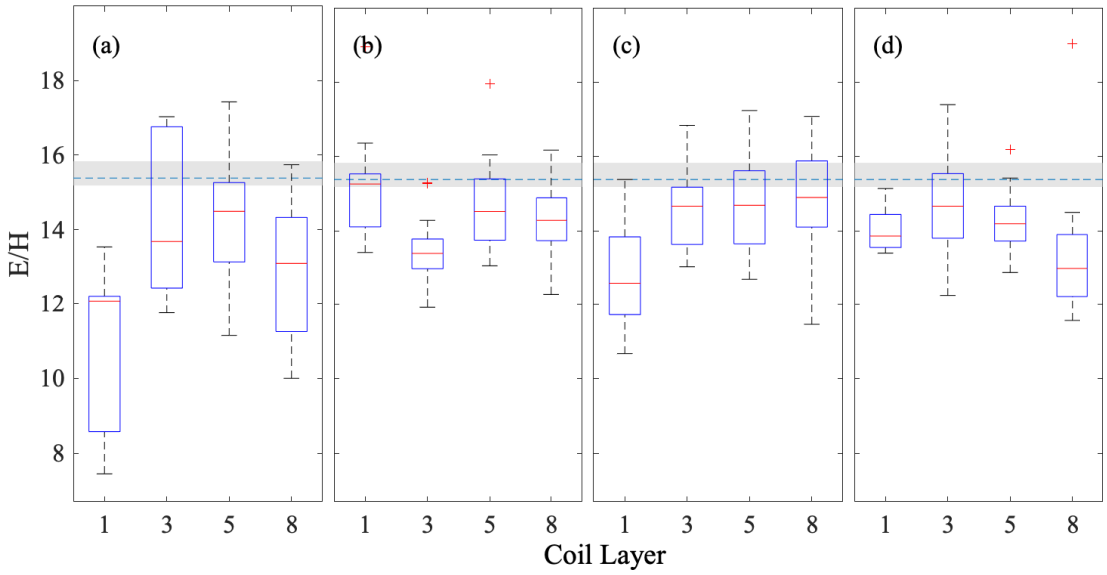

Figure 4.8: Ratio of E/H for coil insulation samples at 4 layers within each dual-wound coil for (a) Coil 1; (b) Coil 2; (c) Coil 3; and (d) Coil 4. The dashed line and gray area shows the median value and 99% distribution of the healthy insulation E/H measurements. The median of the healthy insulation E/H was 15.38; the maximum was 15.83 and the minimum was 15.19.

Kruskal-Wallis and ANOVA (analysis of variance) statistical tests were performed on each of the dual-wound coils and the corresponding layers to test for similarity between the E/H measurements of the aged insulation and the healthy insulation. The significance values for each test are shown in Tables 4.1 and 4.2. According to the Kruskal-Wallis calculations, the null hypothesis can be rejected (meaning the distributions are distinct) in 11/16 cases with a significance value of $p < 0.01$, while using ANOVA, 9/16 cases reject the null hypothesis with a significance value of $p < 0.01$. In all cases, the median value of the aged coil insulation samples lies below the median value of the healthy samples. And in all cases but 1 (Coil 2, layer 1), the median value of the aged coil insulation samples lies outside (below) the 99% distribution of the healthy samples.

A second method of understanding the fracture toughness of the insulation material was suggested by Toivola *et al.* [79] and expanded upon by Oyen and Cook [80] for cases where crack observation may not be possible. Here it was suggested to use the load-displacement trace for discontinuities by examining the P-h gradient, dP/dh. A single load-displacement trace is shown in Figure 4.9.

Table 4.1: Significance values for Kruskal-Wallis non-parametric test between aged insulation sample and new insulation sample E/H calculations.

		Layer number			
		1	3	5	8
Coil number	1	0.0000	0.4548	0.0050	0.0035
	2	0.1445	0.0000	0.0077	0.0001
	3	0.0000	0.0014	0.1151	0.2722
	4	0.0000	0.0425	0.0003	0.0002

Table 4.2: Significance values for ANOVA test between aged insulation sample and new insulation sample E/H calculations.

		Layer number			
		1	3	5	8
Coil number	1	0.0000	0.0780	0.0182	0.0000
	2	0.3317	0.0000	0.0197	0.0001
	3	0.0000	0.0044	0.0297	0.0848
	4	0.0000	0.0183	0.0001	0.0005

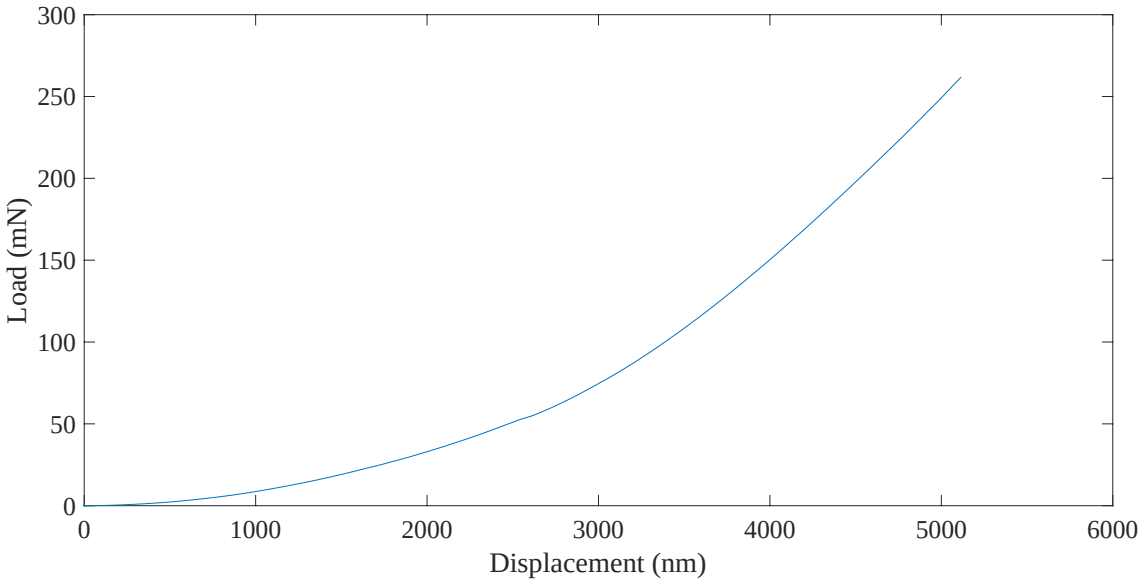

Figure 4.9: Load-displacement trace for a single indent on an insulation sample from Coil 4, layer 1.

One way to test for discontinuities in the load-displacement trace is to evaluate the error associated with a best-fit line through the data. If the fit is appropriate for the data, then the error should be zero-mean and approximately normally distributed, and a higher standard deviation of the error will imply a greater number of discontinuities in the data. Examining the load-displacement trace suggests that it can be fit with a power function, $P = ah^b$. Hence, gradient of the load-displacement trace is also a power law function, $dP/dh = abh^{b-1} = ch^d$. The analysis procedure is to differentiate the load-displacement data, fit a power law function to the result, and then examine the standard deviation of the error between the power law fit and the differentiated data. The resulting boxplots are shown in Figure 4.10. It should be noted that for each of the fits, the coefficient of determination, R^2, was computed (an appropriate goodness-of-fit measure for power functions), and none of the fits yielded a value less than 0.95 (out of a perfect value of 1).

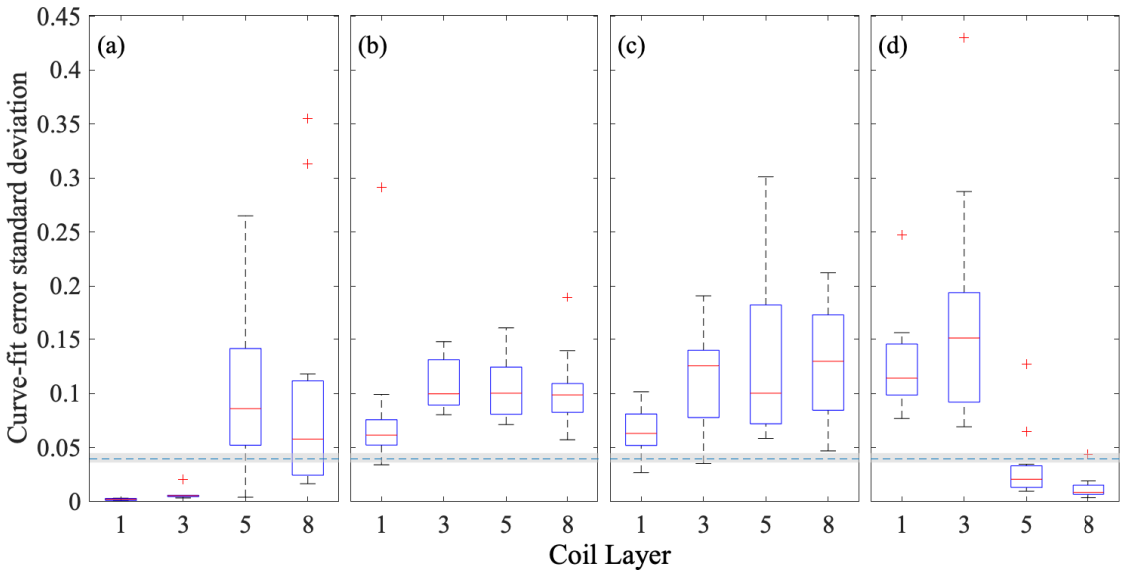

Figure 4.10: Standard deviation of the error between dP/dh data and the corresponding power law curve fit for coil insulation samples at 4 layers within each dual-wound coil for (a) Coil 1; (b) Coil 2; (c) Coil 3; and (d) Coil 4. The dashed line and gray area shows the median value and 99% distribution of the healthy insulation measurements.

In general, the error standard deviation is larger for aged samples than for new samples. While this evidence is less definitive than the previous E/H analysis, given that samples from four layers are almost entirely below the healthy measurements, it still lends credence to the hypothesis that the aged insulation has a lower fracture toughness than the new insulation.

4.2.3 Insulation Thickness

A possible explanation for the increase in capacitance is a decrease in the insulation thickness. This is a direct conclusion from a parallel plate capacitor model, which says $C = k\epsilon_0 A/d$, where C is the capacitance, k is the relative permittivity of the dielectric material, ϵ_0 is the permittivity of empty space, A is the area of the electrode plates, and d is the distance between the electrodes. Hence, capacitance is inversely proportional to the distance between the electrodes. Given the mechanical expansion of the copper wire in a coil due to Joule hearing, along with the increased pliability of the polymer due to the increased temperature, the thickness of the insulation may decrease in the location where it is compressed by the copper wire. Furthermore, the elevated temperature will cause chemical changes in the insulation which will alter the permittivity of the material, including evaporation of components of the insulation. Unfortunately, in this work, a direct measurement of the thickness of the insulation after aging was not possible. When disassembling the coils after aging, the insulation was found to be "flaky", meaning pieces of the insulation would simply flake off the wire. Thus it was challenging to acquire a piece of magnet wire with a fully intact circumference of insulation. Hence, two pieces of evidence are used to support the hypothesis that the insulation became thinner over the course of aging. The weight loss of the insulation and the bobbin from each coil is shown in Figure 4.11. These numbers were calculated by subtracting the weight of the copper conductor, which can be found using the coil resistance, cross-sectional area of the magnet wire, coductor and density of copper, from the total weight. Hence, the result is the weight of the insulation plus the weight of the bobbin. This shows that over the course of aging, the insulation and bobbin lost mass, which in the case of insulation weight loss, could indicate a decreased thickness between the copper conductor wires. Moreover, cross-referencing this image with Figure 3.14 shows that the coil that lost the most weight also had the greatest increase in capacitance, and the coil that lost the least amount of weight had the lowest increase in capacitance; the other two lost similar amounts of weight and had similar increases in capacitance. It should be noted that aromatic polyimides are known to lose weight even at the relatively low temperatures used in this experiment. Hondred *et al.* [81] stated: "A simple isothermal TG analysis of Kapton HN [a general purpose Kapton film] at 150°C for 1 h shows 2–3% weight loss and then stabilizes with no additional weight loss, indicating the removal of water from the sample." Hence, it is likely that a portion of the computed weight loss percentage is due to weight loss of the polyimide insulation.

A second, and perhaps more persuasive, piece of evidence that points to the thinning of the insulation is the nanoindentation data. During nanoindentation, the indenter is driven deeper into the specimen and if there is a substrate of different material beneath the specimen, the properties of the substrate can begin to influence the measurement. If two different specimens show the influence of the substrate at different depths, given that they are otherwise the same material, it can be inferred that one is thinner than the other. An example of this shown in Figure 4.12.

The aged samples began as identical to the new samples, so after aging, the

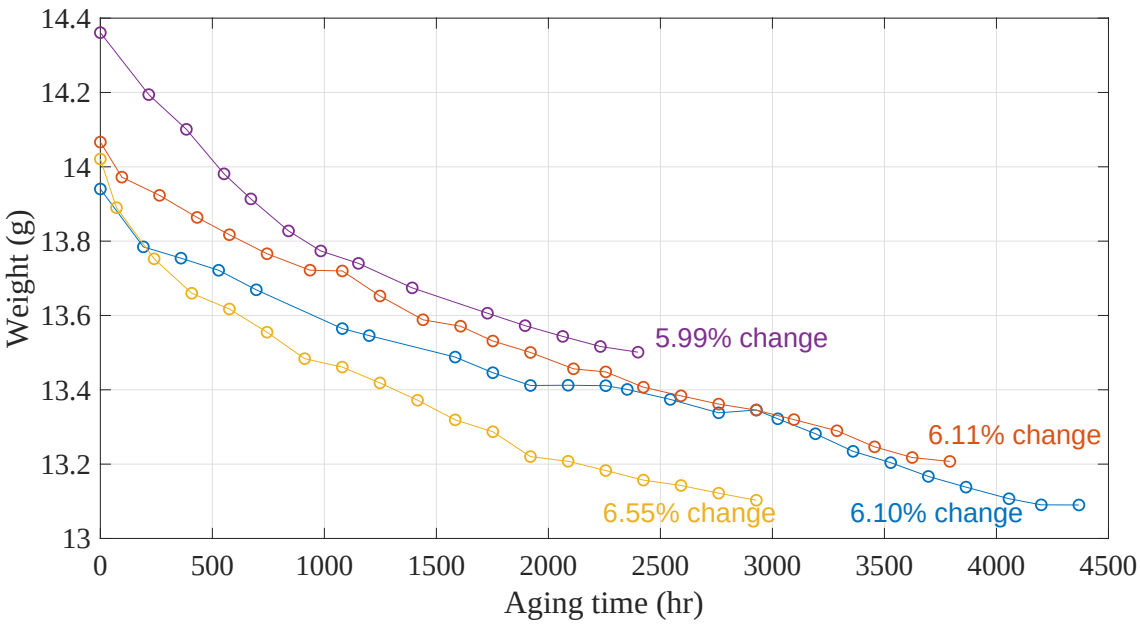

Figure 4.11: Insulation and bobbin weight from the dual-wound coils over the aging period. The insulation and bobbin weight was computed by subtracting the weight of the copper (found using DC resistance and cross-sectional area, along with known quantities of density and resistivity) from the weight of the coil. The percents change are also shown in the figure.

influence of the copper wire on the measurements is apparent. Since the modulus of copper is much higher than that of polyimide, the copper causes the measured modulus of the aged samples to increase. However, there is no similar increase in the new samples. Taken in conjunction with the weight loss data, it is likely that the thickness of insulation between the conductors in the coils decreased.

The analysis presented in this chapter gives credence to the idea that the insulation material becomes more brittle, and thus more susceptible to fracture, as it ages. This suggests a failure mechanism that involves the mechanical stress of the expanded copper (due to Joule heating) acting on the increasingly brittle insulation, ultimately resulting in fracture and turn-to-turn shorting.

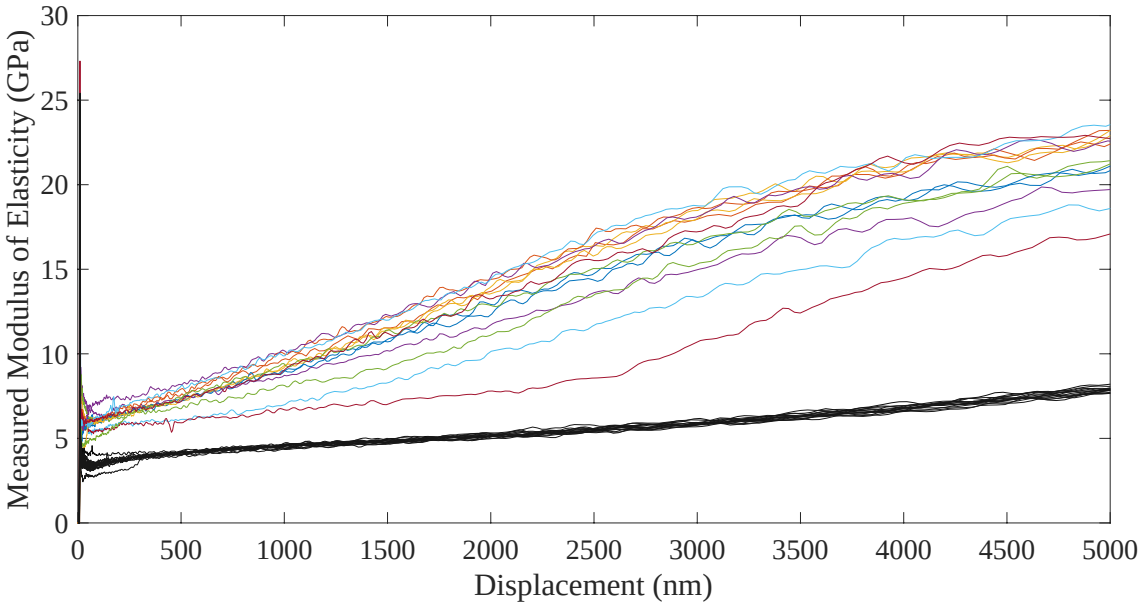

Figure 4.12: Measured modulus of elasticity plotted against indentation depth for Coil 4, layer 1 compared against the same for the healthy insulation sample. The black lines are measurements taken from the healthy insulation sample, while the colored lines are the measurements taken from Coil 4, layer 1.

Chapter 5: Insulation Chemical Property Analysis

A holistic understanding of insulation degradation must account for changes in chemical properties in addition to the electrical and mechanical properties studied in previous chapters. In this chapter, the insulation from dual-wound coils used in the prior analyses is examined using Fourier transform infrared (FT-IR) spectroscopy.

5.1 Fourier Transform Infrared Spectroscopy

FT-IR is a technique that can be used to probe the chemical bonds within a material. Essentially, infrared (IR) spectroscopy measures the electromagnetic radiation absorbed or emitted by a chemical species associated with changes in its vibrational energy state. In order for electromagnetic radiation to be emitted or absorbed, a molecule must produce an oscillating dipole moment [82]. The resulting bond vibrations are generally described as: symmetric and anti-symmetric stretching, twisting, bending, and rocking. These modes are illustrated in Figure 5.1. The nature of the functional group determines the frequency at which vibrations are observed.

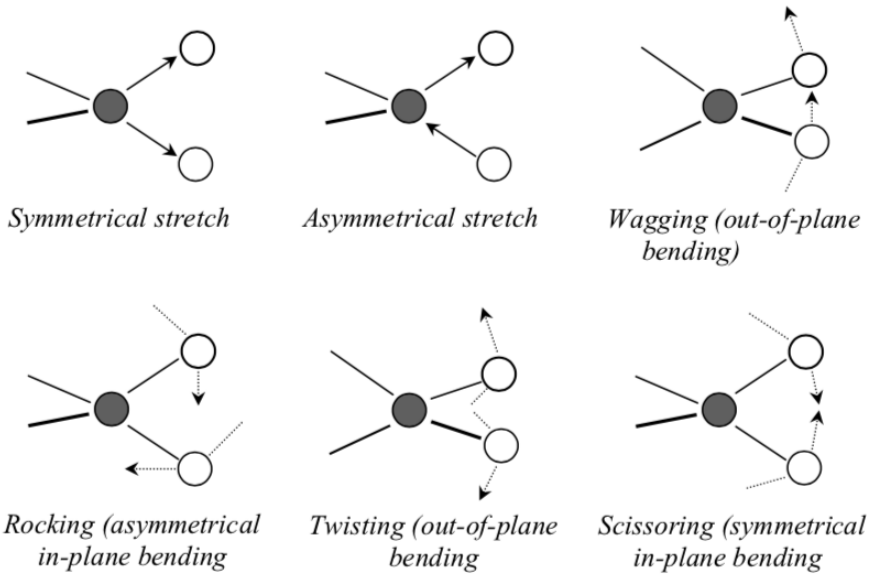

Figure 5.1: Examples of vibrational modes for methylene group (illustration taken from [83]).

The IR portion of the electromagnetic spectrum spans wavenumbers from 14000 to 20 cm^{-1}. This is generally divided into three sub-regions: near-IR (14000 to 4000 cm^{-1}), mid-IR (4000 to 200 cm^{-1}), and far-IR (200 to 20 cm^{-1}). Most fundamental vibrational frequencies for organic materials, such as magnet wire insulation, are found in the mid-IR range.

In this study, the attenuated total reflection (ATR) method was used in conjunction with an Agilent Cary 6000 FT-IR microscope. The use of a microscope allowed for the magnet wire sample to be placed under the IR crystal, and the insulation IR spectra to be measured without removal of the insulation from the magnet wire. The measured wavenumbers spanned from 4000 cm^{-1} to 700 cm^{-1}.

5.2 Measurement Results

The insulation material is an aromatic polyimide [66]. However, the exact chemical structure is unknown. Dupont's Kapton is an aromatic polyimide that is also used in insulation applications. The chemical structure for Kapton is shown in Figure 5.2.

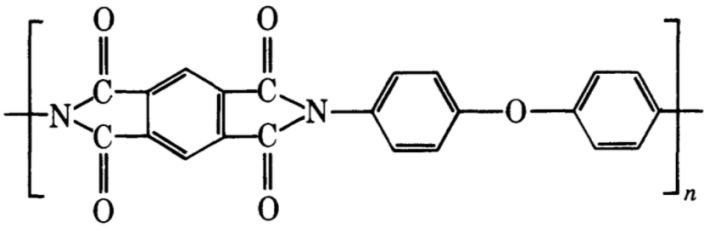

Figure 5.2: Chemical structure of Kapton, an aromatic polyimide (illustration taken from [84]).

As in the previous chapter, 4 layers of each dual-wound coil were measured. The samples were taken from the same location on the coil as those used to measure the mechanical properties. Each measurement consisted of an average of 32 spectrum scans, each with a resolution of 4 cm^{-1}. After the initial measurement was performed, the spectrum was baseline corrected, and the region containing CO_2 was flatlined in the spectrum. While the use of the FT-IR microscope garnered significant benefits, one of the drawbacks of the technique is the need to embed the IR crystal in the material, ensuring that the IR signal is completely injected into the sample and the sensor measures the emitted radiation. While this produces repeatable measurements, it also causes the distance between the surface of the insulation material and the copper wire to be inconsistent across samples, which can lead to differences in absorption intensity. Hence, in order to compare samples, they must be normalized. Prior studies [44, 47, 85] determined that the imide ring remained intact during thermal aging, hence in order to compare the spectra from the healthy and aged insulation, the aged spectrum was normalized to the healthy insulation by ensuring the peaks at $\approx$ 1714 cm^{-1} were the same magnitude. In all the samples,

there is a wide band starting at about 2750 cm^{-1} and ending at about 3750 cm^{-1}, with a peak at about 3350 cm^{-1}. This corresponds with O–H and N–H bonds, which generally span from about 3200 cm^{-1} to 4000 cm^{-1} [86], and C–H bonds, which span from about 2800 cm^{-1} to 3300 cm^{-1} [86].

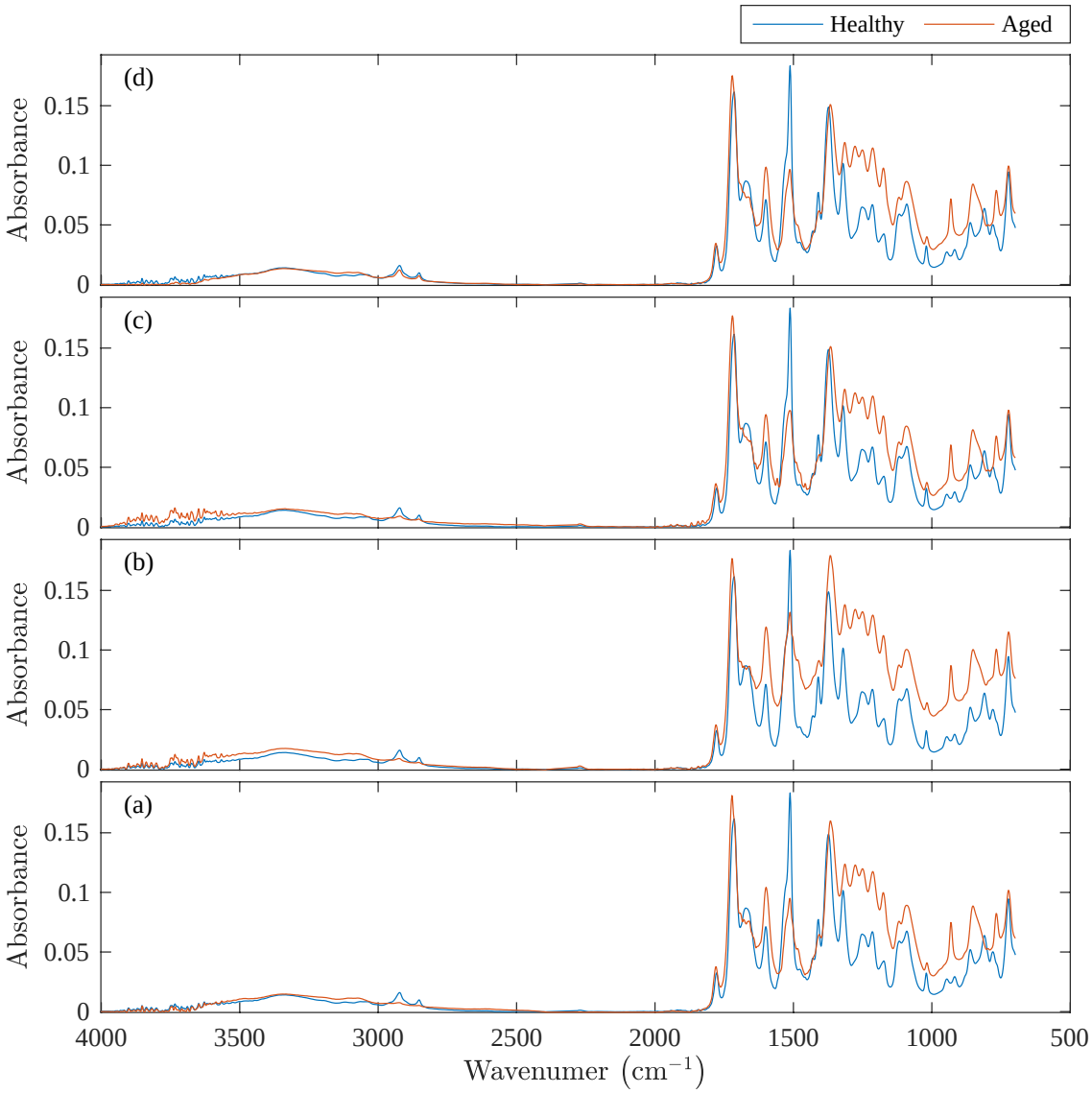

Figure 5.3: FT-IR results for layer 3 of the dual-wound coils: (a) Coil 1; (b) Coil 2; (c) Coil 3; (d) Coil 4. The two FT-IR curves were normalized to the peak of the healthy insulation at $\approx 1714\,\mathrm{cm}^{-1}$.

In Figure 5.4, the FT-IR spectrum from Coil 4, layer 3 is shown. In this figure, the locations that are common to both healthy and aged insulation spectra are noted with a "dash-dot" line. In this figure, support for the normalizing scheme is reinforced since the two curves are equal at points where the imide structure reveals itself [47, 85–88]: 1779 and 1720 cm^{-1} (asymmetric and symmetric C=O imide ring

stretching bands), 1373 cm^{-1} (C–N stretching band), and 723 cm^{-1} (imide ring deformation band).

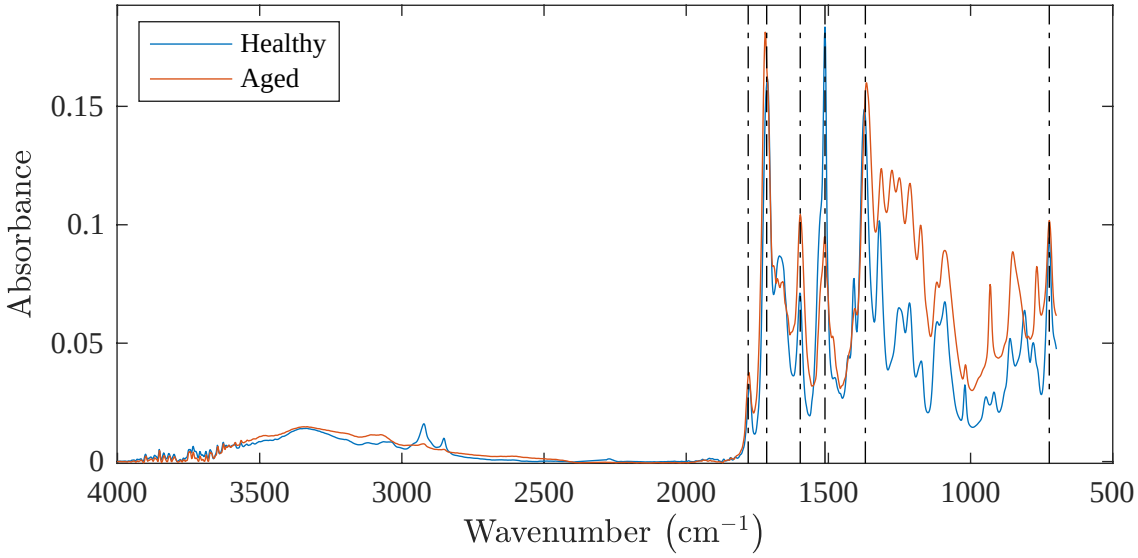

Figure 5.4: FT-IR measurements for Coil 4, layer 3 and the healthy insulation showing peaks that are in both spectra at the same wavenumbers. From left to right, the dash-dot lines indicate: 1779 cm^{-1} is imide ring asymmetric C=O stretch; 1720 cm^{-1} is imide ring symmetric stretch; 1599 cm^{-1} is aromatic C–C ring stretch; 1512 cm^{-1} is aromatic C–C ring stretch; 1370 cm^{-1} is C–N stretch; and 723 cm^{-1} is imide ring deformation.

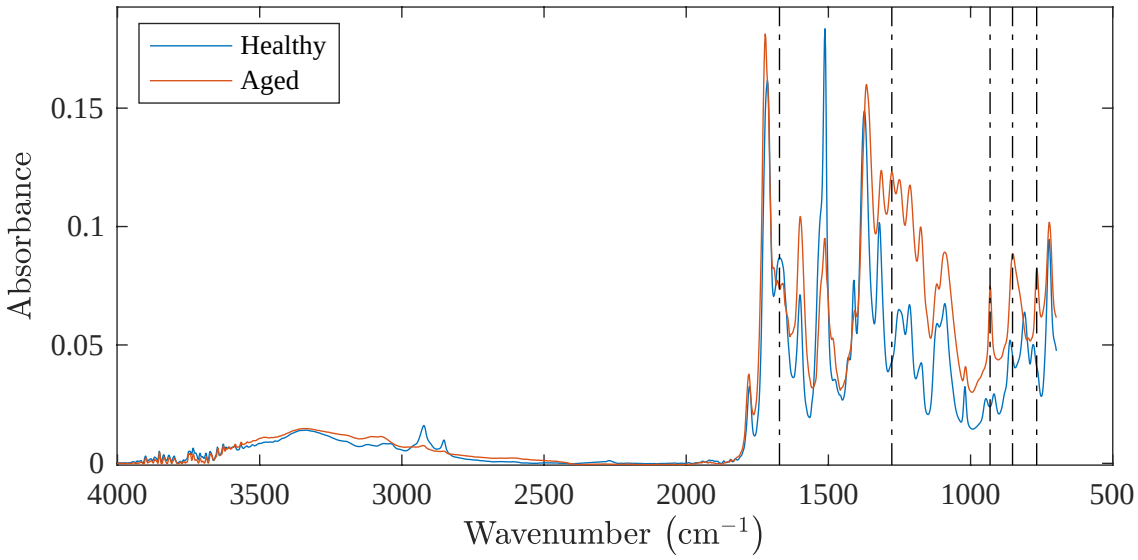

Figure 5.5: FT-IR measurements for Coil 4, layer 3 and the healthy insulation showing wavenumbers where there are differences between the two spectra. In the figure, dash-dot lines indicate wavenumbers where there is a noticeable difference between the two spectra (left to right): 1672 cm^{-1}, 1277 cm^{-1}, 931.4 cm^{-1}, 852.4 cm^{-1}, and 767.5 cm^{-1}.

Figure 5.5 shows the same sample (Coil 4, layer 3), with the dash-dot lines indicating the location of wavenumbers where there are noticeable growths or absences in the aged insulation. At 1672 cm^{-1}, the healthy insulation spectrum has a peak that is absent from the aged insulation spectrum. At 1277 cm^{-1}, 931.4 cm^{-1}, 852.4 cm^{-1}, and 767.5 cm^{-1}, there are peaks in the aged insulation spectrum that are absent from the healthy insulation spectrum. The plots containing these regions of interest are shown in Figure 5.6. Here, each peak and valley comparison between the healthy and aged insulation can be seen in greater detail.

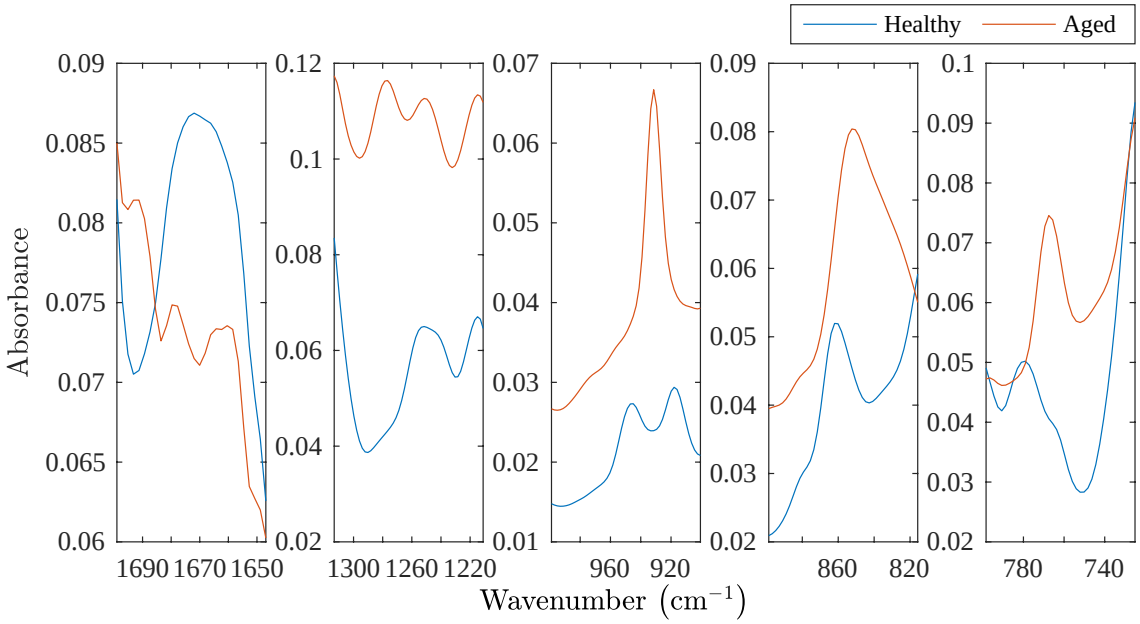

Figure 5.6: Each of the locations that were mentioned in Figure 5.5 are shown in more detail.

A different perspective on the FT-IR data is presented in Figure 5.7, where the aged insulation spectrum was subtracted from the healthy insulation spectrum $\left(\mathrm{IR}_{\mathrm{healthy}} - \mathrm{IR}_{\mathrm{aged}}\right)$. This reinforces many of the prior observations about where in the FT-IR spectra the differences between the materials lie. Furthermore, this plot helps to portray the regions of the spectrum where the healthy insulation shows a greater intensity versus those where the aged insulation shows a greater intensity.

From the FT-IR spectra and data presented, there are a few conclusions that can be drawn. It appears that the intensity of C–C aromatic bonds ($1514\,\mathrm{cm}^{-1}$) has decreased and this decrease is consistent across the samples. This suggests a cleavage of some benzene ring structures in the insulation during aging. However, it must be noted that it is not always possible to determine molecule concentration from IR intensity. Hence this conclusion is tentative.

There is a narrow band centered at $931\,\mathrm{cm}^{-1}$ in the aged insulation and at the same wavenumber, there is a notable dip (between two peaks at $918\,\mathrm{cm}^{-1}$ and $945\,\mathrm{cm}^{-1}$) in the healthy insulation. The aged insulation also has peaks at $767.5\,\mathrm{cm}^{-1}$ and $1277\,\mathrm{cm}^{-1}$. According to Bio-Rad's KnowItAll IR Spectral Library, these are associated with 3-ring ethers, with C–O–C bonds located in the regions: 1230-1280 cm^{-1} (symmetric stretching), 815-950 cm^{-1} (anti-symmetric stretching), 805-880 cm^{-1} (deformation), 775-850 cm^{-1} (deformation), and 750-770 cm^{-1} (deformation).

Taken together with the observed decreased concentration of aromatic C–C bonds, this leads to the possibility that for some of the polymer chains, the diethyl ether functional group ($\mathrm{C_6H_6–O–C_6H_6}$) splits at one of the benzene rings. This leaves the oxygen attached to one benzene ring on one side and to a hydrocarbon

of lesser degree than benzene. This finding is similar to one produced by Tsukiji *et al.* [85] who stated: "The absorption due to C−C and C−O groups and due to condensed ring are observed for the samples. On the other hand, the asymmetric stretching band due to the diphenyl-ether group and the aromatic ring stretching band do [*sic*] not observed. These results show that diphenyl-ether is damaged under long term thermal degradation and that imide rings are not damages seriously."

Based on this finding, it appears as though the polymer chain likely splits, resulting in shorter polymer chains on average throughout the material. This result is surprising when taken in conjunction with the results of the nanoindentation tests. Generally, a shorter polymer chain will result in lower modulus of elasticity. In this case, the polyimide modulus of elasticity increased. It is not clear how these results are congruent. However, one possibility is that the increase is caused by increased concentration of 3-ring ethers, which can be epoxides. For some materials, epoxide addition has been shown to increase the modulus of elasticity and hardness [89–91]. Hence, if the insulation is becoming epoxified, the modulus of elasticity and hardness could increase, and the chemical findings would be satisfied.

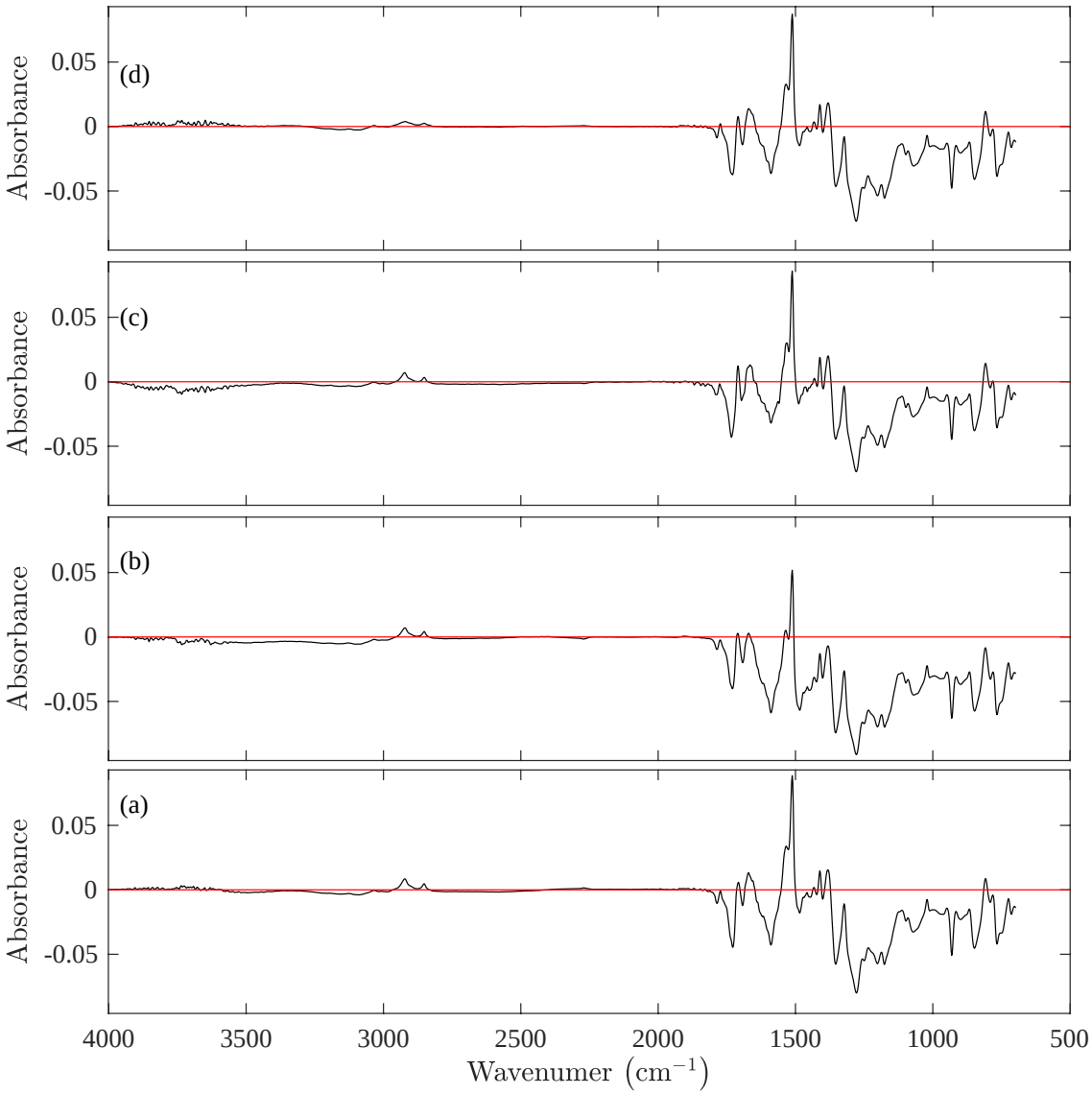

Figure 5.7: FT-IR difference spectrum between healthy and Coil 4, layer 3. The aged insulation spectrum was subtracted from the healthy spectrum. The red line is the zero mark, where the two spectra are equal.

Chapter 6: Loose Magnet Wire Thermal Aging

Prior to this chapter, the experiments were concerned with examining the insulation of magnet wire that was used in an electromagnetic coil. In this chapter, the mechanical and chemical properties of aged insulation from loose magnet wire aged outside of a coil are examined.

6.1 Aging in Air

In this experiment, a single piece of magnet wire with Essex heavy Allex polyimide insulation was placed in a thermal chamber at 250 °C (10 degrees Celsius greater than its 20,000 hours rating) for 7 weeks. A portion of the magnet wire was removed from the larger wire at weeks 1, 2, 3, and 5, and the remainder was removed at week 7. Each piece of removed magnet wire was divided and one part examined using nanoindentation and the other examined using FT-IR.

6.1.1 Nanoindentation Results

Over the course of the experiment, the modulus of elasticity and hardness changed. These changes are shown in Figure 6.1 and Figure 6.2. The same method of producing boxplots was used as that used in Section 4.2.

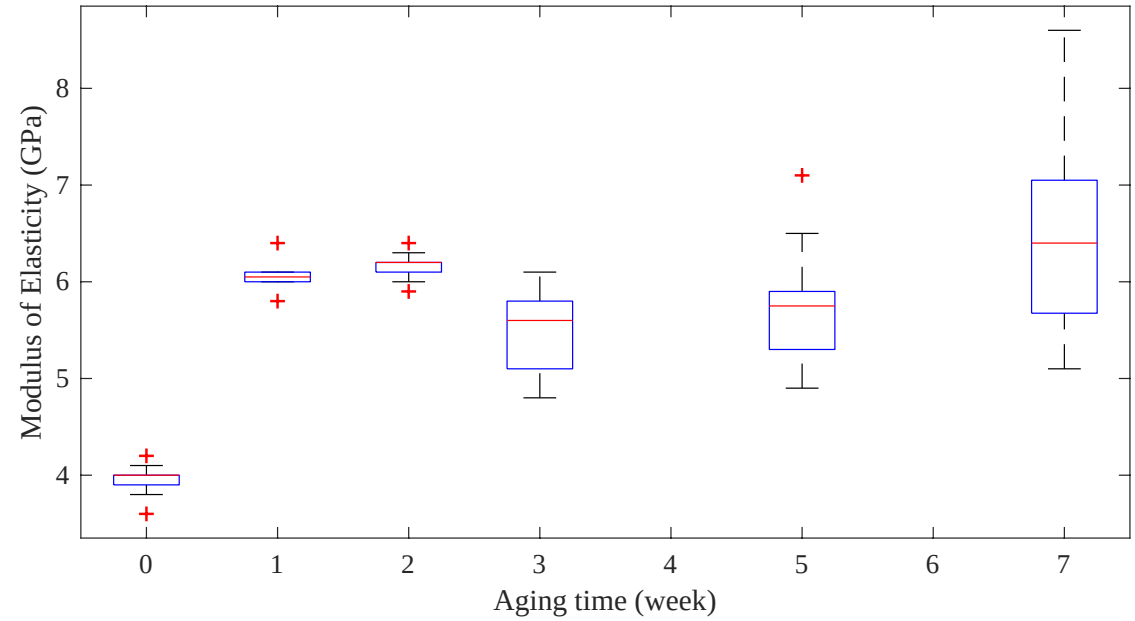

Figure 6.1: Evolution of polyimide insulation modulus of elasticity for a piece of magnet wire aged at 250 °C.

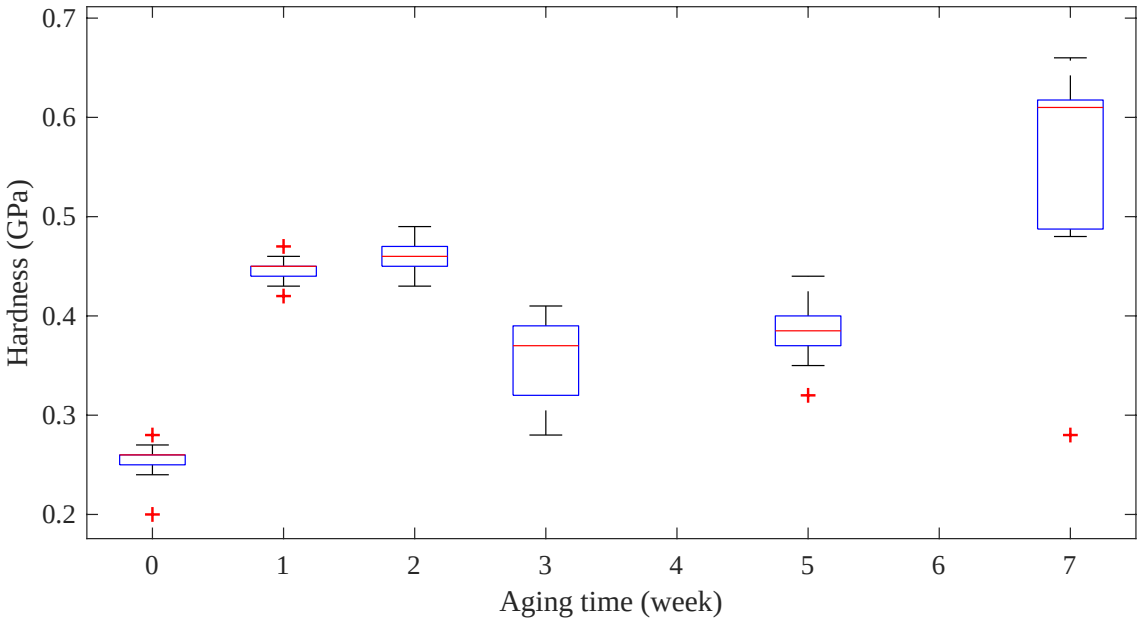

Figure 6.2: Evolution of polyimide insulation hardness for a piece of magnet wire aged at 250 °C.

These results reinforce those shown for the dual-wound coil experiments. Both the modulus of elasticity and the hardness of the insulation material increase as a

result of thermal aging. There is an initial steep increase in modulus of elasticity and hardness that appears to remain relatively steady for the next week. At week 3, there is a small drop in both and this is relatively steady through the next two weeks. Both modulus of elasticity and hardness increase at week 7, though hardness has a greater relative increase. The ratio of modulus of elasticity to hardness is shown in Figure 6.3.

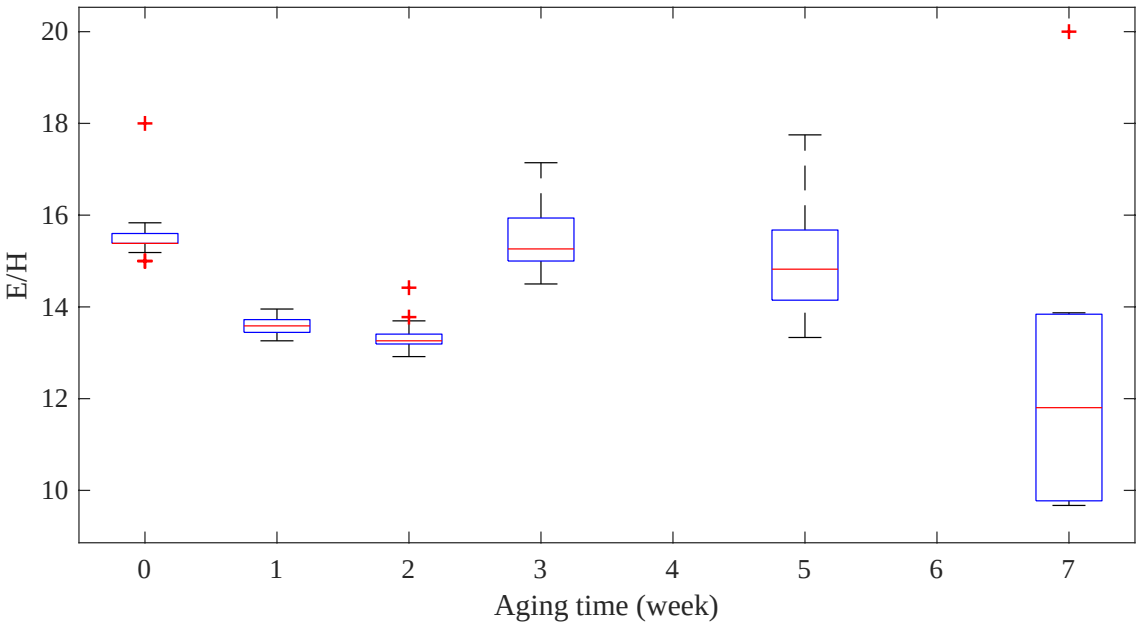

Figure 6.3: Evolution of polyimide insulation modulus of elasticity to hardness for a piece of magnet wire aged at 250 °C.

This again parallels the findings from the dual-wound coils, showing that thermal aging of the polyimide insulation material results in decreased values of fracture toughness as measured by the ratio of modulus of elasticity to hardness.

6.1.2 FT-IR Results

The procedure for acquiring the FT-IR spectra is the same as that presented in Section 5.2. The temporal FT-IR data for the polyimide insulation material are shown in Figure 6.4 and the FT-IR difference (computed as $\mathrm{IR}_{\mathrm{healthy}} - \mathrm{IR}_{\mathrm{aged}}$) spectra are shown in Figure 6.5.

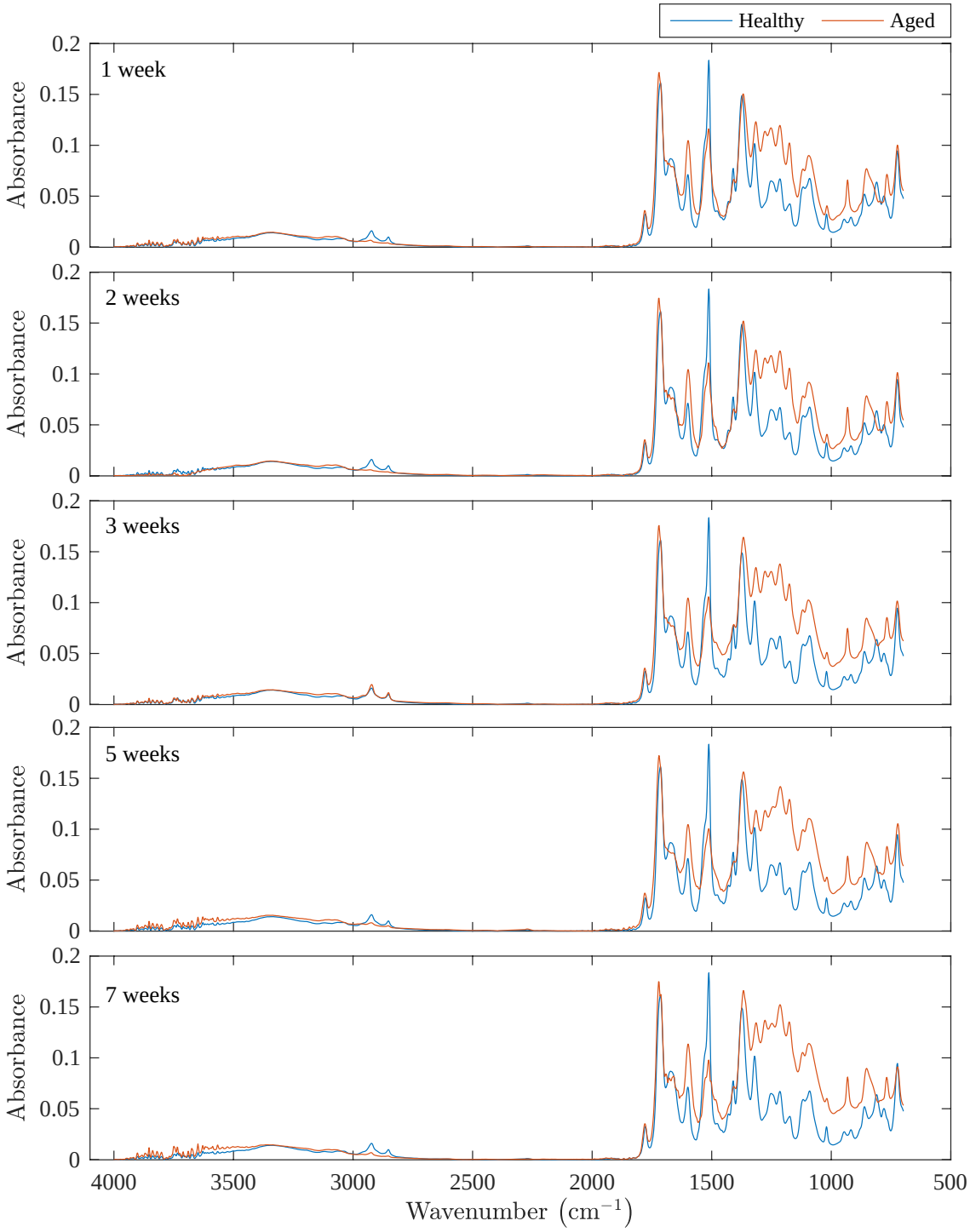

Figure 6.4: Evolution of polyimide insulation FT-IR spectrum for a piece of magnet wire aged at 250 °C.

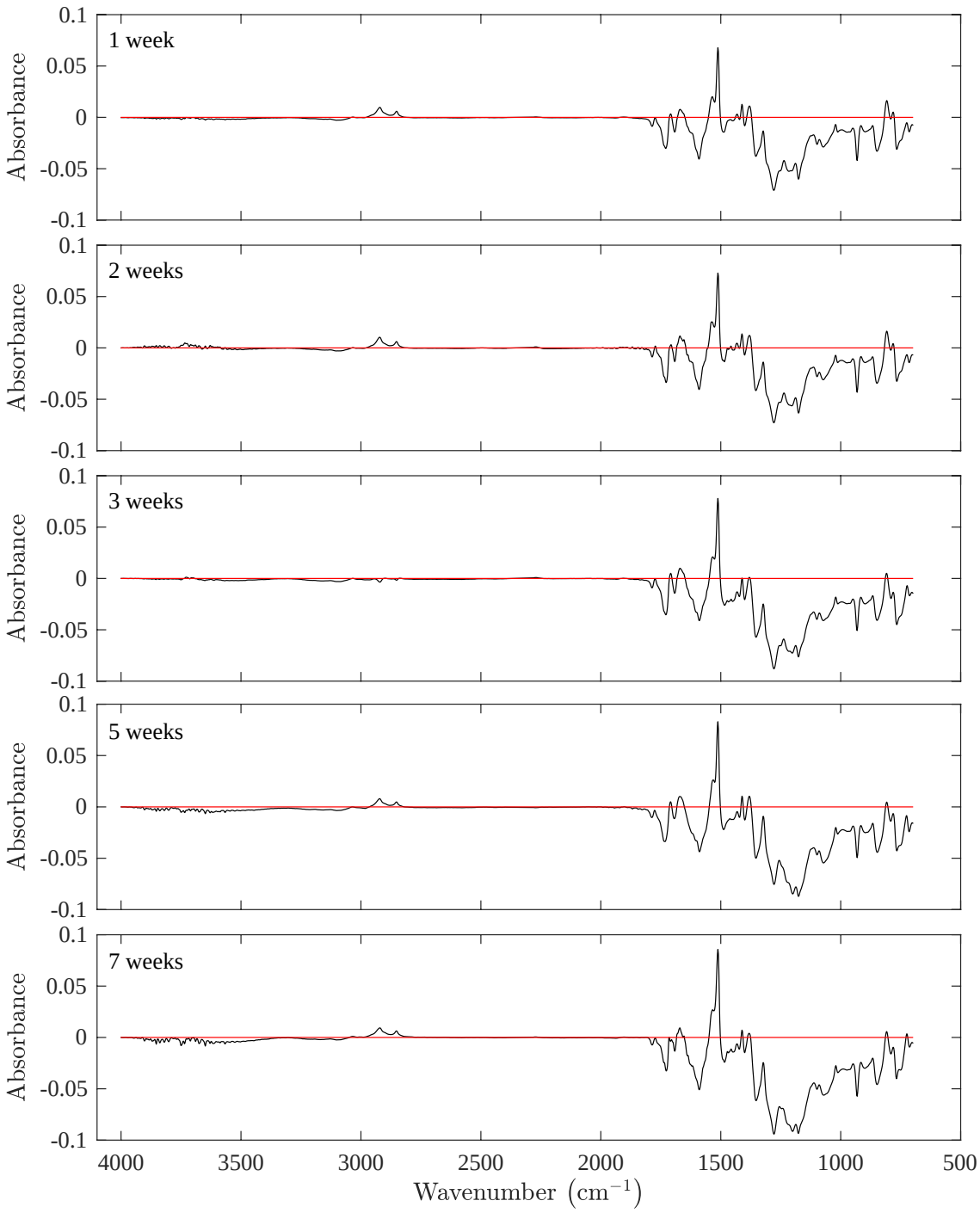

Figure 6.5: Evolution of polyimide insulation FT-IR spectrum for a piece of magnet wire aged at 250 °C.

It appears that with the FT-IR measurements parallel those found in the dual-wound coil experiment. Indeed, the locations of change in the spectrum noted in Section 5.2 and Figure 5.6 (1514 cm^{-1}, 1277 cm^{-1}, 931 cm^{-1}, 852.4 cm^{-1}, and 767.5 cm^{-1}) appear in the first week of thermal aging of the magnet wire. At 1092 cm^{-1} and

1117 cm^{-1} there is a pair of peaks that is initially very close to the healthy insulation spectrum at those wavenumbers. However, as the insulation continued to age, the intensity of the aged insulation diverged from the healthy insulation spectrum at those wavenumbers. There is also a small peak at 1018 cm^{-1} where the aged insulation and the healthy insulation were close in IR intensity. As the insulation aged, the peak diminished significantly.

6.2 Aging in Argon

In this experiment, a single piece of magnet wire with Essex heavy Allex polyimide insulation was placed in a thermal chamber at 250 °C (10 degrees Celsius greater than its 20,000 hours rating) for 5 weeks. The magnet wire was placed in a container while both the container and magnet wire were inside a glovebox that was filled with argon gas (the glovebox interior was slightly above atmospheric pressure). The container had caps on both ends, and the threads were sealed with teflon tape. The container with the magnet wire inside are shown in Figure 6.6.

Figure 6.6: Container with magnet wire inside, which was assembled and sealed in an argon environment.

The mechanical properties of the aged insulation material were measured using nanoindentation. The modulus of elasticity, hardness, and ratio of modulus of elasticity to hardness are shown in Figure 6.7. The boxplots show the distribution of values for healthy insulation, insulation aged for 5 weeks in argon, and insulation aged for 5 weeks in air (i.e., values at 5 weeks shown in Figures 6.1, 6.2, and 6.3).

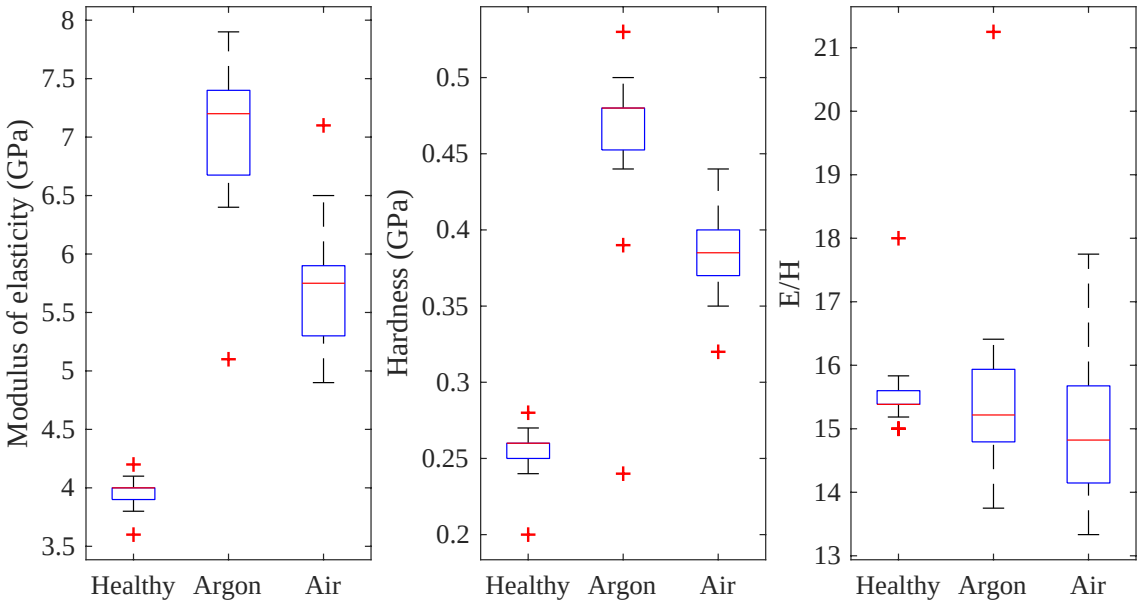

Figure 6.7: Modulus of elasticity, hardness, and ratio of modulus of elasticity to hardness of the polyimide insulation for a piece of magnet wire aged at 250 °C in argon gas for 5 weeks, compared with healthy insulation and insulation aged in air for 5 weeks.

The insulation aged in argon for 5 weeks has higher values of modulus and hardness than the insulation aged in air for 5 weeks, which is higher than the values for the healthy insulation. The ratio E/H for the insulation aged in argon is slightly lower than the healthy, but is slightly higher than the insulation aged in air. However, the hardness of the air aged insulation increased noticeably after 7 weeks of aging, which made the E/H ratio much lower after 7 weeks.

The IR spectrum of the argon-aged insulation sample was measured in the same manner as that of previous IR spectra discussed in this study. The comparisons of the healthy insulation IR spectrum with that of the insulation aged in argon, and of the insulation aged in air (at 5 weeks) with that of the insulation aged in argon are shown in Figure 6.8, and the difference spectra are shown in Figure 6.9. The argon-aged insulation IR spectrum and the air-aged IR spectrum were normalized to the healthy insulation IR spectrum according to the normalization scheme discussed in Section 5.2. The difference spectra were computed as: (a) $\mathrm{IR}_{\mathrm{healthy}} - \mathrm{IR}_{\mathrm{argon}}$; and (b) $\mathrm{IR}_{\mathrm{air}} - \mathrm{IR}_{\mathrm{argon}}$.

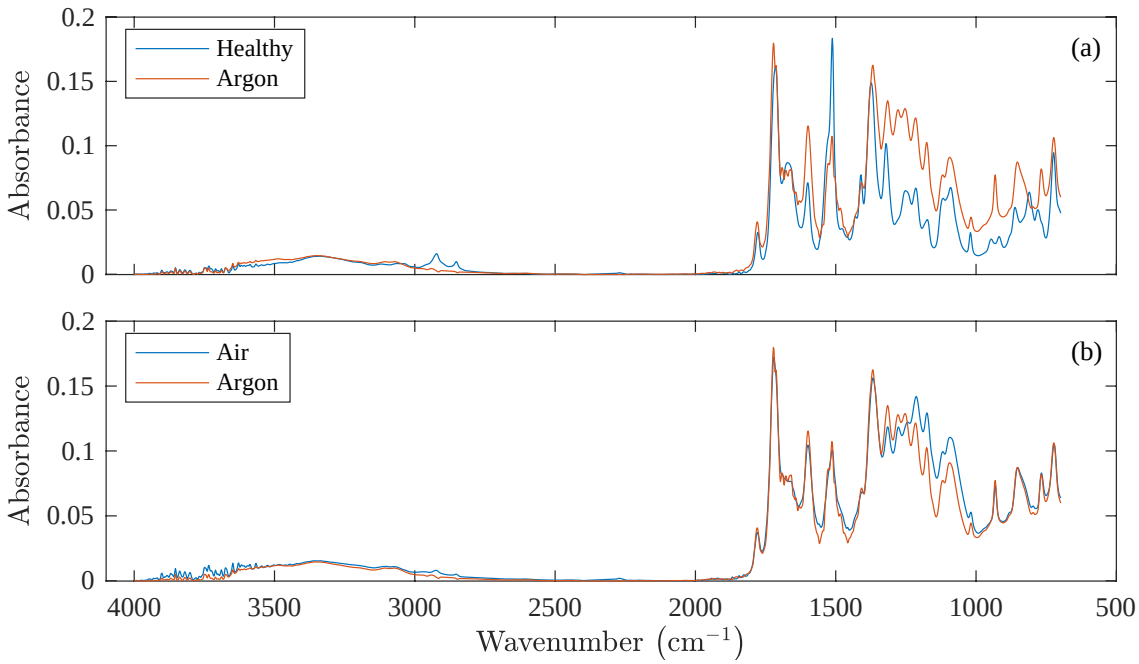

Figure 6.8: Comparison of IR spectrum of argon-aged insulation with (a) healthy insulation; and (b) air-aged insulation at 5 weeks.

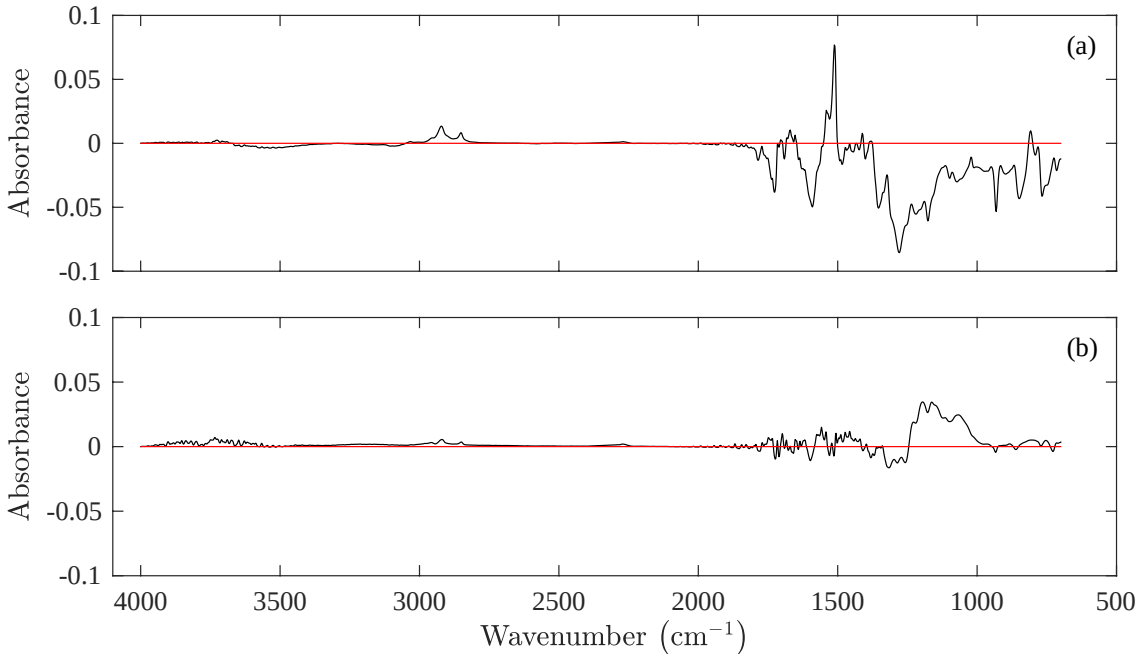

Figure 6.9: IR difference spectra of 5 week argon-aged insulation with (a) healthy insulation, computed as $\mathrm{IR}_{\mathrm{healthy}} - \mathrm{IR}_{\mathrm{argon}}$; and (b) air-aged insulation at 5 weeks, computed as $\mathrm{IR}_{\mathrm{air}} - \mathrm{IR}_{\mathrm{argon}}$.

The similarity of the argon-aged and air-aged IR spectra above about 1500 cm^{-1} suggests that there are portions of the aging/degradation mechanism, such as the decreased intensity of C−C aromatic bonds, that are not oxygen dependent. The difference spectrum in Figure 6.9(b) can be broadly split into two distinct regions of interest: 1250-1340 cm^{-1}, where the argon-aged insulation IR spectrum has a higher intensity, and 950-1250 cm^{-1}, where the air-aged insulation IR spectrum has a higher intensity. These regions may account for the differences observed in the mechanical properties.

Chapter 7: Conclusion

Electromagnetic coil insulation is recognized as a primary site of coil failures. Insulation health monitoring can reduce machine downtime, but it remained challenging to identify features with adequate sensitivity that are readily measurable. Previous authors [33–36] investigated impedance-based coil insulation diagnostic systems based upon the assumption that the resonant frequency provided the best indication of insulation health. Unfortunately, while these studies are valuable, they did not address key features of the impedance frequency spectrum which are responsive to insulation degradation.

Prior to this study, no results were published examining the relationship between insulation electrical parameters and coil impedance. Indeed, most prior work that addressed coil impedance considered only the resonant frequency as an important feature for health monitoring purposes. However, while monitoring the resonant frequency can be useful for some insulation materials (and not as useful for others [17]), there is insulation health information found at most frequencies around resonance.

Monitoring the resonant frequency carries a requirement that one of two conditions must be met. The user must measure impedance over a fine grid of frequencies in order to know the precise frequency at which reactance crosses zero. Or the user must interpolate to estimate the frequency at which reactance crosses zero. This study showed that for impedance-based insulation health monitoring, neither a fine grid of frequencies be used nor linear interpolation need be used, since many frequencies around resonance contain insulation health information. As shown in the experiments herein, the frequencies around resonance experience a higher percent change than resonant frequency. This result is supported by the sensitivity analysis performed on an electromagnetic coil equivalent circuit model in Chapter 3, Section 3.2.

The experiments and analyses presented in this study revealed how impedance spectra evolve for electromagnetic coils when the insulation is subjected to thermomechanical stress, and where the spectrum changes most. The modulus of elasticity, hardness, and IR spectra were measured before and after insulation degradation, showing how the insulation material changes in conjunction with the changes in coil impedance. An additional experiment on loose magnet wire supported the modulus of elasticity, hardness, and IR spectra findings in the coil experiments. This data delivers quantitative measurements and analysis that will assist system designers in selecting ideal frequencies to use when employing impedance-based insulation health monitoring, and for choosing appropriate thresholds for repair and replacement ac-

tions.

7.1 Implementation

A preliminary idea for the implementation of such a system in an industrial setting would require a low-voltage AC signal at a specified frequency to be injected into the coil, superimposed on the power signal. Then the resulting output current must be measured to compute the impedance. This is similar to the system given by Perisse et al. [33]. The frequencies for which measurements are required are those in the vicinity of the original resonant frequency. For example, for the coil used in the preliminary experiment (see Section 1.2), the relevant frequencies (top 5% most sensitive frequencies) are between 182 and 408 kHz, which corresponds to a range of about $[0.72f_r, 1.62f_r]$, where f_r is the resonant frequency in Hz. For the dual-wound coils, the relevant frequencies (top 5% most sensitive frequencies) were in the range $[0.64f_r, 1.36f_r]$. Hence, based upon the experimental data presented in this study, a suitable range could be $[0.5f_r, 1.7f_r]$, though this range can be narrowed by characterizing how the impedance changes as the insulation degrades. Once the coil has been characterized in the lab, and the most sensitive frequencies identified, impedance need only be monitored at those identified frequencies, eliminating the need to monitor the entire spectrum. Depending upon the expected rate of degradation, the coils may only need to be monitored periodically (e.g., once a week), and their measurements trended over time in order to compare with the healthy baseline. In this way, multiple coils could be monitored by the same measurement system by switching the measurement device to interact with different coils. Alternatively, inexpensive microelectronic signal generator and detection components could be incorporated into the internal or external circuitry controlling the valve (or coil). Either approach would allow health monitoring without affecting the operational state of the valve or coil.

The variation of temperature in the proposed health monitoring scheme was not broached in this paper, as the presented spectra were isothermal. However, it is a concern that must be discussed. It is not uncommon for the coil temperature to be monitored using DC resistance (or thermocouples placed at various locations within the coil). Hence, one possible method for incorporating temperature effects into the impedance measurement is as follows. It is reasonable to assume that a given impedance spectrum will have been obtained at approximately a single temperature. Therefore, the procedure must take the temperature into account by mapping each measured spectrum into a spectrum measured at a reference temperature. In other words, after measuring a spectrum at a reference temperature, T_R, each subsequent spectrum should be passed through a model that can correct it to the reference temperature. The functional mapping must be developed using early spectra measurements at various temperatures (during which time, it can be assumed that the insulation is healthy) in order to have the mapping available that can differentiate between changes due to temperature and those due to insulation degradation.

7.2 Suggested Future Research

There is little understanding within the electrical insulation community of how different insulation materials' parameters will evolve in the conditions present in an electromagnetic coil. However, the results presented herein aim to close a portion of that knowledge gap by showing results for polyimide. Given the use of an aromatic polyimide insulation, the results are central to implementing a successful impedance-based health monitoring system for electromagnetic coils with polyimide insulation, since aromatic polyimides are widely used for insulation applications because of their stability in thermal stress environments. The results show how polyimide insulation capacitance and insulation resistance change when subjected to electromagnetic coil-specific degradation conditions, and how these parameter changes affect the overall coil impedance, in addition to corresponding changes in modulus of elasticity, hardness, fracture toughness, and material infrared (IR) spectrum. Hence, the first two suggestions for future research are meant to address these limitations. One direction for future research is to fill the gaps in knowledge concerning other insulation materials and how they change when subjected to stresses present in electromagnetic coils. The optimal discovery is a general principle relating polymer structure and the expected nature of degradation. In the research presented herein, changes in the IR spectra were measured and possible changes in bonds were noted. However, it is likely that additional examination techniques (e.g., nuclear magnetic resonance, x-ray photoelectron spectroscopy) could reveal more about the nature of the changes, shedding light on the chemical changes that are experienced by the insulation material. Moreover, it is important to understand how the increase in modulus of elasticity and hardness of polyimide and other insulation materials are congruent with the apparent shortened polymer length.

A second line of future research is into the underlying failure mechanism for insulation used in electromagnetic coils. Based on the findings presented in this study, it appears that the insulation experiences embrittlement, which, combined with the mechanical stresses present from conductor expansion, results in insulation fracture and the formation of turn-to-turn shorts. However, a more thorough investigation into polymer embrittlement and the measurement thereof is vital to providing a firm foundation for this particular failure mechanism.

A third line of future research deals with the implementation of this method toward coil prognostics. Two goals of the present research were to show that the impedance measurements were reflecting changes in the insulation material properties and to find frequencies where the insulation health was best reflected in the coil impedance measurements. However, in order for this to be valuable for electromagnetic coil users, the impedance measurements must be modeled and forecasted to provide indication of when the coil should be replaced for maximum useful life, but prior to insulation failure. Hence, an optimal method for prognostics would model impedance measurements near the coil resonance, and using knowledge about the failure threshold, forecast the models into the future in order to find when the measurements cross the failure threshold. The resonant frequency and failure threshold can be determined from preliminary testing in a laboratory.

A final line of future research is into the implementation of this method in an industrial environment. Within this potential effort are three main thrusts. First, an industrial environment may contain multiple stressors, including humidity and radiation, which may act in conjunction with the thermo-mechanical stress discussed in this research. Hence, it is necessary to understand the effect of these stressors on insulation degradation and on the impedance measurements. Second, measuring impedance in an industrial environment will present its own challenges. It is critical to the effectiveness of this method that the measured impedance reflect true measurements from the electromagnetic coil under investigation. However, it is likely that if a measurement signal is transmitted over long distance, there will be signal degradation, and this must be taken into account. Of course, there are other means to measure coil impedance, including mobile impedance probes. There are repeatability challenges associated with these probes, in that impedance will be dependent upon the connection between the probe and the coil. Thus, it would be valuable to quantify the uncertainty associated with the use of a mobile impedance probe in measuring coil impedance. Finally, it is necessary to address the affect that positional changes of a magnetically permeable core (e.g., a plunger in a solenoid valve) might have on the impedance measurements. This is especially important for solenoid-operated valves, in which the plunger may gradually change position as the plunger, the plunger tube, and/or the spring may degrade causing slight changes in the plunger position.

Chapter 7: Contributions and Resulting Publications

7.1 Contributions

In this research, the contributions made are as follows. First, I developed an electromagnetic coil health monitoring method using low signal impedance measurement, thus minimizing disturbance to the system. I used the Spearman rank correlation coefficient to narrow the range of frequencies necessary to assess insulation health. Second, I established links between the electromagnetic coil impedance measurements and the mechanical, chemical, and electrical properties of polyimide insulation when subjected to thermo-mechanical aging. An equivalent circuit model (ECM) was developed and the theoretical sensitivity coefficients of the ECM with respect to changes in the insulation capacitance and resistance were computed. A set of four (4) dual-wound electromagnetic coils with aromatic polyimide insulation were thermo-mechanically aged and the aging data was analyzed using a "slope-enhanced" Spearman correlation spectrum, which showed the frequencies of high correlation in addition to the frequencies where the time series had the highest linear (least-squares) slopes, in an absolute value sense. The insulation modulus of elasticity and hardness were measured using nanoindentation. These measurements showed that, as the insulation thermally aged in an electromagnetic coil application, the modulus of elasticity and hardness increased. The new and aged insulation IR spectra were measured using Fourier transform infrared (FT-IR) spectroscopy. An analysis of the FT-IR data revealed that the concentration of C−C aromatic bonds decreased, while the intensity of epoxides, a class of 3-ring ethers, increased. Third, I developed a hypothesized failure mechanism for the polyimide insulation where the insulation thickness decreased and material brittleness increased. This combination results in a material more prone to fracture, which results in the failure of the insulation, and ultimately, failure of the electromagnetic coil.

7.2 Resulting Publications

1. N. Jordan Jameson, M. H. Azarian, and M. Pecht, "Impedance-based condition monitoring for insulation systems used in low-voltage electromagnetic coils," *IEEE Transactions on Industrial Electronics*, vol. 64, no. 5, pp. 3748–3757, May 2017.

2. N. Jordan Jameson, Michael H. Azarian, and Michael Pecht, "Improved electromagnetic coil insulation health monitoring using equivalent circuit model

analysis," submitted March 2019 (under review), *International Journal of Electrical Power & Energy Systems*.

3. N. Jordan Jameson, Michael H. Azarian, and Michael Pecht, "The connection between degraded electromagnetic coil Insulation parameters and coil impedance: Part 1 – Electrical measurements", *in-progress*.

4. N. Jordan Jameson, Michael H. Azarian, and Michael Pecht, "The connection between degraded electromagnetic coil Insulation parameters and coil impedance: Part 2 – Mechanical and chemical measurements", *in-progress*.

5. N. Jordan Jameson, Michael H. Azarian, and Michael Pecht, "Comparative analysis of thermally aged polyimide and polyester magnet wire insulation mechanical and chemical properties," *in-progress*.

6. N. Jordan Jameson, Michael H. Azarian, and Michael Pecht, "Thermal degradation of polyimide insulation and its effect on electromagnetic coil impedance," *Proceedings of MFPT 2017 Annual Conference*, May 16-18, 2017.

7. N. Jordan Jameson, M. H. Azarian, M. Pecht, K. Wang, and X. Aidong, "Electromagnetic coil equivalent circuit model sensitivity analysis for impedance-based insulation health monitoring," in *2017 Prognostics and System Health Management Conference (PHM-Harbin)*, 2017, pp. 1–6.

8. N. Jordan Jameson, M. H. Azarian, and M. Pecht, "Impedance-based health monitoring of electromagnetic coil insulation subjected to corrosive deterioration," in *Proceedings of the Annual Conference of the Prognostics and Health Management Society 2016*, Denver, CO, 2016.

9. N. Jordan Jameson, M. H. Azarian, and M. Pecht, "Correlation analysis for impedance-based health monitoring of electromagnetic coils," in *2016 IEEE International Conference on Prognostics and Health Management (ICPHM)*, 2016, pp. 1–6.

10. N. Jordan Jameson, M. H. Azarian, M. Pecht, C. Morillo, and K. Wang, "Health monitoring of solenoid valve electromagnetic coil insulation under thermal deterioration," in *Proceedings of MFPT 2016/ISA's 62nd IIS*, Dayton, OH, 2016.

11. N. Jordan Jameson, M. H. Azarian, and M. Pecht, "Fault diagnostic opportunities for solenoid operated valves using physics-of-failure analysis," in *2014 IEEE Conference on Prognostics and Health Management (PHM)*, 2014, pp. 1–6.

12. K. Wang, H. Guo, A. Xu, N. J. Jameson, M. Pecht, and B. Yan,"1Creating Self-Aware Low-Voltage Electromagnetic Coils for Incipient Insulation Degradation Monitoring for Smart Manufacturing," *IEEE Access*, vol. 6, pp. 69860–69868, 2018.

Bibliography

[1] V. P. Bacanskas, G. C. Roberts, and G. J. Toman. Aging and service wear of solenoid-operated valves used in safety systems of nuclear power plants: Volume 1, operating experience and failure identification. Technical report, Franklin Research Center, Philadelphia, PA (USA); Oak Ridge National Lab., TN (USA); Nuclear Regulatory Commission, Washington, DC (USA), 1987.

[2] Robert C. Kryter. Nonintrusive methods for monitoring the operational readiness of solenoid-operated values. *Nuclear Engineering and Design*, 118(3):409–417, 1990.

[3] Robert C. Kryter. Aging and service wear of solenoid-operated valves used in safety systems of nuclear power plants. Technical report, Oak Ridge National Lab; Nuclear Regulatory Commission, Washington, DC (USA), 1991.

[4] Motor Reliability Working Group. Report of large motor reliability survey of industrial and commercial installations: Part I. *IEEE Transactions on Industry Applications*, IA-21(4):853–864, July 1985.

[5] Motor Reliability Working Group. Report of large motor reliability survey of industrial and commercial installations: Part II. *IEEE Transactions on Industry Applications*, IA-21(4):865–872, July 1985.

[6] Olav Vaag Thorsen and Magnus Dalva. A survey of faults on induction motors in offshore oil industry, petrochemical industry, gas terminals, and oil refineries. *IEEE Transactions on Industry Applications*, 31(5):1186–1196, 1995.

[7] EG11.02 CIGRE Study Committee SC11. Hydrogenerator failures – results of the survey. Technical report, International Council on Large Electric Systems (CIGRE), 2003.

[8] Stefan Grubic, J.M. Aller, Bin Lu, and T.G. Habetler. A survey on testing and monitoring methods for stator insulation systems of low-voltage induction machines focusing on turn insulation problems. *IEEE Transactions on Industrial Electronics*, 55(12):4127–4136, December 2008.

[9] NEMA. NEMA MW 1000 - Magnet Wire, 2015.

[10] S. V. Angadi, R. L. Jackson, Song-Yul Choe, G. T. Flowers, J. C. Suhling, Young-Kwon Chang, and Jung-Keol Ham. Reliability and life study of hydraulic solenoid valve. Part 1: A multi-physics finite element model. *Engineering Failure Analysis*, 16(3):874–887, 2009.

[11] S. V. Angadi, R. L. Jackson, Song-yul Choe, G. T. Flowers, J. C. Suhling, Young-Kwon Chang, Jung-Keol Ham, and Jae-il Bae. Reliability and life study of hydraulic solenoid valve. Part 2: Experimental study. *Engineering Failure Analysis*, 16(3):944–963, 2009.

[12] Thomas Karte and Eugen Nebe. Reliability data and the use of control valves in the process industry in accordance with IEC 61508/61511. *Automatisierungstechnische Praxis (Translation)*, 47(2), 2005.

[13] Greg C. Stone, Edward A. Boulter, Ian Culbert, and Hussein Dhirani. *Electrical Insulation for Rotating Machines: Design, Evaluation, Aging, Testing, and Repair*. IEEE Press Series on Power Engineering. John Wiley & Sons, 2004.

[14] J. L. Bolland and Geoffrey Gee. Kinetic studies in the chemistry of rubber and related materials. II. The kinetics of oxidation of unconjugated olefins. *Transactions of the Faraday Society*, 42:236–243, 1946.

[15] Achim Göpferich. Mechanisms of polymer degradation and erosion. *Biomaterials*, 17(2):103–114, 1996.

[16] John Scheirs. *Compositional and Failure Analysis of Polymers: A Practical Approach*. John Wiley & Sons, 2000.

[17] N. Jordan Jameson, Michael H. Azarian, and Michael Pecht. Impedance-based condition monitoring for insulation systems used in low-voltage electromagnetic coils. *IEEE Transactions on Industrial Electronics*, 64(5):3748–3757, May 2017.

[18] Robert T. Sheldon and Nicola Bowler. An interdigital capacitive sensor for nondestructive evaluation of wire insulation. *IEEE Sensors Journal*, 14(4):961–970, 2014.

[19] P. J. Tavner. Review of condition monitoring of rotating electrical machines. *IET Electric Power Applications*, 2(4):215–247, August 2008.

[20] H. Arabian-Hoseynabadi, H. Oraee, and P. J. Tavner. Failure modes and effects analysis (fmea) for wind turbines. *International Journal of Electrical Power & Energy Systems*, 32(7):817–824, September 2010.

[21] Mehdi Nafar, Taher Niknam, and Amirhossein Gheisari. Using correlation coefficients for locating partial discharge in power transformer. *International Journal of Electrical Power & Energy Systems*, 33(3):493–499, March 2011.

[22] A. S. Deshpande; H. A. Mangalvedekar; A. N. Cheeran. Partial discharge analysis using energy patterns. *International Journal of Electrical Power & Energy Systems*, 53:184–195, December 2013.

[23] F. W. Fetherston; B. F. Finlay; J. J. Russell. Observations of partial discharges during surge comparison testing of random wound electric motors. *IEEE Transactions on Energy Conversion*, 14(3):538–544, September 1999.

[24] C. Hudon and M. Belec. Partial discharge signal interpretation for generator diagnostics. *IEEE Transactions on Dielectrics and Electrical Insulation*, 12(2):297–319, April 2005.

[25] Greg C. Stone. Partial discharge diagnostics and electrical equipment insulation condition assessment. *IEEE Transactions on Dielectrics and Electrical Insulation*, 12(5):891–904, October 2005.

[26] A. Mbaye, F. Grigorescu, T. Lebey, and Bui Ai. Existence of partial discharges in low-voltage induction machines supplied by pwm drives. *IEEE Transactions on Dielectrics and Electrical Insulation*, 3(4):554–560, August 1996.

[27] Hitoshi Okubo, Naoki Hayakawa, and Gian Carlo Montanari. Technical development on partial discharge measurement and electrical insulation techniques for llw voltage motors driven by voltage inverters. *IEEE Transactions on Dielectrics and Electrical Insulation*, 14(6):1516–1530, December 2007.

[28] Martin W. Kendig and Daniel N. Rogovin. Method of conducting broadband impedance response tests to predict stator winding failure, November 27 2001. US Patent 6,323,658.

[29] Martin W. Kendig and Daniel N. Rogovin. Method of conducting broadband impedance response tests to predict stator winding failure, November 19 2002. US Patent 6,483,319.

[30] A. Massarini, M. K. Kazimierczuk, and G. Grandi. Lumped parameter models for single-and multiple-layer inductors. In *Power Electronics Specialists Conference*, volume 1, pages 295–301. IEEE, 1996.

[31] Antonio Massarini and Marian K. Kazimierczuk. Self-capacitance of inductors. *IEEE Transactions on Power Electronics*, 12(4):671–676, 1997.

[32] Gabriele Grandi, Marian K. Kazimierczuk, Antonio Massarini, and Ugo Reggiani. Stray capacitances of single-layer solenoid air-core inductors. *IEEE Transactions on Industry Applications*, 35(5):1162–1168, 1999.

[33] Frédéric Perisse, Piotr Werynski, and Daniel Roger. A new method for ac machine turn insulation diagnostic based on high frequency resonances. *IEEE Transactions on Dielectrics and Electrical Insulation*, 14(5):1308–1315, 2007.

[34] Frédéric Perisse, David Mercier, Eric Lefevre, and Daniel Roger. Robust diagnostics of stator insulation based on high frequency resonances measurements. *IEEE Transactions on Dielectrics and Electrical Insulation*, 16(5):1496–1502, 2009.

[35] P. Neti and Stefan Grubic. Online broadband insulation spectroscopy of induction machines using signal injection. *IEEE Transactions on Industry Applications*, 53(2):1054–1062, March 2017.

[36] P Werynski, Daniel Roger, R Corton, and Jean F Brudny. Proposition of a new method for in-service monitoring of the aging of stator winding insulation in ac motors. *IEEE Transactions on Energy Conversion*, 21(3):673–681, 2006.

[37] Edward A. Boulter and Greg C. Stone. Historical development of rotor and stator winding insulation materials and systems. *IEEE Electrical Insulation Magazine*, 20(3):25–39, May 2004.

[38] P117 Materials Subcommittee Working Group. IEEE Standard Test Procedure for Thermal Evaluation of Systems of Insulating Materials for Random-wound AC Electric Machinery. *IEEE Std 117-2015 (Revision of IEEE Std 117-1974)*, pages 1–34, May 2016.

[39] Shinya Ota, Masaaki Yamauchi, Akira Mizoguchi, Kengo Yoshida, and Yasushi Tamura. Magnet wire with enhanced tolerance for high frequency voltage. Technical Review 84, Sumitomo Electric Group, April 2017.

[40] Sang Bin Lee, Karim Younsi, and Gerald B. Kliman. An online technique for monitoring the insulation condition of AC machine stator windings. *IEEE Transactions on Energy Conversion*, 20(4):737–745, 2005.

[41] Karim Younsi, Prabhakar Neti, Manoj Shah, Joe Yingneng Zhou, John Krahn, Konrad Weeber, and C David Whitefield. On-line capacitance and dissipation factor monitoring of AC stator insulation. *IEEE Transactions on Dielectrics and Electrical Insulation*, 17(5):1441–1452, 2010.

[42] S. Savin, S. Ait-Amar, D. Roger, and G. Vélu. Aging effects on the AC motor windings: A correlation between the variation of turn-to-turn capacitance and the PDIV. In *2011 Annual Report Conference on Electrical Insulation and Dielectric Phenomena (CEIDP)*, pages 64–67. IEEE, 2011.

[43] S. Savin, S. Ait-Amar, and D. Roger. Turn-to-turn capacitance variations correlated to PDIV for AC motors monitoring. *IEEE Transactions on Dielectrics and Electrical Insulation*, 20(1):34–41, 2013.

[44] Sombel Diaham, Marie-Laure Locatelli, and Thierry Lebey. Improvement of polyimide electrical properties during short-term of thermal aging. In *2008 Annual Report Conference on Electrical Insulation and Dielectric Phenomena*, pages 79–82. IEEE, 2008.

[45] Li Li, N. Bowler, P. R. Hondred, and M. R. Kessler. Dielectric response of polyimide to thermal and saline degradation. In *2010 Annual Report Conference on Electrical Insulation and Dielectic Phenomena*, pages 1–4. IEEE, 2010.

[46] Thomas W. Dakin. Electrical insulation deterioration treated as a chemical rate phenomenon. *Transactions of the American Institute of Electrical Engineers*, 67(1):113–122, 1948.

[47] B. Petitgas, G. Seytre, O. Gain, G. Boiteux, I. Royaud, A. Serghei, A. Gimenez, and A. Anton. High temperature aging of enameled copper wire: Relationships between chemical structure and electrical behavior. In *2011 Annual Report Conference on Electrical Insulation and Dielectric Phenomena (CEIDP)*, pages 84–88. IEEE, 2011.

[48] Mo-yuen Chow, Robert N. Sharpe, and James C. Hung. On the application and design of artificial neural networks for motor fault detection – Part I. *IEEE Transactions on Industrial Electronics*, 40(2):181–188, April 1993.

[49] Mo-yuen Chow, Robert N. Sharpe, and James C. Hung. On the application and design of artificial neural networks for motor fault detection – Part II. *IEEE Transactions on Industrial Electronics*, 40(2):189–196, April 1993.

[50] E. Rahimpour, M. Jabbari, and S. Tenbohlen. Mathematical comparison methods to assess transfer functions of transformers to detect different types of mechanical faults. *IEEE Transactions on Power Delivery*, 25(4):2544–2555, October 2010.

[51] G. S. Narayana, K. P. Badgujar, and S. V. Kulkarni. Factorisation-based transfer function estimation technique for deformation diagnostics of windings in transformers. *IET Electric Power Applications*, 7(1):39–46, January 2013.

[52] F. R. Blánquez, C. A. Platero, E. Rebollo, and F. Blánquez. Evaluation of the applicability of FRA for inter-turn fault detection in stator windings. In *2013 9th IEEE International Symposium on Diagnostics for Electric Machines, Power Electronics and Drives (SDEMPED)*, pages 177–182, August 2013.

[53] M. Rahmatian, B. Vahidi, A.J. Ghanizadeh, G.B. Gharehpetian, and H.A. Alehosseini. Insulation failure detection in transformer winding using cross-correlation technique with ANN and k-NN regression method during impulse test. *International Journal of Electrical Power & Energy Systems*, 53:209–218, December 2013.

[54] M. Heindl, Stefan Tenbohlen, Juan Velasquez, Alexander Kraetge, and Rene Wimmer. Algorithmic determination of pole-zero representations of power transformers' transfer functions for interpretation of FRA data. In *Proceedings of the 16th International Symposium on High Voltage Engineering*, 2009.

[55] M. Heindl, Stefan Tenbohlen, Juan Velasquez, Alexander Kraetge, and Rene Wimmer. Transformer modelling based on frequency response measurements for winding failure detection. In *Proceedings of the 2010 International Conference on Condition Monitoring and Diagnosis,*, September 2010.

[56] D. H. Johnson. Origins of the equivalent circuit concept: The voltage- source equivalent. *Proceedings of the IEEE*, 91(4):636–640, May 2003.

[57] D. H. Johnson. Origins of the equivalent circuit concept: The current-source equivalent. *Proceedings of the IEEE*, 91(5):817–821, May 2003.

[58] Ingo Schäfer and Klaus Krüger. Modelling of coils using fractional derivatives. *Journal of Magnetism and Magnetic Materials*, 307(1):91–98, December 2006.

[59] Ingo Schäfer and Klaus Krüger. Modelling of lossy coils using fractional derivatives. *Journal of Physics D: Applied Physics*, 41(4):1–8, February 2008.

[60] Bertrand Iooss and Paul Lemaître. A review on global sensitivity analysis methods. In *Uncertainty management in simulation-optimization of complex systems*, pages 101–122. Springer, 2015.

[61] D. M. Hamby. A review of techniques for parameter sensitivity analysis of environmental models. *Environmental Monitoring and Assessment*, 32(2):135–154, September 1994.

[62] Andrea Saltelli, Stefano Tarantola, Francesca Campolongo, and Marco Ratto. *Sensitivity analysis in practice: a guide to assessing scientific models*. Wiley Online Library, 2004.

[63] Nicola Bowler and Shuaishuai Liu. Aging mechanisms and monitoring of cable polymers. *International Journal of Prognostics and Health Management*, 6, 2015.

[64] T. Mizutani, T. Tsukahara, and M. Ieda. The effects of oxidation on the electrical conduction of polyethylene. *Journal of Physics D: Applied Physics*, 13(9):1673–1679, 1980.

[65] M. Nedjar. Effect of thermal aging on the electrical properties of crosslinked polyethylene. *Journal of Applied Polymer Science*, 111(4):1985–1990, 2009.

[66] Essex Group. Allex product data sheet, 2008.

[67] Jacques Curie. Recherches sur le pouvoir inducteur specifique et la conductibilite des corps cristallises (Research on the specific inductive power and on the conductivity of crystallized bodies). *Annales de chimie et de physique, 6. Serie*, 17:385–434, 1889.

[68] Egon Ritter von Schweidler. Studien über die anomalien im verhalten der dielektrika (Studies on the anomalous behaviour of dielectrics). *Annalen der Physik*, 329(14):711–770, 1907.

[69] IEEE recommended practice for testing insulation resistance of electric machinery. *IEEE Std 43-2013 (Revision of IEEE Std 43-2000)*, pages 1–37, March 2014.

[70] Anthony C. Fischer-Cripps. *Nanoindentation*. Mechanical Engineering Series. Springer, 3rd edition, 2011.

[71] Warren C. Oliver and Georges M. Pharr. Measurement of hardness and elastic modulus by instrumented indentation: Advances in understanding and refinements to methodology. *Journal of Materials Research*, 19(1):3–20, 2004.

[72] D. L. Joslin and Warren C. Oliver. A new method for analyzing data from continuous depth-sensing microindentation tests. *Journal of Materials Research*, 5(1):123–126, 1990.

[73] Lugen Wang and S. I. Rokhin. Universal scaling functions for continuous stiffness nanoindentation with sharp indenters. *International Journal of Solids and Structures*, 42:3807–3832, 2005.

[74] Brian Lawn and Rodney Wilshaw. Indentation fracture: Principles and applications. *Journal of materials science*, 10(6):1049–1081, 1975.

[75] A. G. Eans and E. A. Charles. Fracture toughness determinations by indentation. *Journal of the American Ceramic society*, 59(7-8):371–372, 1976.

[76] Brian R. Lawn, A. G. Evans, and D. B. Marshall. Elastic/plastic indentation damage in ceramics: The median/radial crack system. *Journal of the American Ceramic Society*, 63(9-10):574–581, 1980.

[77] G. R. Anstis, P. Chantikul, Brian R. Lawn, and D. B. Marshall. A critical evaluation of indentation techniques for measuring fracture toughness: I. Direct crack measurements. *Journal of the American Ceramic Society*, 64(9):533–538, 1981.

[78] M. T. Laugier. Palmqvist indentation toughness in WC-Co composites. *Journal of Materials Science Letters*, 6(8):897–900, 1987.

[79] Yvete Toivola, Jeremy Thurn, and Robert F. Cook. Structural, electrical, and mechanical properties development during curing of low-k hydrogen silsesquioxane films. *Journal of the Electrochemical Society*, 149(3):F9–F17, 2002.

[80] Michelle L. Oyen and Robert F. Cook. A practical guide for analysis of nanoindentation data. *Journal of the Mechanical Behavior of Biomedical Materials*, 2(4):396–407, 2009.

[81] Peter R. Hondred, Nicola Bowler, and Michael R. Kessler. Electrothermal lifetime prediction of polyimide wire insulation with application to aircraft. *Journal of Applied Polymer Science*, 130(3):1639–1644, 2013.

[82] H. George and P. McIntyre. *Infrared Spectroscopy*. John Wiley & Sons, 1986.

[83] Michael Nathan Grigg. *Thermo-Oxidative Degradation of Polyamide 6*. PhD thesis, Queensland University of Technology, 2006.

[84] Kashmiri Lal Mittal, editor. *Polyimides: synthesis, characterization, and applications*, volume 1. Springer Science & Business Media, 1984.

[85] M. Tsukiji, W. Bitoh, and J. Enomoto. Thermal degradation and endurance of polyimide films. In *IEEE International Symposium on Electrical Insulation*, pages 88–91. IEEE, 1990.

[86] George Socrates. *Infrared and Raman characteristic group frequencies: tables and charts*. John Wiley & Sons, 2004.

[87] Habib Saedi. Intercalated polyamide-imide nanocomposite with montmorillonite. *American Journal of Polymer Science*, 5(2):47–53, 2015.

[88] Sheng-Huei Hsiao, Guey-Sheng Liou, Yi-Chun Kung, and Yi-Ju Lee. Synthesis and characterization of electrochromic poly(amide–imide)s based on the diimide-diacid from 4, 4′-diamino-4″-methoxytriphenylamine and trimellitic anhydride. *European Polymer Journal*, 46(6):1355–1366, 2010.

[89] T. Johnson and S. Thomas. Effect of epoxidation on the transport behaviour and mechanical properties of natural rubber. *Polymer*, 41(20):7511–7522, 2000.

[90] I. Surya, S. Maulina, and H. Ismail. Effects of alkanolamide and epoxidation in natural rubber and epoxidized natural rubbers compounds. In *IOP Conference Series: Materials Science and Engineering*, volume 299, page 012061. IOP Publishing, 2018.

[91] C. M. Roland, J. K. Kallitsis, and K. G. Gravalos. Plateau modulus of epoxidized polybutadiene. *Macromolecules*, 26(24):6474–6476, 1993.